2010

The Effect Of Direct Yaw Moment On Human Controlled Vehicle Systems

Robert Rieveley
University of Windsor

THE EFFECT OF DIRECT YAW MOMENT ON HUMAN CONTROLLED VEHICLE SYSTEMS

by

ROBERT J. RIEVELEY

A Dissertation
Submitted to the Faculty of Graduate Studies
through Mechanical, Automotive, & Materials Engineering
in Partial Fulfillment of the Requirements for
the Degree of Doctor of Philosophy at the
University of Windsor

Windsor, Ontario, Canada
2010

THE EFFECT OF DIRECT YAW MOMENT ON HUMAN CONTROLLED VEHICLE SYSTEMS

by

ROBERT J. RIEVELEY

APPROVED BY:

Dr. R. Langlois, External Examiner
Carleton University

Dr. F. Ghrib
Civil and Environmental Engineering

Dr. J. Johrendt
Mechanical, Automotive, & Materials Engineering

Dr. D. Ting
Mechanical, Automotive, & Materials Engineering

Dr. P. Frise, Co-Advisor
Mechanical, Automotive, & Materials Engineering

Dr. B. Minaker, Advisor
Mechanical, Automotive, & Materials Engineering

Dr. E. Tam, Chair of Defense
Civil and Environmental Engineering

May 19, 2010

Author's Declaration of Originality

I hereby certify that I am the sole author of this thesis and that no part of this thesis has been published or submitted for publication.

I certify that, to the best of my knowledge, my thesis does not infringe upon anyone's copyright nor violate any proprietary rights and that any ideas, techniques, quotations, or any other material from the work of other people included in my thesis, published or otherwise, are fully acknowledged in accordance with the standard referencing practices. Furthermore, to the extent that I have included copyrighted material that surpasses the bounds of fair dealing within the meaning of the Canada Copyright Act, I certify that I have obtained a written permission from the copyright owner(s) to include such material(s) in my thesis and have included copies of such copyright clearances to my appendix.

I declare that this is a true copy of my thesis, including any final revisions, as approved by my thesis committee and the Graduate Studies office, and that this thesis has not been submitted for a higher degree to any other University or Institution.

Abstract

Advances in computing technology have had a profound impact on the design and development of modern vehicle systems. These advances have provided the basis for virtual design and testing in simulated environments, as well as the development of active control systems capable of providing improved vehicle safety, efficiency, and performance. Continued developments in hybrid powertrains and on-board computing will provide for greater amounts of control, through the integration of larger numbers of actuators and more complex control schemes. The intention of this research is to investigate the effects of advanced vehicle dynamics controls on the human operated vehicle system.

Hybrid electric vehicle systems incorporating multiple electric drive motors are capable of actively distributing drive and braking torque to the individual wheels of the vehicle. The modulation of these torques can be used to optimize or alter the dynamic response of the vehicle, through the application of a direct yaw moment. A control structure capable of determining and dynamically allocating appropriate control signals for over-actuated vehicle systems is proposed. A dynamic simulation of a virtual prototype BMW 330i is utilized to evaluate the effects of active drive torque vectoring on vehicle response. The effects of the proposed system on the human operator are also evaluated, through the use of driver model in-the-loop simulations.

The results presented indicate the promising potential of direct yaw moment control in modulating the response of human operated vehicle systems. The interactions between the human driver model and control systems were shown to be favourable. The scientific contributions and implications of the research are detailed, including application of closed-loop simulation to engineering education. Conclusions on the efficacy of developed models, methodologies and systems are given. Finally, recommendations on potential improvements and future research regarding vehicle modelling and motion control are provided.

To my parents, Janet and Peter.

Acknowledgements

First, I would like to thank my supervisors Dr. Bruce Minaker and Dr. Peter Frise for their guidance, patience and thought provoking questions that have inspired me to go further than I would have otherwise. Specifically, I would like to thank Dr. Minaker for the enthusiasm, encouragement and the extensive knowledge that he has openly extended towards my research and teaching activities. I would also like to thank Dr. Greg Rohrauer who first introduced me to the wonderful world of graduate studies, and the opportunities it affords. Dr. Minaker, Dr. Frise and Dr. Rohrauer have proven to be a wealth of knowledge and experience that has truly made my research as fruitful as possible.

Furthermore, I would like to thank the Natural Sciences and Engineering Research Council of Canada, the Ontario Ministry of Training, Colleges and Universities, the AUTO21 Network Centres of Excellence and the University of Windsor for the funding that allowed me to freely pursue my many research interests and goals.

I extend a gracious thanks to my colleagues Nathan Nantais, Edward W.K. Oh, Siniša Drača, Hart Honickman, Mike Johnston, Kevin Martin and Alex Wood, who I have shared many hours, laughs and theoretical thoughts with over the years. I would also like to thank the AUTO21 researchers that I have had the pleasure of working with at the University of Waterloo, University of Ontario Institute of Technology, University of British Columbia and Memorial University.

I must also thank my family and friends for their love and steadfast support in all aspects of my life. Specifically, for watching and listening to my ramblings as the sometimes unintelligible dots that mean so much to me flashed across the computer screen. Finally, I would like to thank my ever present supporter Deanna, for her patience, encouragement and support.

Windsor, Ontario Robert J. Rieveley

"Creating a new theory is not like destroying an old barn and erecting a skyscraper in its place. It is rather like climbing a mountain, gaining new and wider views, discovering unexpected connections between our starting points and its rich environment. But the point from which we started out still exists and can be seen, although it appears smaller and forms a tiny part of our broad view gained by the mastery of the obstacles on our adventurous way up."
Albert Einstein

Contents

List of Tables

List of Figures

Notation

The notation throughout this work is used to denote mathematical types. Matricies are indicated by bold upper case letters, vectors are indicated by bold italicized lower case letters and scalars are indicated by italicized lower case letters. The notations for specific entities are listed below.

Label	Description
$a_{\mathrm{x}}, a_{\mathrm{y}}$	acceleration in the longitudinal and lateral directions
$\mathcal{A}$	first order system matrix
$\mathcal{B}$	first order input matrix
$\mathbf{B}_{\mathrm{h}}$	holonomic constraint Jacobian matrix
$\mathbf{B}_{\mathrm{nh}}$	nonholonomic constraint Jacobian matrix
c_{f}	front tire linear cornering stiffness
c_{r}	rear tire linear cornering stiffness
$\mathcal{C}$	first order state output matrix
$\mathbf{C}$	linear damping matrix
$\mathcal{D}$	first order input output matrix
$\mathbf{D}$	augmented input selection matrix
e	error
$\mathbf{E}$	tire to vehicle frame transformation matrix
f	force
$\boldsymbol{f}_{\mathrm{a}}$	applied forces
$\bar{f}$	allowable force
$\tilde{f}$	control force
$\hat{f}$	estimated force
f_1, f_2, f_3, f_4	force on front left, right and rear left,right tires respectively
g	gravitational constant

Label	Description
$\mathbf{G}$	genome matrix
$\mathbf{H}$	linear observer gain matrix
h_{rc}	height of roll centre
h_{s}	height of centre of mass above roll centre
i_{a}	armature current
$i_{\mathrm{w_f}}$,$i_{\mathrm{w_r}}$	rotational inertia of the wheel
i_{z}	inertia about vertical axis
i_{m}	motor rotational inertia
$\mathbf{I}$	inertia tensor
$\mathbf{I}_{\mathrm{d}}$	identity matrix
j	control penalty function
k_1,k_2	scalar gain coefficient
k_{b},k_{c},k_{d},k_{h},k_{v}	Magic Formula coefficients
k_{a_i},k_{b_i}	transfer function coefficients
$\mathbf{K}$	linear stiffness matrix
$\mathbf{K}_{\mathrm{c}}$	feedback control gain matrix
κ	longitudinal slip
κ^*	generalized slip
l_{f},l_{r}	distance from centre of mass to front and rear axles respectively
l_{t}	track width
l_{h}	height of vehicle centre of gravity
l_{hs}	height of vehicle centre of gravity above roll axis
$\mathbf{L}$	left orthogonal complement transformation matrix
m	mass of a rigid body
$\mathbf{M}$	mass matrix
n	number of
$\mathbf{N}$	interpolation functions
$\boldsymbol{p}$	global position of a body, containing linear and rotational terms
$\mathbf{P}$	solution to the matrix Riccati equation
$\boldsymbol{q}$	positions and orientations, first order system
$\boldsymbol{q}_{\mathrm{m}}$	measured positions and orientations, first order system
$\boldsymbol{q}_{\mathrm{e}}$	estimated positions and orientations, first order system
$\mathbf{Q}$	state penalty weighting matrix

Label	Description
r	rotational velocity about body-fixed vertical direction
r_e	effective tire rolling radius
$\mathbf{R}$	right orthogonal complement transformation matrix, input penalty weighting matrix
s	distance travelled, master element coordinate
$\mathbf{s}_f$	sensor frame
$\mathbf{s}_o$	imposed objectives, sensor order
$\mathbf{S}$	augmented state output selection matrix
$\mathbf{S}_o$	objective transformation matrix
t	time, master element coordinate
t_f	preview time
u	linear velocity in body-fixed longitudinal direction
$\boldsymbol{u}$	first order input
v	linear velocity in body-fixed lateral direction
$\mathbf{V}$	gyroscopic matrix
$\boldsymbol{w}$	body-fixed velocity of a body, containing linear and angular terms
$\mathbf{W}$	weighting matrix
$\boldsymbol{x}$	position and orientations
x_g	translation in global reference frame
ξ_{ss}	cornering ratio
y_g	translation in global reference frame
$\boldsymbol{z}$	first order system output
$\boldsymbol{z}_e$	reduced order estimator states
α_f, α_r	front and rear tire slip angles
β	vehicle side slip angle
δ_f, δ_r	front and rear wheel steer angle
δ_{sw}	steering wheel angle
λ	system eigenvalues
λ_d	desired eigenvalues
μ	tire-road friction coefficient
ψ	heading angle
Φ	state transition matrix
Ψ	forced state transisiton matrix
ω	angluar velocity about an axis

Label	Description
ρ	radius
ρ_{dyn}	dynamic cornering radius
ρ_{kin}	kinematic cornering radius
σ	disturbance
$\boldsymbol{\tau}_{\text{a}}$	applied torques
τ_i	motor torque
χ	sliding surface
ζ_{us}	understeer coefficient
$\wp_{\text{z}}$	moment about vertical axis

Chapter 1

Introduction

Advances in computing technology have had a profound impact on the design and development of modern vehicle systems. These advances have provided the basis for virtual design and testing in simulated environments, as well as the development of active control systems capable of providing improved vehicle performance, efficiency, and safety. As the complexity and fidelity of the virtual models have increased, the analysis and development of ever more complicated and integrated systems can be achieved. The analysis of which, is well beyond the problems that could ever be tackled by hand.

The introduction to the detailed research is broken into two sections. First, background information regarding the integration of vehicle dynamics and control is presented. Second, the research objectives are stated, and a layout of the remaining chapters is given.

1.1 Vehicles, Computers and Control

The general requirements and design characteristics of modern road vehicles and systems were inherited from the wooden carts and wagons used by ancient civilizations [28]. The evolution was marked with several technological advances, the largest of these being the addition of the internal combustion engine. Other important advances defining the modern road vehicle include the addition of pneumatic tires, suspensions, hydraulic dampers and independent braking systems at each wheel. Recently, the adoption of computer assisted design techniques has allowed for the virtual analysis and design of vehicle components and systems, reducing capital and lead costs associated with traditional empirical methods. The success of these techniques has lead to the integration of computer systems within the vehicle architecture.

A large volume of research on the application of modern control and computer design techniques to passenger vehicles has stemmed from developments in the area of in-vehicle computer systems.

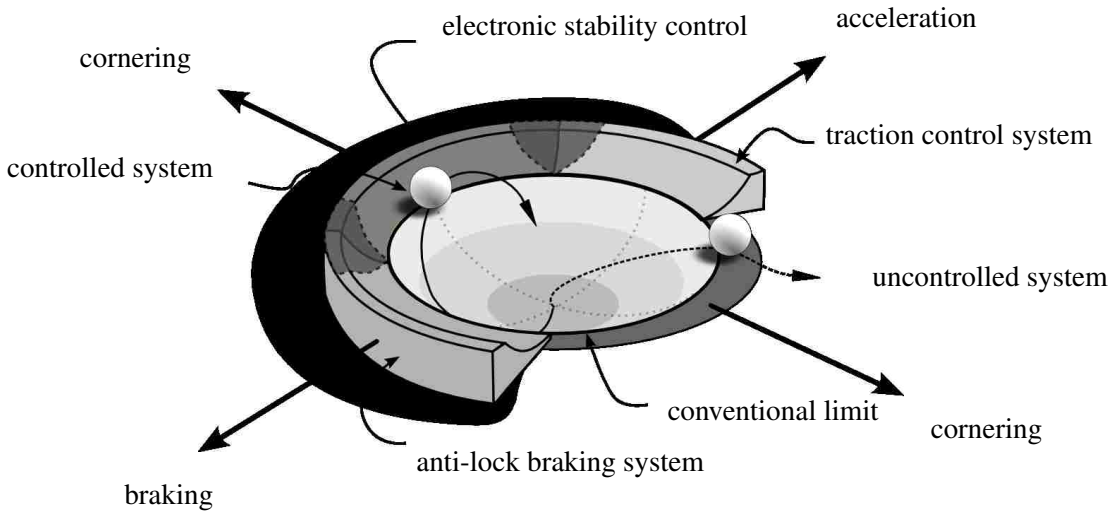

Figure 1.1: *Modern stability control analogy*. The stability bowl analogy uses a marble in a bowl to illustrate the increase in stability afforded by various vehicle dynamics controls. Stability control systems including anti-lock braking, traction control, and electronic stability control can be used in concert to extend the region of stable operation, where the marble remains in the bowl of stability. In the given example, it can be seen that the uncontrolled marble exits the bowl, while the ESC system constrains the controlled marble. Adapted from Aga [5].

This research has lead to the development of vehicle dynamics control (VDC) systems designed to assist the driver in maintaining control in critical driving situations. A significant number of relevant texts and articles detail and propose automatic controls for engine, cruise, and traction control systems. More recently, direct yaw moment control (YMC) systems that produce corrective moments around the vertical axis of the vehicle have become popular, with the adoption of anti-lock brake systems (ABS). These active systems can be designed to work in concert to improve or maintain vehicle response and stability around the handling limits, as illustrated by the stability bowl analogy in Figure 1.1.

Statistical studies conducted by Aga [5], Giesen [29] and Papelis [68] have indicated large reductions in loss of control, severe accident, and casualty rates in vehicles equipped with VDC systems. Current legislation (FMVSS 126) in the United States of America mandating the adoption of brake system based electronic stability control (ESC) systems predicts a reduction of single vehicle accidents by 34% and 59%, for passenger cars and sport utility vehicles respectively [2]. This legislation also estimates an impact of saving 5,300-9,600 lives and reducing injuries by 156,000-238,000 annually. It is understandable that adoption of the VDC systems proposed within this

legislation can not guarantee vehicle safety in every event; however, the limits of control continue to increase with the integration of more advanced and combined vehicle control systems that blur the lines between conventional VDC systems [60].

Various modern vehicle control systems capable of meeting these regulations have been developed and become standard equipment on an increasing number of vehicles over the past decade. As such, it is expected that most systems developed by vehicle manufacturers will meet the intended operational and implementation targets enforced by FMVSS 126. However, recent technological advances in active driveline components and hybrid vehicle powertrains capable of modulating drive torques to the individual wheels of the vehicle have afforded an opportunity to expand the operational region and capabilities of vehicle dynamics control systems. These increased capabilities will be provided from corrective yaw moments being generated by drive forces at the contact patches, along with the braking forces of conventional ESC systems. However, such integrated systems require methods to allocate and distribute control forces between various control subsystems, as well as cost effective and reliable methods to develop analyze and test these systems.

1.2 Research Outline

This research is intended to develop and apply model-based simulation and control techniques to determine the effects of active dynamics control systems on human operated road vehicles. More specifically, the work focuses on demonstrating the viability of an integrated variable torque distribution direct yaw moment controls for hybrid electric vehicles.

1.2.1 Research Objectives

The first objective of this research is to develop an accurate and comprehensive closed-loop simulation model with the ability to investigate the interactions between a human operator and road vehicle systems. To this end, a set of mathematical models representing the dynamic behaviour of human drivers and vehicle systems must be identified, developed and implemented in software. This will allow the dynamic response of the human operated vehicle system to be evaluated within a controlled simulation environment.

The second objective is to determine the effect of direct yaw moment control on the human operated vehicle system. A set of control strategies for variable torque distribution direct yaw moment control for hybrid electric vehicles will be developed. Further, the effectiveness of the proposed control systems will be evaluated using the developed simulation models.

Finally, the effect of the the developed direct yaw moment control on the human operated vehicle system will be evaluated.

1.2.2 Structure of Thesis

The thesis consists of eight chapters. The first chapter introduces and describes the motivation and goals of the research. In Chapter 2, relevant literature regarding the state of the art within the individual research areas is presented. The following chapters discuss the necessary formulations and modelling activities to meet the goals outlined above. Figure 1.2 illustrates the integration of the efforts within the remaining chapters.

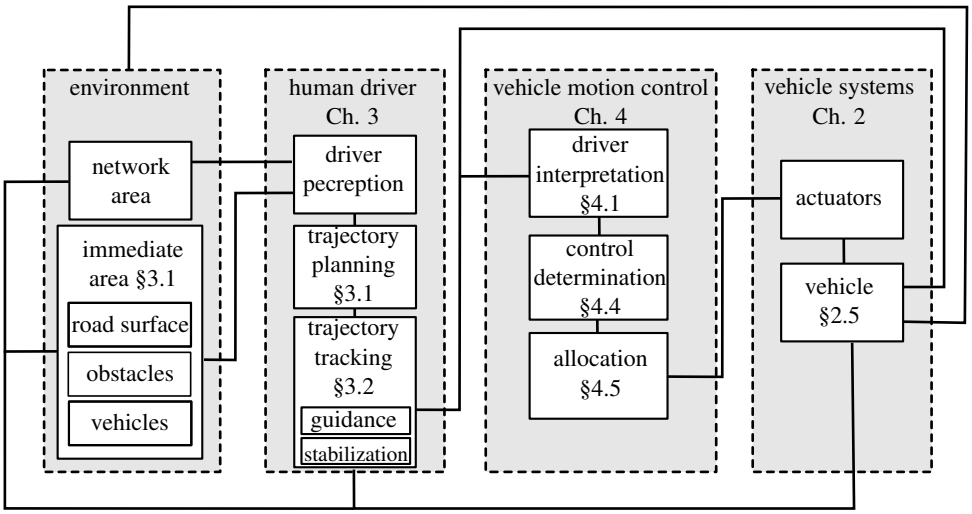

Figure 1.2: *Closed-loop model of human operated vehicle system.* The contributions of the dissertation within the closed-loop modelling of human operated vehicle systems can be found in the denoted sections.

In Chapter 3, the modelling and analysis of dynamic systems are detailed, with special attention to vehicle dynamics. A novel numerical approach for developing equations of motion for systems with nonholonomic constraints is presented and utilized to develop a set of increasingly complex linear vehicle models. These vehicle models are used to evaluate the stability and response of a 2006 BMW 330i in various configurations. The models are then verified using a fully nonlinear virtual prototype vehicle model in CarSim®. Methods for evaluating the stability of nonlinear systems are presented. The time domain response of the developed linear and nonlinear models are then compared.

In Chapter 4, the modelling and analysis of the human driver are presented in order to quantify the effect of the driver on vehicle system response. A nonlinear hybrid driver model is developed with preview based longitudinal and lateral control schemes. A novel method for path planning is presented, utilizing mapped track elements and genetic algorithm optimization techniques. The

application of the developed driver model to racing lap simulation is presented. Finally, the novel use of closed-loop driver models for vehicle dynamics education is presented.

In Chapter 5, the use of model-based techniques for the development of vehicle dynamics controls are presented. A particular focus is placed on developing a closed-loop variable torque distribution yaw moment control system for application within a prototype hybrid electric vehicle architecture. A hierarchical control structure is developed, comprised of driver interpretation, control determination and allocation levels. The development of methods for linear control design using automatically generated equations of motion are presented. To solve the over-actuation problem present within a given hybrid electric vehicle configuration, a tire force based control allocation algorithm is developed. Methods accounting for tire force, electric motor and effector limitations are presented. Finally, the potential incorporation of additional allocation objectives are discussed.

In Chapter 6, the synthesis and software implementation of the methods described in the preceding chapters are presented. The developed closed-loop simulation environment involving co-simulation of MATLAB®, Simulink®, and CarSim® is detailed, along with the integration of the required sub-component models.

In Chapter 7, a set of numerical experiments illustrating the efficacy of the developed controls and models are presented, and results are discussed. Both the open and closed loop simulation response of the developed BMW 330i model performing steering manoeuvres are presented. The interactions between the human operator and vehicle system are inferred and detailed. The effect of control gains, state estimating observers and vehicle configurations are also evaluated and results are presented.

In Chapter 8, conclusions on the development of design and simulation tools within the research are presented. Implications of the research are outlined, as are areas of potential future work.

Chapter 2

Literature Review

2.1 General Vehicle System Modelling

Conventional road vehicles are hybrid systems comprised of a human driver and a vehicle. The response of the vehicle is influenced by the driver input to the system, based on subjective analysis of incoming stimuli. The application of systems modelling and control theory can be used to augment the inputs of a driver to positively influence vehicle response. During modelling, the complete vehicle system can be separated into three main components including the human driver, vehicle dynamics management, and vehicle systems as shown in Figure 2.1. These systems operate in concert, actively and passively exchanging data important to the operation of the vehicle and subsystems.

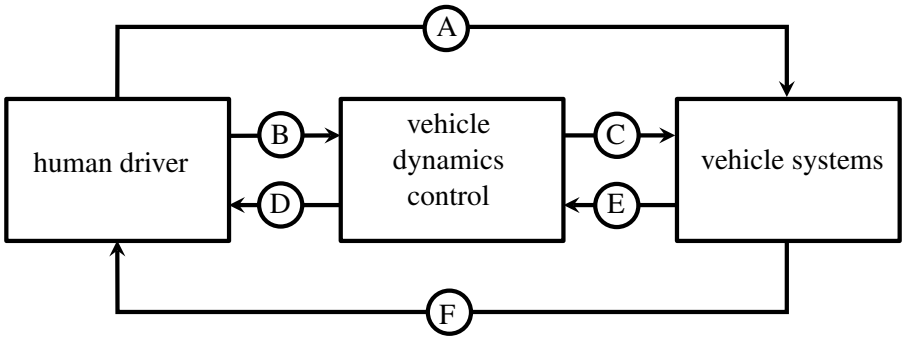

Figure 2.1: *Generalized vehicle system.* A conventional road vehicle is a hybrid system comprised of a driver, control and vehicle systems. These systems work in concert communicating feed-forward (A,B,C) and feedback (D,E,F) signals. A complete model requires the characterization of the appropriate subsystem models and the communications between them.

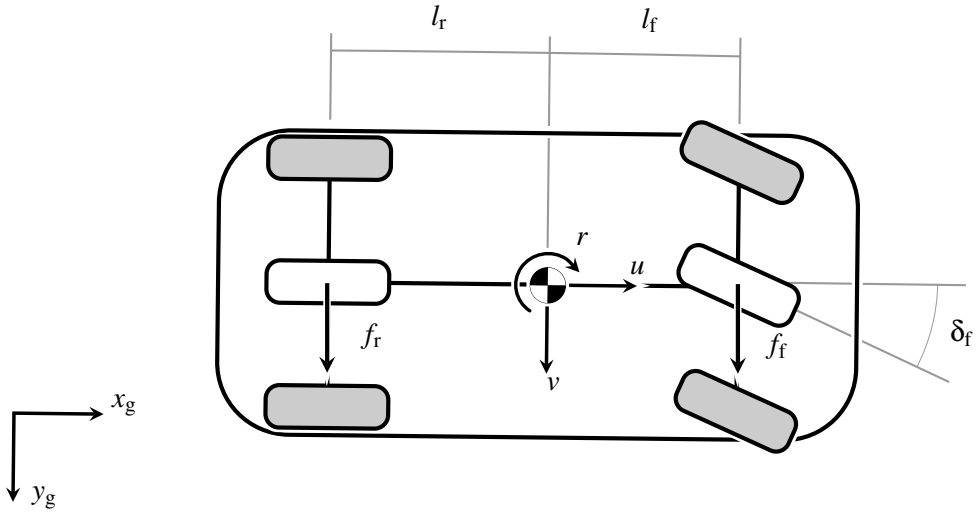

Figure 2.2: *Yaw-plane vehicle model.* The yaw-plane model has of two degrees of freedom and is widely used for handing analysis. The forward speed of the vehicle is parameterized as constant with lateral forces generated at the front and rear axles. The vehicle width is ignored, making use of lumped equivalent tires generating lateral forces f_f and f_r at distances of l_f and l_r from the centre of mass respectively.

2.2 Vehicle Modelling

Interest in the mathematical modelling of vehicles over the past century has lead to the development of various models capable of predicting vehicle response. The process of modelling involves creating a description of the physical system, formulating a set of governing equations and simulating the system response [39]. Several methods exist for the generation of the governing equations of vehicle systems including hand derivations [26], specialized hard coded models [36] and generic multibody approaches relying on numerical [47, 57] and symbolic [80, 59] formulations.

One of the most concise and widely utilized models for evaluating the handling response of a vehicle is the 'yaw-plane' or 'bicycle' model, illustrated in Figure 2.2. The latter terminology is derived from the assumption that the effect of vehicle width on tire force generation is considered negligible. The development and use of this model for the determination of vehicle handling characteristics was detailed by Ellis [26].

The equations of motion for the two degree of freedom model are developed in a local reference frame, with the forward speed u parameterized as constant. The degrees of freedom include the lateral velocity v and yaw rate r. The tire properties of the front and rear axles are given as a set of lumped equivalent tires, acting at the centre line of the vehicle with distances of l_f and l_r from the

centre of mass. The lateral tire forces developed by the front and rear equivalent tires are determined using a linear approximation where

$$\begin{aligned} f_{\mathrm{f}} &= -c_{\mathrm{f}}\alpha_{\mathrm{f}} \\ f_{\mathrm{r}} &= -c_{\mathrm{r}}\alpha_{\mathrm{r}} \end{aligned} \tag{2.2.1}$$

where the lateral cornering stiffnesses of the front and rear tires are given as c_{f} and c_{r}. Applying small angle assumptions, the slip angles α_{f} and α_{r} of the front and rear tires can be expressed as

$$\begin{aligned} \alpha_{\mathrm{f}} + \delta_{\mathrm{f}} &= \frac{v + r l_{\mathrm{f}}}{u} \\ \alpha_{\mathrm{r}} + \delta_{\mathrm{r}} &= \frac{v - r l_{\mathrm{r}}}{u} \end{aligned} \tag{2.2.2}$$

Rearranging and combining Equations 2.2.1 and 2.2.2, followed by substitution into Newton's second law, the governing set of equations of motion can be expressed as

$$\begin{bmatrix} m & 0 \\ 0 & i_{\mathrm{z}} \end{bmatrix} \begin{Bmatrix} \dot{v} \\ \dot{r} \end{Bmatrix} + \begin{bmatrix} \dfrac{(c_{\mathrm{f}} + c_{\mathrm{r}})}{u} & \dfrac{(l_{\mathrm{f}} c_{\mathrm{f}} - l_{\mathrm{r}} c_{\mathrm{r}})}{u} + mu \\ \dfrac{(l_{\mathrm{f}} c_{\mathrm{f}} - l_{\mathrm{r}} c_{\mathrm{r}})}{u} & \dfrac{(l_{\mathrm{f}}^2 c_{\mathrm{f}} + l_{\mathrm{r}}^2 c_{\mathrm{r}})}{u} \end{bmatrix} \begin{Bmatrix} v \\ r \end{Bmatrix} = \begin{bmatrix} c_{\mathrm{f}} \\ l_{\mathrm{f}} c_{\mathrm{f}} \end{bmatrix} \left\{ \delta_{\mathrm{f}} \right\} \tag{2.2.3}$$

where m is the vehicle mass, i_{z} is the yaw moment of inertia of the vehicle about the vertical axis. The steering angle of the lumped front tire is δ_{f}, where the steer angle of the rear axle δ_{r} is zero.

Steady-state Response

The yaw-plane model can be used to understand the effect of design parameters on the fundamental response of a vehicle. The terms 'understeer', 'neutral steer' and 'oversteer' stem from the use of this model, and indicate the difference between the 'dynamic cornering radius' and 'kinematic cornering radius' of a vehicle during steady-state cornering. The kinematic cornering radius represents the path the vehicle would exhibit if no lateral slipping of the tires occurred. Conversely, the dynamic cornering radius provides a more accurate representation of the cornering path of the vehicle in the presence of lateral tire slip. The relationship between dynamic and kinematic radii can be expressed as

$$\xi_{\mathrm{ss}} = \frac{\rho_{dyn}}{\rho_{kin}} = 1 - \frac{mu^2 \left(l_{\mathrm{f}} c_{\mathrm{f}} - l_{\mathrm{r}} c_{\mathrm{r}}\right)}{\left(l_{\mathrm{f}} + l_{\mathrm{r}}\right)^2 c_{\mathrm{f}} c_{\mathrm{r}}} \tag{2.2.4}$$

The vehicle will exhibit a neutral steering characteristic when $\xi_{\mathrm{ss}} = 1$, indicating that the vehicle will track the kinematic cornering radius in the presence of slipping. The vehicle will understeer when $\xi_{\mathrm{ss}} > 1$, or $l_{\mathrm{f}} c_{\mathrm{f}} < l_{\mathrm{r}} c_{\mathrm{r}}$, and oversteer with $\xi_{\mathrm{ss}} < 1$ or $l_{\mathrm{f}} c_{\mathrm{f}} > l_{\mathrm{r}} c_{\mathrm{r}}$. Another commonly used descriptor of the steady-state handling behaviour of a vehicle is the 'understeer coefficient' presented

by Karnopp [39]. This coefficient expresses the relationship between lateral acceleration and steer angle for a given vehicle configuration. The front wheel steer angle required to maintain a cornering radius at a given speed can be expressed as

$$\delta_f = \zeta_{\text{us}} \frac{u^2}{\rho} + \frac{l_\text{f} + l_\text{r}}{\rho} \tag{2.2.5}$$

where

$$\zeta_{\text{us}} = \frac{m(l_\text{r} c_\text{r} - l_\text{f} c_\text{f})}{(l_\text{f} + l_\text{r}) c_\text{f} c_\text{r}} \tag{2.2.6}$$

with positive and negative values of understeer coefficient ζ_{us} indicating understeer and oversteer characteristics respectively. It can be seen that for an understeering vehicle, the steer angle of the front wheels must be increased as lateral acceleration increases. Conversely, the steer angle must be reduced for an oversteering vehicle, leading to a zero steer input at the 'critical speed'. Beyond this point a 'counter-steer' or reverse steer must be applied to maintain the cornering radius.

The presence of slip induced by centripetal acceleration leads the vehicle to point in a direction other than the direction of travel; the difference in these directions is defined as the body slip angle, and can be expressed as

$$\beta = \frac{v}{u} \tag{2.2.7}$$

The steady-state response of a vehicle can be expressed using transfer functions relating model input and output. The transfer functions relating body slip angle and yaw rate to steer angle input are

$$\frac{\beta}{\delta_\text{f}} = \frac{l_\text{f} - \dfrac{l_\text{f} m u^2}{(l_\text{f} + l_\text{r}) c_\text{r}}}{l_\text{f} + l_\text{r} - \frac{m u^2 (l_\text{f} c_\text{f} - l_\text{r} c_\text{r})}{(l_\text{f} + l_r) c_\text{f} c_\text{r}}} \tag{2.2.8}$$

and

$$\frac{r}{\delta_\text{f}} = \frac{u}{(l_\text{f} + l_\text{r}) - \frac{m u^2 (l_\text{f} c_\text{f} - l_\text{r} c_\text{r})}{(l_\text{f} + l_\text{r}) c_\text{f} c_\text{r}}} \tag{2.2.9}$$

With these relationships it can be shown that the body side slip response of an understeering vehicle will reach limiting value, as the forward speed is increased. Conversely, the body slip angle and yaw rate response of an oversteering vehicle will become large and tend to infinity at the critical speed, expressed as

$$u_\text{crit} = \sqrt{\frac{c_\text{f} c_\text{r} (l_\text{f} + l_\text{r})^2}{m(l_\text{f} c_\text{f} - l_\text{r} c_\text{r})}} \tag{2.2.10}$$

These relationships can be useful in understanding the fundamental response of a vehicle. The addition of further vehicle inputs can be addressed in a similar manner, creating alternative single-input-multiple-output (SIMO) and multiple-input-multiple-output (MIMO) transfer relationships.

Other widely used linearized models describing planar motion, as well as vertical or ride motions of the vehicle can be found in the literature [28, 36]. While the development and use of higher fidelity nonlinear models with increased degrees of freedom are prevalent in the prediction of vehicle response, the basic yaw plane model captures the fundamental behaviour very well and is still widely used.

2.3 Vehicle Dynamics Control

The application of active control systems within vehicles has matured and grown from engine management to chassis control systems. Generally, these controls are developed using model-based control techniques, similar to those detailed by Slotine [82]. Open-loop controls involving only feed-forward signals A, B and C in Figure 2.1, as well as closed-loop controls adding feedback signals D, E and F can be made to stabilize a system or track a desired response. The desired characteristics of these controls can include stability, accuracy, speed, and robustness. A number of sequential or parallel design methodologies may be adopted, comprised of a number of steps:

1. Specify desired behaviour
2. Select actuators and sensors
3. Model the physical plant
4. Design a control law
5. Analyze and simulate the resulting control system
6. Implement the control in hardware

A wide range of research addressing these topics for the development of active systems for road vehicles can be found in the literature. Within the scope of control development, a number of separate problems and research areas are presented by Tseng [83], including driver intent recognition, control philosophy, state estimation, road bank angle estimation, robustness, system evaluation and implementation. A number of active control technologies have been proven effective in improving vehicle safety, and have subsequently found wide adoption on consumer vehicles within the past few decades. These technologies include open-loop and closed-loop traction control, steering control and brake-based electronic stability controls that utilize existing and proposed vehicle components [65, 86, 23, 37].

One such control involves the optimal distribution of front-to-rear drive and braking force when travelling in a straight line. The analysis of this problem has been extensively documented in introductory texts on vehicle dynamics [28, 36]. This analysis shows that improper brake distribution

can cause a divergent yaw instability if the rear wheels lock prior to the front wheels, in the presence of longitudinal load transfer. Traditionally, the effect of lateral load transfer on braking force distribution during cornering has been neglected in such texts. The work of Nantais [62] addressed this omission in considering the effect of lateral load transfer on braking force distribution. The developed brake force proportioning algorithm required an active braking system capable of proportioning brake forces to individual wheels. The study showed the proposed algorithm provided increased braking and lateral handling performance with minimal effect on driver effort. Further discussion on the effect of nonuniform brake distribution on the generation of yaw moments during limit cornering was presented by Koibuchi [46]. In this work, the effects of sudden increases in slip angle are discussed, leading to the definition of an approximate region of stability in the $\dot{\beta}$-β phase plane in which a vehicle can be expected to recover from perturbations.

In cases with high lateral acceleration, nonlinearities in tire force generation become significant when attempting to determine vehicle response characteristics, thus requiring nonlinear tire models. In the presence of these nonlinearities, the vehicle behaviour can change dramatically from understeering to oversteering in the presence of longitudinal and lateral demands. In these conditions the nonlinear response of the vehicle can be determined with the use of handling diagrams relating vehicle acceleration to the tire slip angles, as presented in [39, 55]. These clearly present the fundamental response of the vehicle model; however, these methods typically rely on simplistic vehicle models. Expanding on the traditional analysis, the work of Kato [40] details the dynamic square method (DSM) that can be used to quantify the quasi-steady state cornering ability of a vehicle during both braking and acceleration events. This method considers the effect of load transfer and cornering drag, using single and multiple track vehicle models. This method can provide information on the lateral acceleration capability and understeer/oversteer response in the presence of longitudinal acceleration, as illustrated in Figure 2.3. The figure presents the relationship between tractive force distribution to achieve a desired longitudinal acceleration and the lateral acceleration capability, given by a set of iso-lines when presented in two dimensions. From these iso-lines the nonlinear longitudinal force distribution to achieve optimal handling capabilities can be determined, illustrated by the bold line. In this illustration the regions of understeer (white) and oversteer (gray) are defined as cases where the front or rear axles saturate respectively, limiting the lateral handling capability of the vehicle. In the figure, most conventional operational conditions can be found the first and the third quadrants. The first quadrant represents the acceleration case where drive forces are being applied to both axles, where the third quadrant represents the case with only braking forces at the axles. The second and fourth quadrants illustrate combined driving and braking cases that may be utilized in regenerative processes in parallel-through-the-road hybrid vehicles. As the dynamic square expresses a wide range of operating conditions in a concise manner it can be a use-

ful tool in analyzing the operational characteristics of a chassis, as well as determining the optimal or desired force distribution between the front and rear axles of a vehicle.

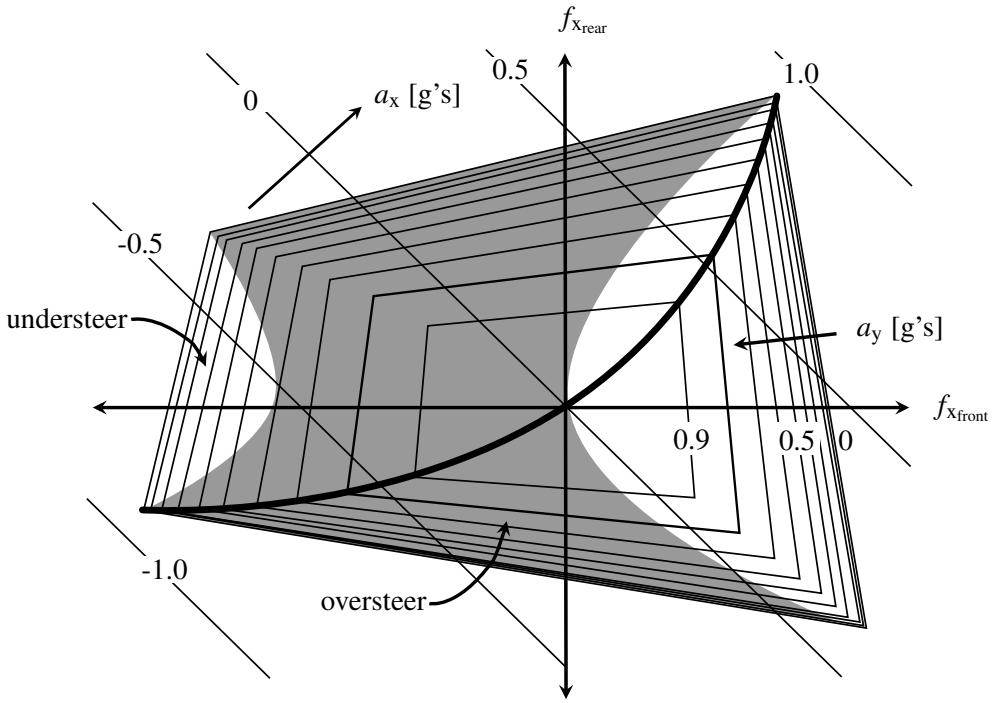

Figure 2.3: *The dynamic square*. The dynamic square is a tool that can be used to visually convey the quasi-steady state response of a vehicle based on the saturation limits of the tires [40]. This tool can be used to determine optimal force distribution to individual axles or wheels of a vehicle in a given configuration. The given illustration depicts the handling response predicted using a bicycle model (no lateral load transfer), with front and rear axle drive forces on the x-axis and y-axis respectively. The longitudinal and lateral accelerations are given by the diagonal axis and iso-lines. Regions of understeer and oversteer response are represented by the white and gray regions and the optimal tractive force distribution (black) maximizing handling capability.

With analysis tools such as the DSM, potential improvements over conventional fixed power-trains can be found. To address this potential, research focusing on the use of advanced power-train and drive systems capable of increasing the operational performance and stability of vehicles can be found in the literature. The development of all wheel drive (AWD) vehicles originated from desire for increased traction off-road. However, these systems can also be used to best utilize available grip, leading to higher acceleration and cornering performance on-road. Klomp [45] discussed the advent of passive and active driveline components for conventional road vehicles capable of

modulating drive torques to the individual vehicle drive axles, including transmissions and passive and active differentials.

An investigation of passive drivetrain layout on four wheel drive vehicle dynamics was conducted by Danesin [21]. This study evaluated the effects of mechanical open, torque sensing and limit slip differentials on vehicle handling. It was shown that torque sensing and hydraulic clutch type differentials offered best lateral handling capability in conditions where drive forces were present. The work of Lee [50] attempted to determine the interaction between stability control systems and passive drive-line viscous couplers. Since passive couplers are not electronically controlled, they can not be disconnected, causing torque transfer across an axle, reducing the capabilities of brake based stability control systems. To achieve maximum corrective moment with such brake based systems, all four wheels must act independently. However, braking one wheel in such systems can cause deep slip on the others, thus transferring torque to the unbraked wheels. To limit the impact of passive coupling differentials on VDC systems, modifications to brake based controls, detuned viscous coupling units, and the incorporation of an electronic throttle system were proposed. The use of active torque coupling devices with the capability of modulating torque transfer across the differential was proposed by Sawase [79]. The proposed systems were capable of generating a direct yaw moment about the vertical axis of the vehicle, influencing the dynamic response during cornering manoeuvres. Further study of the efficacy of such active drive-line systems was presented by Hancock [31], comparing the response to those of conventional brake based ESC systems.

Another promising power-train development is the incorporation of electric motors in hybrid electric (HEV) and electric (EV) vehicles. The design and modelling of these advanced power-train systems are presented in detail by Ehsani [25]. In general, hybrid powertrains are comprised of two power sources, namely an internal combustion engine coupled with electric motors, allowing for kinetic energy recovery through regenerative braking systems (RBS). Conventional braking systems utilize hydraulic brakes to dissipate kinetic energy, where a RBS uses the electric motor in generator mode to provide negative torque to driven wheels, converting kinetic energy to electrical energy to recharge the energy storage system. These mechanical and electrical systems may be used in concert, as in the work of Cikanek [15], which focused on the development and testing of a regenerative braking algorithm for a front wheel drive parallel hybrid electric vehicle (PHEV), providing improved performance. In this algorithm, the electric brake torque is a predetermined fraction of master cylinder pressure, modulated to ensure favourable front and rear wheel lock-up conditions. The available motor drive and braking torques are estimated using linear relationships. The proposed method was successful in modulating the electric motor during drive and brake events. Further developments in four wheel drive hybrid drivetrain operational algorithms providing improved

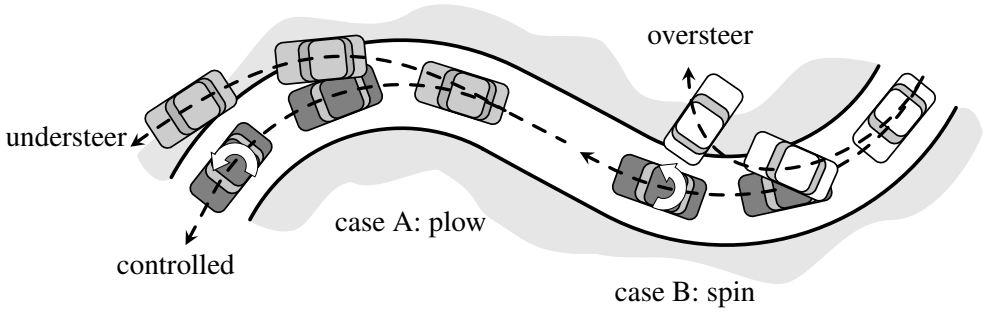

Figure 2.4: *Corrective yaw moments*. Yaw moment control strategies can be used to apply a corrective moment about the vertical axis of the vehicle to prevent loss of control situations. Case A illustrates the corrective yaw moment required to correct an understeering (light gray) vehicle. Case B illustrates the corrective yaw moment required to correct an oversteering (white) vehicle.

drive and regeneration capability are presented by Kimura [44] and Endo[27].

Within Canada, the AUTO21 Network Centres of Excellence (NCE), has funded projects focused on the design and analysis of regenerative braking technology (E03-RGB) as well as safety systems and grid interfacing for hybrid vehicle systems (E301-EHV). Work within these projects has focused on the design and evaluation of hybrid architectures, component sizing, drivetrain design and the application of regenerative braking [43, 78, 24, 22]. In particular, the work of Oh [63] indicated the implementation challenges to post-transaxle electric motor hybrid vehicles and proposed a supervisory vehicle dynamics control for regenerative braking in a front wheel drive hybrid vehicle. The proposed VDCs were shown to improve stability and performance during braking manoeuvres. It was shown that having direct electronic control over motors within a hybrid vehicle powertrain architecture can provide opportunities for advanced vehicle dynamics control.

2.3.1 Integrated Chassis Control

As discussed, various mechanical, electrical and hybrid drive systems are capable of providing forces to correct or alter inherent vehicle handling response. These systems include ABS, TCS, active steering, and brake based ESCs that can be combined to create an encompassing integrated chassis control strategy. Additionally, the advent of active transmissions and advanced hybrid vehicle architectures has made variable torque distribution (VTD) control systems feasible on consumer road vehicles. These systems have been shown to be capable of providing direct yaw moment control to correct unfavourable vehicle response and minimize loss of control situations, as illustrated in Figure 2.4.

The work of Osborn [66] proposed an AWD drivetrain with the ability to transfer torque to the outside wheel during cornering to improve the cornering limitations of front wheel, rear wheel and all-wheel-drive (AWD) vehicles. In the proposed implementation, the amount of torque transferred was determined using a control law tracking the response of an estimated neutral steering vehicle. A distributed proportional-integral control structure was used with the front-rear torque distribution based on yaw rate feedback, and left-right distribution based on lateral acceleration. The multiple input multiple output control was tuned using an experimental Box-Behaken method evaluating the sensitivity of the vehicle to control parameters. It was noted that the AWD system provided a vast handling improvement, and the front-rear torque distribution was a significant factor.

Another direct YMC method vectoring electric motor torque across a rear axle was proposed by Shino [81] for a small-scale electric vehicle. In the proposed method, steering angle dependent feed-forward steer and yaw moment controls were compensated with optimal feedback controls to reject external disturbances. The steering wheel angle was modulated by the feed-forward component only, while the yaw moment to the individual drive motors was distributed using quasi-static relationships. As measuring side slip angle directly is difficult and expensive, a linear speed dependent observer estimate of lateral slip velocity was used.

He [32] studied the efficacy of coupled active front steer (AFS), active rear steer (ARS) and variable torque distribution controls to improve yaw rate tracking in mid-range lateral acceleration using sliding mode control. A rule based control method was used with the required yaw moment based on the evaluation of the phase-plane stability region of the vehicle. This work concluded that ARS and AFS are effective in the linear range of the tire, where developed tire forces are proportional to slip angle. Alternatively, the VTD ESC becomes powerful under emergency conditions. In the proposed method, wheel torques were set using quasi-static allocation of the desired yaw moment. The work of Mokiamar [58] also evaluated the use of combined AFS, ARS, and VTD YMC. However, it was proposed that side slip control is more effective than yaw rate control in compensating lateral dynamics and loss of stability due to tire nonlinearities. Control values were determined using a linear model tracking sliding mode control and distributed with an optimum force distribution method relying on the unconstrained optimization of a linear system of equations attempting to minimize tire usage.

The use of soft computing techniques have also been used to determine and allocate desired corrective yaw moments. The work of Jalali [35] detailed the development of yaw moment control using soft computing techniques, in which yaw moments applied to the vehicle are determined using a fuzzy logic controller with triangular membership functions. In the presented work, the fuzzy logic membership functions were tuned using genetic algorithms to minimize the yaw rate and side slip error. However, the detailed method only determines the yaw moment that must be

further be allocated to the individual drive motors and chassis actuators. This could be accomplished with the previously discussed methods, or by further fuzzy methods as proposed by Buckholtz [12].

The addition of greater numbers of control effectors has been shown to improve the capabilities of VDCs. However, as the number of control actuators increases, the problem of over-actuation can occur. Over-activation occurs when there is a manifold set of actuator assignments capable of reproducing the desired control response. This over-actuation is present in the case of variable torque distribution systems and complete chassis control systems. To address this, the use of hierarchical control structures with a component for control force allocation are proposed. The work of Sakai [75] makes use of simple fixed case driven algorithms, similar to the rule based and fuzzy methods of He and Buckholtz. More advanced solutions to the over-actuation problem are found in the field of aerospace, where over-actuated control is present in roll-yaw coupled flight controls [7]. In this work, the implementation of direct, linear, optimization based and real time allocation algorithms for higher dimension control allocation problems are discussed. In general, these methods determine an optimum solution within an allowed higher dimension search space by minimizing a cost function under an imposed set of additional constraints.

Application of quadratic programming allocation techniques for road vehicles can be found in the work of Plumlee [70]. In the proposed method the effector commands are allocated based on the minimization of a quadratic cost function subject to inequality constraints. Ono [64] extends these techniques with the application of sequential quadratic programming to allow for the determination of global optimality conditions, accounting for limits in tire force generation. Andreasson *et al.* [6, 38] lends these techniques towards the development of generalized vehicle controls for global chassis control strategies for autonomous corner modules. These force constrained methods have been shown to maintain vehicle stability near the handling limit; however, these methods rely on detailed tire data, including Jacobians that must be calculated or read from large tables, making the control methods discussed computationally expensive. In general, developments providing improved allocation algorithms have lead to new integrated control approaches with the capability of optimizing the use of tire and control effectors, increasing vehicle safety. It was noted in these works that further study incorporating the driver should be conducted to evaluate the efficacy of such systems in the human operated vehicle system.

2.4 Human Driver Modelling

The human operator is an integral part of the complete vehicle system and must be considered in the analysis of vehicle and control system response. Cases can exist where the interactions between the closed-loop human control and a vehicle dynamics control could impact the vehicle response

negatively. However, a significant amount of research remains without consideration of the driver within the vehicle system. Studies attempting to quantify these interactions within closed-loop simulations can be found in the literature with driver models of varying complexity. The work of Ishio [34] evaluated the handling response of a vehicle with active front wheel steering using a proportional-derivative driver steer control to minimize lateral path error, while a slightly more complex single point model predictive control was used by Mokhiamar, and even the use of driver in the loop testing has been proposed [16]. In general, the formulations of these models vary widely in complexity and are typically developed and tuned for testing within a confined set of scenarios. A number of other models for longitudinal, lateral and combined control situations can be found in academic and commercial work [8, 54, 48, 51, 4]. The modelling approaches found in these works attempt to characterize and emulate the response of the human neuro-physiological control. These approaches can be grouped into classical linear, non-linear, fuzzy, neuro-network and hybrid control methods. Each of these approaches has inherent benefits and limitations when attempting to emulate the often nonlinear and non-deterministic human responses, as outlined in detail by Plochl [69].

It is widely believed that the efforts of a human driver occur on the macro, micro and instantaneous levels, otherwise termed navigation, guidance and stabilization [42]. Efforts in navigation are on the macro scale comprised of global route planning, such as selecting roads to get from a start to an end location. Guidance deals with the micro scale, pertaining to a finite preview period and is comprised of path error minimization and obstacle avoidance. Stabilization occurs on a more instantaneous level involved with maintaining vehicle stability. Generally, a majority of evaluation regarding vehicle dynamics controls falls within the guidance and stabilization regimes.

A body of work regarding path planning can be found in the literature largely focused on race applications [14, 17, 11]. These works present the use of advanced iterative search techniques to find the racing line around a given track geometry, yielding the minimum traversing time for a given vehicle model. These search techniques rely on *a priori* knowledge of the problem to improve convergence of the search techniques. Another potential method for path determination involves the use of genetic algorithms as proposed by Lu [52] and Wang [85]. These genetic search algorithms generate and evaluate potential solutions using biologically based algorithms, where convergence can be achieved with minimal *a priori* knowledge. Regardless of the method, the large and complex search problem poses challenges relating the description of the road environment to the optimization problem, leading to difficulties in guaranteeing convergence to absolute maxima and minima.

Research conducted at the University of Michigan Transportation Research Center (UMTRI) lead to the development of a set of preview based model predictive control driver steering models capable of replicating driver steering inputs through various manoeuvres within set operational and emergency conditions [54, 84]. These models determine steer inputs by minimizing a penalty

function relying on a simplified internal vehicle model to predict the future path of the vehicle. It has been shown that the two degree of freedom yaw-plane model is sufficient in predicting future vehicle states with determined steer angles, correlating well with experimental data. Within these works the effect of driver preview time has been shown to have a significant effect on the accuracy of the predicted steer inputs, and must be carefully determined to provide the desired response.

In the majority of literature surveyed, the control tasks of the driver in the longitudinal direction are ignored. Kienke [42] presented the comprehensive characterization of the mental and physical response of the human driver. Within the proposed structure, a finite state machine was proposed to emulate the mental tasks of a driver in setting appropriate reference states for longitudinal motion. In this method the finite state machine is presented as an abstraction of the non-deterministic rules and actions of the driver. A set of operating regimes with specific actions and rules are defined, detailing straight-line and cornering processes. The model developed was capable of modulating throttle and brake commands, given preview information of the intended path of the vehicle.

Using experimental testing, Ishiro [34] concluded that the driver adapts to the vehicle handling characteristics of a controlled vehicle over time. However, a learning period may be required to accurately predict vehicle response to inputs. In an emergency situation a driver may not have time to adapt to unexpected vehicle responses imposed by an applied vehicle dynamics control. Therefore, it may be beneficial to model the response of the driver in the closed-loop vehicle dynamics simulations.

Chapter 3

Dynamic Modelling and Analysis

This chapter presents a set of modelling and analysis techniques well suited for the design and analysis of road vehicles. The models developed are utilized in subsequent chapters focusing on human driver modelling and control system development. To illustrate the techniques in detail, the modelling of a 2006 BMW 330i with validation is presented. A series of models of increasing complexity are developed and evaluated to determine their efficacy in predicting vehicle response.

3.1 Equations of Motion

To accurately predict the response of a system, a dynamic model requires sufficient definition of the elements, configuration and acting forces of the system. To this end, the kinematic and kinetic relationships within, and acting on the system must be considered. This leads to the formulation of a set of governing equations for analysis and simulation. Several methods exist to generate equations of motion of mechanical, electrical and hybrid systems, including the Newton-Euler method based on the relationship between applied forces and resulting motions expressed as

$$\begin{aligned} \sum \boldsymbol{f}_{\mathrm{a}} &= m\dot{\boldsymbol{v}} + \boldsymbol{\omega} \times m\boldsymbol{v} \\ \sum \boldsymbol{\tau}_{\mathrm{a}} &= \mathbf{I}\dot{\boldsymbol{\omega}} + \boldsymbol{\omega} \times \mathbf{I}\boldsymbol{\omega} \end{aligned} \tag{3.1.1}$$

where $\boldsymbol{f}_{\mathrm{a}}$ is a vector of applied forces, and $\boldsymbol{\tau}_{\mathrm{a}}$ is a vector of applied moments. The mass of the body is given by m, and the inertia tensor is given by the $\mathbf{I}$. The translational and rotational velocities expressed in the body-fixed rotating frame are $\boldsymbol{v}$ and $\boldsymbol{\omega}$ respectively. Defining and substituting a new state vector

$$\boldsymbol{w} = \begin{Bmatrix} \boldsymbol{v} \\ \boldsymbol{\omega} \end{Bmatrix} \tag{3.1.2}$$

and force vector

$$\boldsymbol{f} = \begin{Bmatrix} \boldsymbol{f}_{\mathrm{a}} - \boldsymbol{\omega} \times \mathbf{mv} \\ \boldsymbol{\tau}_{\mathrm{a}} - \boldsymbol{\omega} \times \mathbf{I}\boldsymbol{\omega} \end{Bmatrix} \tag{3.1.3}$$

and mass matrix

$$\mathbf{M} = \begin{bmatrix} \mathbf{m} \cdot \mathbf{I}_{\mathrm{d}} & \mathbf{0} \\ \mathbf{0} & \mathbf{I} \end{bmatrix} \tag{3.1.4}$$

into the set of Newton-Euler relationships, we get the general nonlinear multibody form of the equation of motion

$$\sum \boldsymbol{f} = \mathbf{M}\dot{\boldsymbol{w}} \tag{3.1.5}$$

3.1.1 Linear System Analysis

In reality most systems are nonlinear due to friction and other nonlinear effects. However, in a majority of cases, linear approximations about operational or equilibrium points can provide important understanding of the response of these systems. The use of linear models allows for the application of linear systems theory and control. However, in systems where large nonlinearities such as discontinuities occur near the linearization point, the equations developed may only be valid in a limited range about the linearization point.

Considering the constraints on the system, a coordinate reduction can be completed. Further applying simplifying assumptions, and linearizing Equation 3.1.5 about an operational point, the classic mass-damping-stiffness form (MCK) expressed as

$$\mathbf{M}\ddot{\boldsymbol{x}}_{\mathrm{i}} + \mathbf{C}\dot{\boldsymbol{x}}_{\mathrm{i}} + \mathbf{K}\boldsymbol{x}_{\mathrm{i}} = \boldsymbol{f}_{\mathrm{a}} \tag{3.1.6}$$

where $\mathbf{M}$ is the mass matrix, $\mathbf{C}$ is the damping matrix and $\mathbf{K}$ is the stiffness matrix given the state vector $\boldsymbol{x}$. Equation 3.1.6 is a set of ordinary differential equations (ODEs) that represent the dynamical response of the system, that can be further classified as linear time invariant (LTI) if the components of the matrices are not a function of time. The resulting LTI system can be further manipulated into first order form as

$$\begin{Bmatrix} \dot{\boldsymbol{x}}_{\mathrm{i}} \\ \ddot{\boldsymbol{x}}_{\mathrm{i}} \end{Bmatrix} = \begin{bmatrix} \mathbf{0} & \mathbf{I_d} \\ -\mathbf{M}^{-1}\mathbf{K} & -\mathbf{M}^{-1}\mathbf{C} \end{bmatrix} \begin{Bmatrix} \boldsymbol{x}_{\mathrm{i}} \\ \dot{\boldsymbol{x}}_{\mathrm{i}} \end{Bmatrix} + \begin{bmatrix} \mathbf{0} \\ \mathbf{M}^{-1} \end{bmatrix} \boldsymbol{f}_{\mathrm{a}} \tag{3.1.7}$$

where $\mathbf{I}_d$ is the identity matrix. In most systems, the state is not directly measurable, so a vector of outputs can be added, completing the state-space formulation

$$\begin{aligned} \dot{\boldsymbol{q}} &= \mathcal{A}\boldsymbol{q} + \mathcal{B}\boldsymbol{u} \\ \boldsymbol{z} &= \mathcal{C}\boldsymbol{q} + \mathcal{D}\boldsymbol{u} \end{aligned} \tag{3.1.8}$$

where the state vector $\boldsymbol{q}$ and the vector of inputs $\boldsymbol{u}$ are related to the state derivatives and dependent outputs $\boldsymbol{z}$ by the system matrices $\mathcal{A}$, $\mathcal{B}$, $\mathcal{C}$ and $\mathcal{D}$. It should be noted that this first order state-space form of the equations of motion is now readily suited for computer simulation and analysis. The stability of a system can be inferred from the eigenvalues of the characteristic equations of the system model. This is accomplished considering the characteristic solutions of the set of ODEs, such that

$$\dot{\boldsymbol{q}} = \mathcal{A}\boldsymbol{q} \tag{3.1.9}$$

assuming the solution

$$\begin{aligned} \boldsymbol{q} &= \hat{\boldsymbol{q}} e^{st} \\ \dot{\boldsymbol{q}} &= \hat{\boldsymbol{q}} s e^{st} \end{aligned} \tag{3.1.10}$$

where $\hat{\boldsymbol{q}}$ is a vector of constants, s is the Laplace variable and t is time. Substituting this assumed solution into Equation 3.1.9 and solving $[s\mathbf{I}_d - \mathbf{A}]\,\hat{\boldsymbol{q}} = \mathbf{0}$ yields the set of complex characteristic values $s = a + b\imath$. The homogeneous solution for the states with respect to time is now given

$$\boldsymbol{q}(t) = \hat{\boldsymbol{q}}_1 e^{s_1 t} + \hat{\boldsymbol{q}}_2 e^{s_2 t} + \ldots + \hat{\boldsymbol{q}}_n e^{s_n t} \tag{3.1.11}$$

where n is equal to the number of characteristic values of the system. It can be shown that positive real components will produce exponential growth with amplitudes tending to infinity. Responses with negative real parts exhibit amplitudes tending towards zero. With this technique the real parts of the eigenvalues can be used to infer system stability, while the imaginary parts indicate oscillation about the equilibrium or linearization point.

3.1.2 Automatic Generation of the Equations of Motion

In general, hand derived equations of motion are possible for simple systems with limited degrees of freedom or where linearizing assumptions are valid. However, as the size of the system increases or where significant nonlinearities are present, it becomes increasingly difficult to generate the equations of motion by hand. To address this, several techniques for automatic generation of the equations of motion have been proposed and marketed commercially over the past few decades. The equations of motion developed by most of these techniques are suitable for computer implementation and are nonlinear. These nonlinear equations are not ideally suited for conventional control or eigenvalue analysis, where linearized equations are favoured. Many methods producing linear equations for systems with holonomic constraints apply a linearization of the equations of motion, followed by a reduction to first order form [56]. However, adoption of this method can be difficult or impossible in systems with nonholonomic constraints (constraints that can not be expressed in

terms of positions alone). The yaw-plane model previously presented takes this form, with three position coordinates and only two velocity coordinates, as the forward speed is parameterized, leading to nonlinear terms appearing in the linearized formulation.

The generation of equations of motion for systems with nonholonomic constraints requires a different approach. A method of automatically generating the linearized equations of motion for mechanical systems allowing for the inclusion of nonholonomic constraints was proposed and developed by Minaker and Rieveley [57]. This method has been implemented in computer software named Equations of Motion (EoM) and has been shown to be well suited to vehicle stability analysis. In this method, the equations of motion are formed using a novel approach, first reducing the system to first order form and then linearizing the equations of motion. The resulting first order form can be expressed as

$$\begin{bmatrix} \mathbf{I}_\mathrm{d} & \mathbf{0} \\ \mathbf{0} & \mathbf{M} \end{bmatrix} \begin{Bmatrix} \dot{\boldsymbol{p}} \\ \dot{\boldsymbol{w}} \end{Bmatrix} + \begin{bmatrix} \mathbf{V} & -\mathbf{I}_\mathrm{d} \\ \mathbf{K} & \mathbf{C} \end{bmatrix} \begin{Bmatrix} \boldsymbol{p} \\ \boldsymbol{w} \end{Bmatrix} = \begin{Bmatrix} 0 \\ \boldsymbol{f}_\mathrm{c} + \boldsymbol{f}_\mathrm{a} \end{Bmatrix} \tag{3.1.12}$$

where $\boldsymbol{p}$ is a vector of global coordinates, and $\boldsymbol{w}$ is a vector of local velocities, $\mathbf{V}$ contains the constant linear velocities, $\boldsymbol{f}_\mathrm{c}$ are the constraint forces and $\boldsymbol{f}_\mathrm{a}$ are the applied forces. The linearized constraint equations can be expressed as

$$\begin{bmatrix} \mathbf{B}_\mathrm{h} & \mathbf{0} \\ -\mathbf{B}_\mathrm{h}\mathbf{V} & \mathbf{B}_\mathrm{h} \\ \mathbf{0} & \mathbf{B}_\mathrm{nh} \end{bmatrix} \begin{Bmatrix} \dot{\boldsymbol{p}} & \boldsymbol{p} \\ \dot{\boldsymbol{\omega}} & \boldsymbol{\omega} \end{Bmatrix} = \begin{bmatrix} 0 & 0 \\ 0 & 0 \\ 0 & 0 \end{bmatrix} \tag{3.1.13}$$

The constraints can now be removed considering the holonomic and nonholonomic constraints as

$$\begin{bmatrix} \mathbf{B}_\mathrm{h} & \mathbf{0} \\ -\mathbf{B}_\mathrm{h}\mathbf{V} & \mathbf{B}_\mathrm{h} \\ \mathbf{0} & \mathbf{B}_\mathrm{nh} \end{bmatrix} \mathbf{R} = \mathbf{0} \tag{3.1.14}$$

and

$$\begin{aligned} \mathbf{B}_\mathrm{h}\mathbf{L}_\mathrm{u} &= \mathbf{0} \\ \begin{bmatrix} \mathbf{B}_\mathrm{h} \\ \mathbf{B}_\mathrm{nh} \end{bmatrix} \mathbf{L}_\mathrm{l} &= \mathbf{0} \end{aligned} \tag{3.1.15}$$

giving

$$\mathbf{L} = \begin{bmatrix} \mathbf{L}_\mathrm{u} & \mathbf{0} \\ \mathbf{0} & \mathbf{L}_\mathrm{l} \end{bmatrix} \tag{3.1.16}$$

where $\mathbf{R}$ and $\mathbf{L}$ are the orthogonal compliments providing a reduced set of coordinates satisfying

the holonomic and nonholonomic constraint equations represented by $\mathbf{B}_{\mathrm{h}}$ and $\mathbf{B}_{\mathrm{nh}}$. The reduced dimension first order form can expressed as

$$\begin{aligned} \mathcal{A} &= -\left[\mathbf{L}^{\mathrm{T}}\begin{bmatrix}\mathbf{I}_{\mathrm{d}} & \mathbf{0}\\ \mathbf{0} & \mathbf{M}\end{bmatrix}\mathbf{R}\right]^{-1}\mathbf{L}^{\mathrm{T}}\begin{bmatrix}\mathbf{V} & -\mathbf{I}_{\mathrm{d}}\\ \mathbf{K} & \mathbf{C}\end{bmatrix}\mathbf{R} \\ \mathcal{B} &= \left[\mathbf{L}^{\mathrm{T}}\begin{bmatrix}\mathbf{I}_{\mathrm{d}} & \mathbf{0}\\ \mathbf{0} & \mathbf{M}\end{bmatrix}\mathbf{R}\right]^{-1}\mathbf{L}^{\mathrm{T}}\begin{bmatrix}\mathbf{0}\\ \mathbf{I}_{\mathrm{d}}\end{bmatrix} \end{aligned} \tag{3.1.17}$$

where $\mathcal{A}$ and $\mathcal{B}$ are the state and input matrices. The state equation can be extended to provide system output with

$$\begin{aligned} \mathcal{C} &= \mathbf{S}\begin{bmatrix}\mathbf{RI} & \mathbf{R}\mathcal{A}^{i} & \cdots & \mathbf{R}\mathcal{A}^{n-1}\end{bmatrix}^{\mathrm{T}} \\ \mathcal{D} &= \mathbf{D}\begin{bmatrix}\mathbf{0} & \mathbf{R}\mathcal{A}^{i-1}\mathcal{B} & \cdots & \mathbf{R}\mathcal{A}^{n-1}\mathcal{B}\end{bmatrix}^{\mathrm{T}} \end{aligned} \tag{3.1.18}$$

where $\mathbf{S}$ and $\mathbf{D}$ are output selection matrices for the augmented state with $i = 1, 2, \ldots, n$, where the augmentation level for the highest order sensor can be expressed as

$$n = \max\left(\left\lceil s_{\mathrm{o}} + \frac{s_{\mathrm{f}}}{2} - 2\right\rceil\right) \tag{3.1.19}$$

where s_{o} and s_{f} are vectors of the sensor orders (eg. 1, 2, 3) and reference frames ($s_{\mathrm{f}_{\mathrm{local}}} = 0$ and $s_{\mathrm{f}_{\mathrm{global}}} = 1$). The system output formulation allows for sensor output in the local or global reference frames. This method has been shown to be effective in producing equations of motion for small and large systems where the application of hand derived equations would be difficult, if not impossible.

3.2 Vehicle Modelling

In general, the modelling techniques discussed can be applied to larger systems and more specific applications, including the modelling of road vehicles. However, the presence of nonlinearities within the suspensions and tires can complicate the application of these techniques, warranting a detailed discussion on the dynamic nature of these elements.

3.2.1 The Pneumatic Tire

Aside from gravitational and wind forces acting on a conventional road vehicle, all other forces of motion are generated by interactions contained within the regions of contact between the tires and the road, termed the contact patches. Despite a simple exterior appearance, pneumatic tires are complex structures combining rubber, metal and composite materials, as shown in Figure 3.1. This

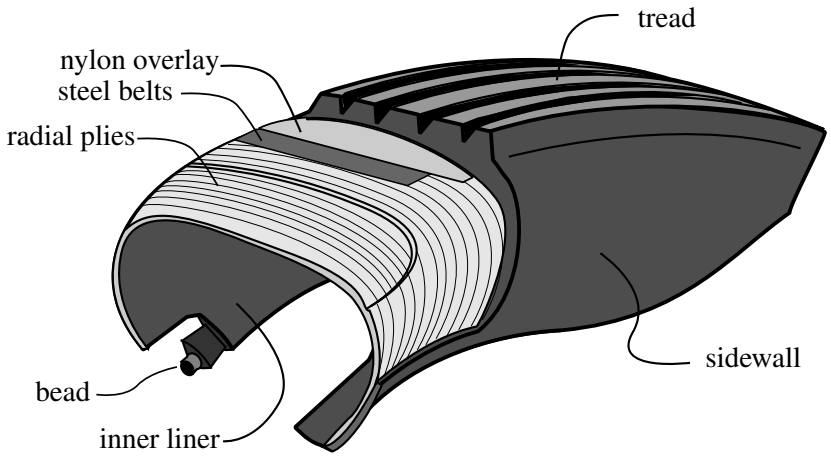

Figure 3.1: *Pneumatic tire construction*. Conventional road vehicle tires are complex hybrid structures composed of rubber, steel and composite fibres designed to meet desired vertical, longitudinal and lateral loading requirements.

hybrid structure is required to achieve the desired vertical, longitudinal and lateral forces, while meeting other secondary criteria such as low rolling resistance and noise production. Treatments on the nonlinear nature of tire force generation vary in complexity and scope; however, certain underlying theories exist, allowing for fundamental understanding of tire force generation [55, 67]. In general, forces are generated by a combination of three phenomenon: slipping, gearing, and chemical adhesion. The amount of each phenomenon present within the contact patch relies heavily on the construction and materials of both the tire and road surface.

Pure and Combined Slip

The most significant component of tire force is generated through longitudinal or lateral slip within the tire-road contact patch. Slip occurs due to deformations in the tire sidewalls and treads in the presence of acting forces and moments, causing parts of the tire to slide across the road surface within the contact patch.

In the longitudinal case the driving moment on the tire causes the exterior band of the tire to compress circumferally when it strikes the road surface. This deformed region of the tire must return to undeformed condition at the point when it separates from the road surface, as shown by the brush model in Figure 3.2. This causes slip to occur between the tire and the road as the tire transitions from the deformed to the undeformed state. As the drive torque increases, the fraction of surface area in the contact patch that slips will increase, until the entire surface is slipping. The slip ratio is

defined as the percent difference in longitudinal velocity between the wheel and the contact patch expressed as

$$\kappa = \frac{\omega r_e - u_{cp}}{u_{cp}} \tag{3.2.1}$$

where κ is the slip ratio, ω is the rotational speed of the wheel, r_e is the effective radius and u_{cp} is the speed of the contact point in the longitudinal direction of the tire. Similarly, force in the lateral direction is generated as the tire rolls, leading to the definition of the slip angle, which is the difference between steered angle of the tire and actual rolling direction, as illustrated in Figure 3.2. A shear deformation occurs as the tire rolls, causing the tire to follow a path less than the steered angle of the wheel.

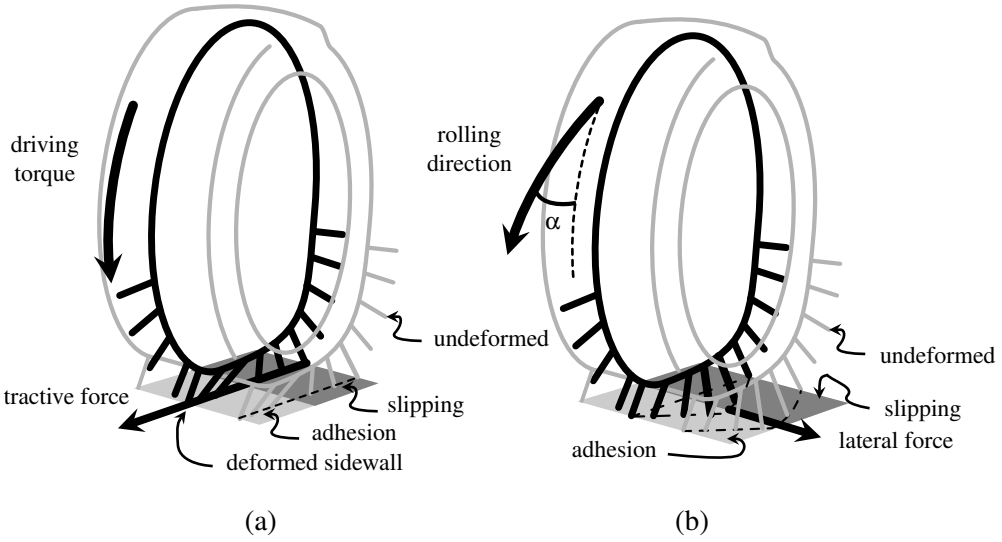

Figure 3.2: *Brush tire model*. The brush model can be used to visualize tire force generation in the presence of longitudinal and lateral slip. (a) illustrates the case of pure longitudinal slip in which the driving torque on the wheel compresses the tire when it comes into contact with the road surface, the compressed region of the tire carcass must return to an undeformed state when it separates from the road surface. (b) illustrates the case of pure lateral slip as the difference in rolling and pointed direction of the tire causes lateral deformation in the tire carcass. The adhesion and sliding of the tire with the road surface generates tractive and lateral forces. Figure adapted from [67].

In reality the lateral and longitudinal forces generated by a tire are interdependent and there is a maximum resultant force that can be generated within the contact patch. In cases with combined loading, the resultant force has a finite limit that can be expressed as a function of the vertical load

on the tire and the friction coefficient of the tire-road contact. The force generation limit acts in all directions, leading to the concept of the friction ellipse presented in [55]. The friction ellipse defines the maximum amount of adhesion potential of a tire in a given operating condition, as shown in Figure 3.3. In general, the limit is elliptical and asymmetric due to load in the tire belts that cause the centre of contact to migrate within the contact patch. However, the elliptical nature of the limit envelope can be closely approximated by

$$1 = \left(\frac{f_{\mathrm{x}}}{f_{\mathrm{x_{max}}}}\right)^2 + \left(\frac{f_{\mathrm{y}}}{f_{\mathrm{y_{max}}}}\right)^2 \tag{3.2.2}$$

where f_{x} and f_{y} are the longitudinal and lateral forces in the tire reference frame. The normalized tire force or safety margin of a tire expressing the amount of tire grip used can be written as

$$\eta = \frac{\sqrt{f_{\mathrm{x}}^2 + f_{\mathrm{y}}^2}}{f_{\max}(\mu, \ldots, f_{\mathrm{z}})} \tag{3.2.3}$$

where $f_{\max}(\mu, \ldots, f_{\mathrm{z}})$ is the maximum allowed resultant force on a tire for given operational condition.

Load Sensitivity

The force generation of a tire is nonlinearly dependent on the vertical loading of the tire, as doubling the load on a tire does not double the force generated by the tire. Understanding this phenomenon is important, as weight is transferred longitudinally and laterally across the vehicle in the presence of accelerations, due to inertial effects. In the presence of load transfer, the average lateral load capability of the vehicle or a given axle pair is less than the static condition as shown in Figure 3.4.

Inclination, Transient and Additional Effects

Tires are effected by other transient and physical conditions that are outside the scope of the present study, but should be mentioned for completeness. Changes in contact patch pressure distribution due to the inclination angle between the road surface normal and the wheel vertical axis can alter the amount of slip between the tire and the road. This variation in the amount of slip can alter the force generating capability of the tire. It has also been shown that tire forces are not generated instantaneously, requiring approximately one third and two thirds of a wheel revolution to reach steady-state in the longitudinal and lateral cases respectively. Tire pressure and temperature have also been shown to influence mechanical gearing and chemical adhesion between tire and road surface. Further less significant effects exist and are discussed in detail by Pacejka [67].

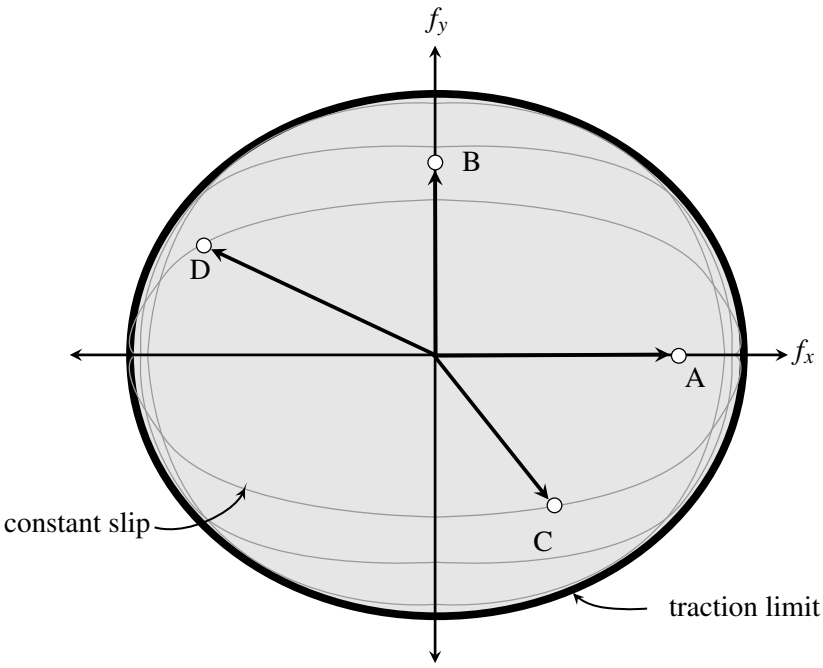

Figure 3.3: *Single tire friction ellipse*. The single tire traction ellipse graphically illustrates the limits of traction. Constant combined slip lines (gray) are shown, with the resultant force limit (black). Cases A and B illustrate pure longitudinal drive and lateral cornering force respectively, where cases C and D present combined loading cases.

Tire Modelling

Due to the complex nonlinear nature of tire force generation, the modelling of tires has grown to be a research field unto itself, with a wide variety of models available for varied purposes and levels of accuracy. As discussed in the preceding section, tires are the main generation point of forces acting on a vehicle, so a chosen model must sufficiently replicate the required dynamic and kinematic effects. As the operational conditions become more demanding, linear approximations become less applicable and more detailed models are required. These advanced models incorporating large amounts of slip, combined slip, large inclination angles, dynamic friction coefficients, and vertical contact variations are detailed by Pacejka [67]. Generally, models vary from purely empirical curve fits to purely theoretical closed form solutions, and combinations of the two classifications. The resulting models vary in the amount of investment required, fit quality and the level understanding of tire behaviour that can be obtained.

In practice, the most widespread tire models are empirical curve fits to experimental data using a

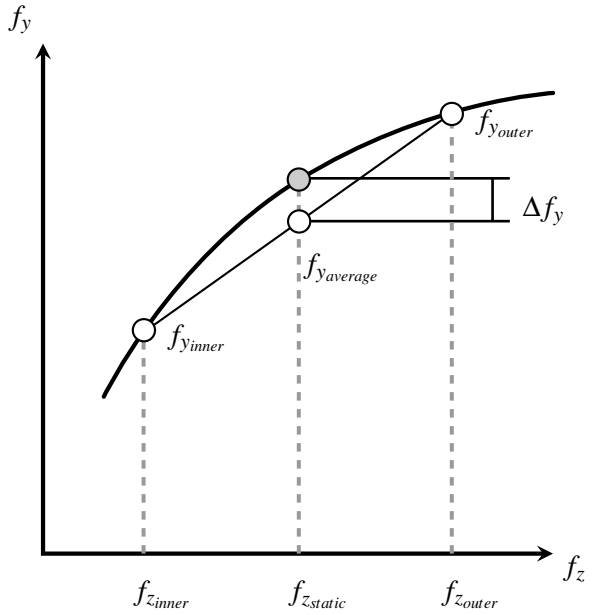

Figure 3.4: *Load transfer sensitivity*. This figure illustrates the effects of load transfer on the force generating capability of a tire relative to vertical load (black line). In the presence of load transfer during cornering, a reduction in average force Δf_y generated by the inside and outside tires of the vehicle can be seen when compared to the static case (gray).

limited number of coefficients that preferably relate to physical characteristics of the tire. The most widely accepted, the Magic Formula developed by Pacejka at the Delft University of Technology, produces a good fit to experimental data with coefficients that exhibit clear relationships to physical quantities. This formulation is directly applicable to computer simulation and specifically where real-time data is required. The formulation of the tire force is given as

$$\begin{aligned} f(\kappa_*) &= k_{\mathrm{d}} \sin\left(k_{\mathrm{c}} \tan^{-1}\left(k_{\mathrm{b}}\kappa_* - k_{\mathrm{e}}[k_{\mathrm{b}}\kappa_* - \tan^{-1}(k_{\mathrm{b}}\kappa_*)]\right)\right) \\ \kappa_* &= \kappa + k_{\mathrm{h}} \\ f^*(\kappa_*) &= f(\kappa_*) + k_{\mathrm{v}} \end{aligned} \tag{3.2.4}$$

where, $f(\kappa_*)$ can represent longitudinal force given slip ratio κ, or lateral force and aligning moments given slip angle α.

In an attempt to reduce the dependence on empirical models, the work of Salaani [76] in conjunction with the Transportation Research Center proposed an analytical model for predicting forces and moments for vehicle handling simulations. In this model, tire forces are determined using a set

of theoretical relationships valid for the full range of longitudinal, lateral and combined slip conditions up to extreme handling manoeuvres. Model parameters such as lateral and longitudinal stiffnesses, aligning moment pneumatic trail, overturning moment arm, lateral force relaxation length and friction properties are used in the formulation. A set of tire force predictions presenting the longitudinal, lateral and aligning moments of a Bridgestone P255/35R18 tire using this method are shown in Figure 3.5.

In the figures for the Bridgestone P255/35R18, the tire dependence on vertical loading can be seen, as for a given slip angle or ratio the corresponding ground plane forces increase with the vertical loading on the tire. However, this relationship is not linear, leading to reduced force generation capability in the presence of load transfer, as discussed in Section 3.2.1. It should be noted that the data presented is for a sport tire and that the load transfer effect would differ for a less sport-tuned tire. The planar force plot illustrates the friction ellipse of the tire at the extreme limit operating conditions. In the limit condition, an increase in the longitudinal force requires a corresponding reduction in the lateral force to maintain a constant amount of total slip.

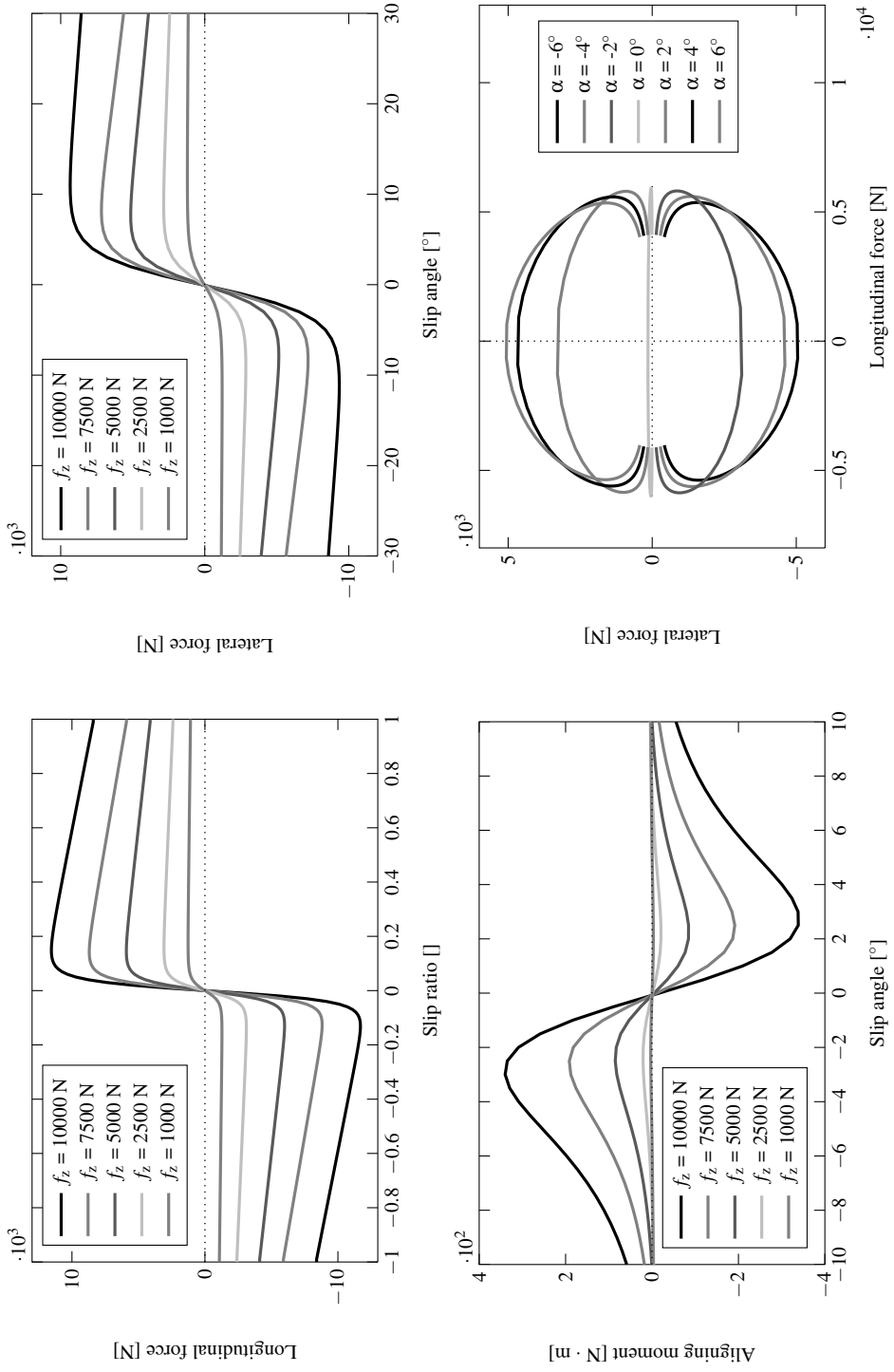

Figure 3.5: *Longitudinal, lateral and aligning moment tire force: Bridgestone P255/35R18.* The top left, top right and bottom left present the longitudinal force, lateral force and aligning moment with respects to slip and vertical load, generated using the Salaani tire model [76]. The bottom right illustrates the friction ellipse for the tire at various slip angles, with a vertical load of 5000 N.

3.2.2 Vehicle Data

To illustrate the methods developed during the course of this study, a 2006 BMW 330i shown in Figure 3.6 was modelled. The BMW 330i is a medium sized sport saloon car with symmetric Macpherson strut type front suspensions and five-link rear suspensions. The vehicle was chosen as detailed parameter and test data was available courtesy of Dr. Gary Heydinger [1], as well as previously published benchmark results [77, 33]. The relevant vehicle inertial parameters, suspension kinematics and tire force data used to develop the various vehicle models presented are detailed in Appendix A.

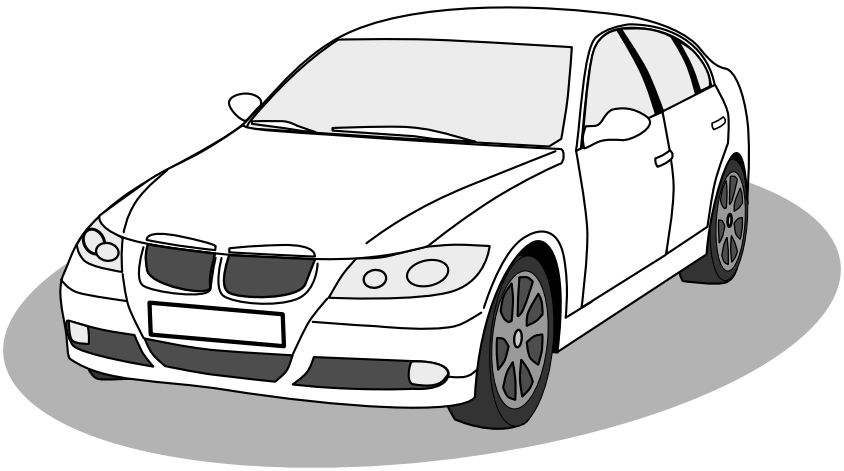

Figure 3.6: *2006 BMW 330i*. The figure illustrates the 2006 BMW 330i modelled for the purpose of this study. The relevant vehicle parameters and data detailing this model can be found in Appendix A.

3.3 Models and Analysis

3.3.1 Yaw-Plane Model

As detailed in [26], the nominal lateral and yaw motions of a road vehicle travelling at a constant forward speed can be evaluated utilizing the yaw-plane model. The equations of motion of the two DOF model can be readily developed by hand or automatically generated using the method presented in Section 3.1.2. A subsequent eigen-analysis can then be conducted to infer the vehicle stability. It is desirable that the fundamental motions of the vehicle be stable in the designed and expected configurations within the operational speed range. To evaluate the stability of the 2006 BMW 330i, a

Table 3.1: *Yaw-plane model configuration parameters: 2006 BMW 330i.*

Configuration	ζ_{us} [°/g]	Mass [kg]	Front axle-CG [m]	Front Stiffness [N/rad]	Rear Stiffness [N/rad]
A - nominal	0.072	1718.5	1.37	86488	87410
B - forward CG	0.479	1718.5	1.10	97350	75331
C - rearward CG	-0.185	1718.5	1.60	76150	99171

set of vehicle models in varying configurations were generated. These models were generated in the given nominal configuration, as well as configurations with the centre of gravity moved forward and rearward of the nominal position. These configurations were chosen as they were at or near the expected variations that could be caused by vehicle loading conditions. The parameters of each configuration including the centre of gravity location (CG), lateral cornering stiffness of each tire and understeer gradient are given in Table 3.1. The linear tire cornering stiffnesses were determined using a software implementation of the Salaani tire model in the given static loading condition. It can be inferred from the understeer gradient that the nominal, forward CG and rearward CG vehicle configurations exhibit neutral steering, mildly understeering and mildly over-steering behaviour.

Using the yaw-plane model presented in Equation 2.2.3 the system matrices for the nominal configuration at 25 m/s can be determined by hand as

$$\mathcal{A} = \begin{bmatrix} -7.167 & -24.885 \\ 0.080 & -9.553 \end{bmatrix}, \mathcal{B} = \begin{bmatrix} 0.099 \\ 0.095 \end{bmatrix}, \mathcal{C} = \begin{bmatrix} 1 & 0 \\ 0 & 1 \end{bmatrix}, \mathcal{D} = \begin{bmatrix} 0 \\ 0 \end{bmatrix} \tag{3.3.1}$$

where the steering input was defined as degrees of steering wheel. To improve the speed of analysis, a set of models were developed by automatically generating the equations of motion using the EoM implementation of the presented method. These models were comprised of a single body, with flex-point speed dependent linear damping elements at the front and rear axle locations, with a linear actuator element in the lateral direction at the front axle present to allow for steering input. The body was constrained to planar motion with a nonholonomic forward speed constraint. The system matrices for the automatically generated nominal configuration model at 25 m/s and the EoM input file describing the documented configurations are given in Appendix A. It can be seen that the hand derived and automatically generated equations of motion match, with extra coordinates present in the automatically generated model. The system can be further reduced, but has been left in its complete form for illustrative purposes.

One benefit of automatic generation of the equations of motion is that the effect of forward speed on the eigenvalues of the system models can be readily evaluated. The eigen-response of

the nominal configuration as a function of speed is shown in Figure 3.7. In the figure the rigid body mode associated with the lateral motion of the vehicle has been removed for clarity, with the remaining eigenvalue shown. It can be seen that the real parts of the eigenvalues are negative inferring system stability. The response also exhibits exponential decay below 22 m/s, transitioning to stable oscillatory response above. The natural frequency at the transition speed is 1.34 Hz.

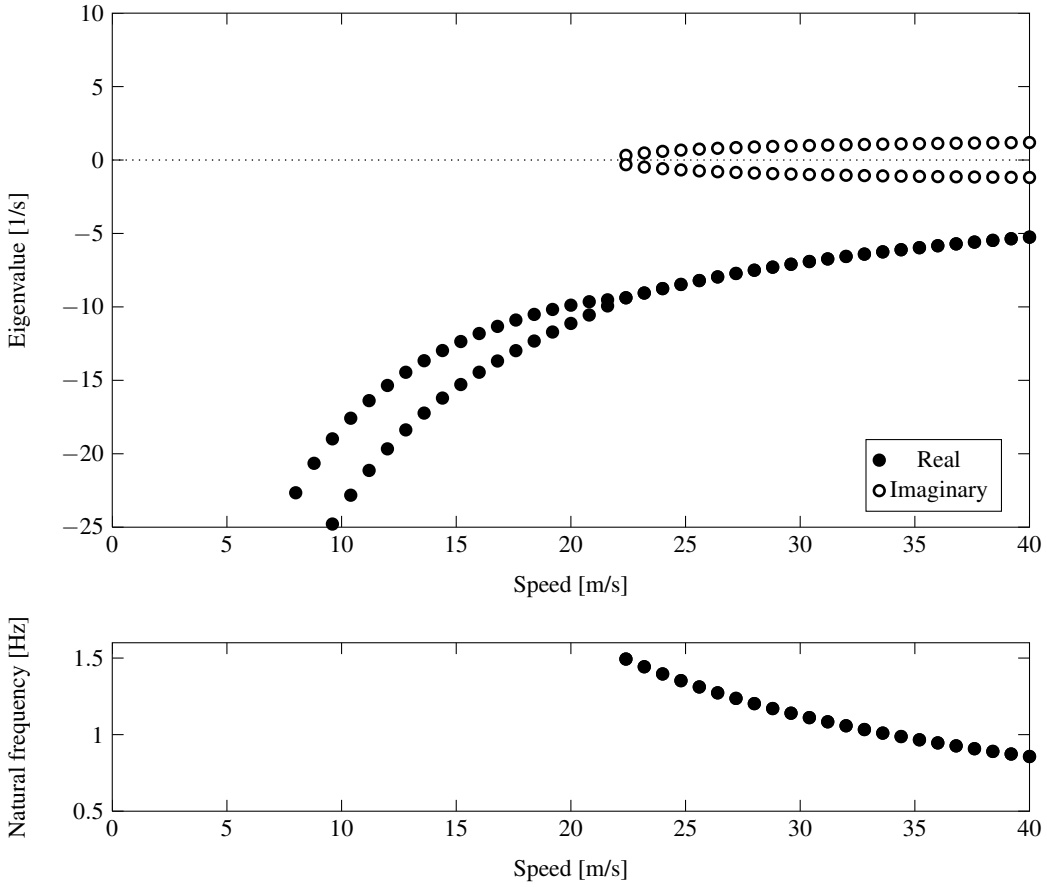

Figure 3.7: *BMW 330i eigenvalues vs. forward speed: nominal configuration*. The free response of the nominal configuration yaw-plane model exhibits understeer behaviour with exponentially decaying yaw response becoming stable-oscillatory response at 22 m/s, with a natural frequency of 1.34 Hz.

The effect of vehicle parameters on the eigenvalues of the vehicle were also evaluated. The effects of centre of gravity location are presented in Figures 3.8 and 3.9. As expected, Figure 3.8 reveals that moving the centre of gravity forward reduces the speed at which the response transitions from exponential to oscillatory decay. This transition now occurs at a forward speed of 10 m/s. It can

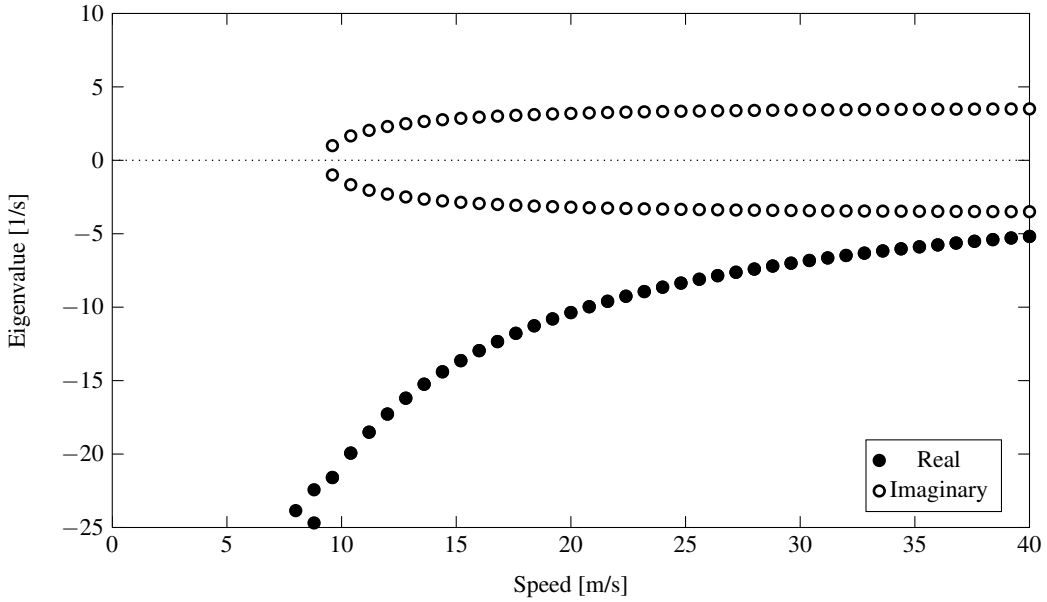

Figure 3.8: *BMW 330i eigenvalues vs speed: forward centre of gravity* In the forward centre of gravity configuration, the initial forward speed at which oscillation occurs decreases to approximately 10 m/s.

be seen that the vehicle remains stable throughout the operational range of speeds, as the real part of the eigenvalues remains negative. Figure 3.9 shows that moving the centre of gravity rearward causes the vehicle to exhibit exponential decay response throughout the tested speed range. It can be seen that the real part of the eigenvalues associated with yaw response remain negative, and the system remains stable. However, at high speed the stability is reduced, as the vehicle approaches the critical speed. At the critical speed of 91.41 m/s, the real component of the eigenvalues becomes positive leading to exponential growth. The predicted critical speed given by the yaw-plane model is much higher than the maximum operational speed of the vehicle and is not expected to be reached in normal operation.

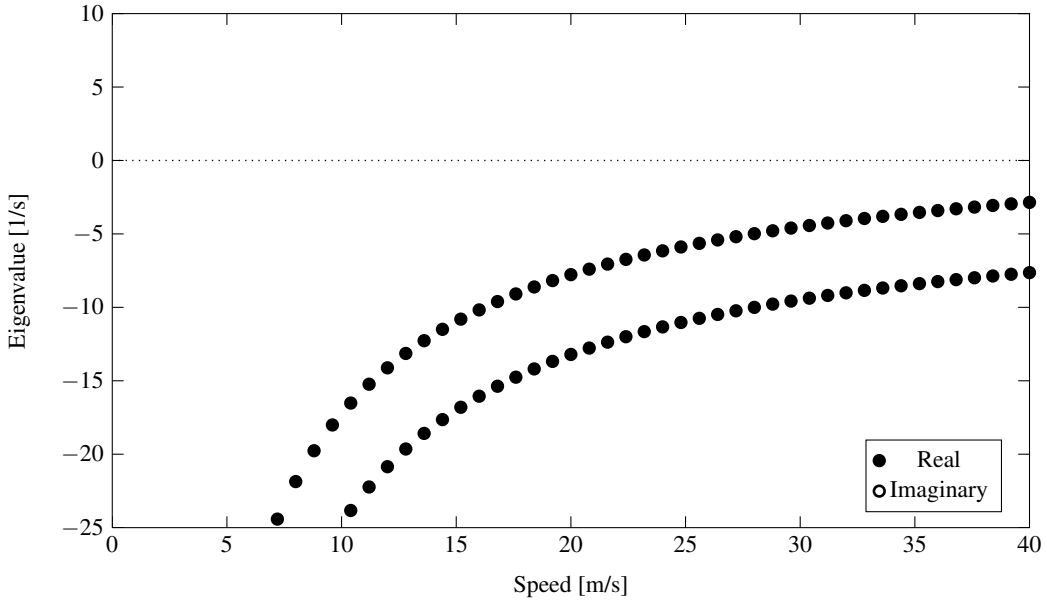

Figure 3.9: *BMW 330i eigenvalues vs speed: rearward centre of gravity* The response of the rearward centre of gravity configuration exhibits exponential decay over the tested speed range.

3.3.2 Multibody Model

It was inferred from the preceding analysis using the two DOF yaw-plane model that the lateral and yaw motions of the modelled vehicle were stable. However, this model assumed that the vehicle was comprised of a single body, and may have ignored important degrees of freedom present in the full vehicle system. To evaluate these added degrees of freedom, a full multibody vehicle model was created using the previous EoM implementation. This model was comprised of 21 bodies including the chassis, suspension and wheel uprights, as described in Appendix A and shown in Figure 3.10.

In the model, each front Macpherson strut suspension was comprised of four bodies for the upright, suspension arms and tie-rod. The suspension arms were connected to the chassis with revolute joints and to the upright with spherical joints. The spring-damper was modelled with a linear spring element. Similarly, each rear five-link suspension model was comprised of six bodies representing the links and wheel upright. The inner suspension bushings and outer roll-over strut joint were assumed to be rigid and modelled with revolute joints, with the other suspension bushings modelled with flex points with equal in-plane stiffnesses. Separate linear spring and damper elements were used to model the suspension springs and dampers. The vertical compliance of the tires were modelled using a flex point item, and the lateral cornering stiffnesses were modelled using a speed dependent linear damper element. Vertical gravitational loads were applied to the chassis and wheel uprights, with the gravitational loading of the links ignored, as the corresponding masses were small.

First, the eigenvalues of the full nominal multibody model constrained to planar motion were determined. The planar motion force and moment constraints were applied to the vehicle chassis, allowing the wheel degrees of freedom to be excited. Table 3.2 presents the eigenvalues for the planar motion with a forward speed of 25 m/s. Two rigid body modes can be seen with eigenvalues of zero. The third eigenvalue associated with lateral chassis motions with a natural frequency of 1.28 Hz can be seen. This mode is very similar to the mode observed with the yaw-plane model. A set of in phase and out of phase wheel hop modes are also present with natural frequencies between 6.93 Hz and 8.14 Hz. Higher frequency, highly damped modes associated with the rear suspension bushings were also present and have been omitted for clarity.

Next, the eigenvalues of the full nominal unconstrained multibody system with a forward speed of 25 m/s were determined. Table 3.3 presents the eigenvalues predicted by the detailed model. Again the high frequency highly damped modes associated with the suspension bushings have been excluded. The model predicts two rigid body modes associated with lateral motion of the vehicle. The third mode predicted has a real component similar to that predicted by the yaw-plane and constrained multibody models, however, the small imaginary component has disappeared. From this it can be inferred that the response of the vehicle is exhibiting exponential decay, and that the

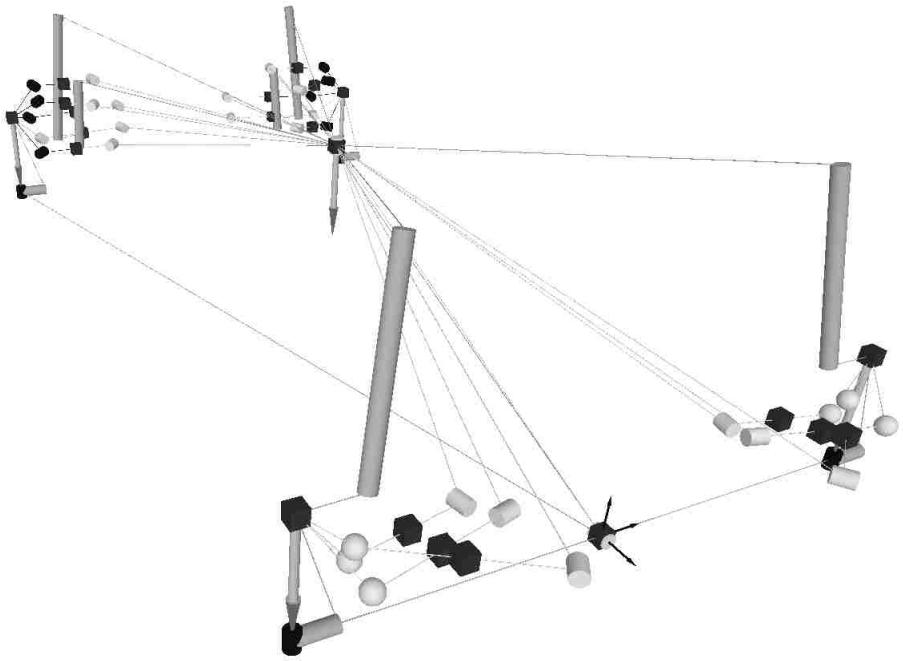

Figure 3.10: *Multibody EoM model: nominal configuration*. This figure presents the EoM model of the BMW 330i in the nominal configuration. As presented the ground element (with axes) and the front of the vehicle can be seen in the bottom right corner, with the front left suspension and connections to the vehicle cabin (thin lines) to the extreme right. The model is comprised of a collection of bodies (black cubes), linear springs (gray cylinders), revolute joints (light gray cylinders), rigid points (light gray spheres), flex points (black cylinders) acted on by loads (light gray arrows). The actuators and sensors on the system have been removed for clarity. Connections between the various elements are shown by the connecting lines.

transition to oscillatory response occurs at a higher speed than previously predicted. This may be attributed to the additional roll degree of freedom of the chassis, and the effect of the vehicle suspension. An additional stable exponentially decaying mode associated with coupled lateral chassis motion and roll about the vehicle roll axis is present. Stable chassis bounce, pitch and roll modes are also predicted, and fall within the range of expected frequencies. The in-phase and out-of-phase wheel hop modes are also present, and shown to be similar to those of the constrained multibody model. In general, excluding the slightly positive rigid body mode attributed to computer rounding error, all of the predicted eigenvalues are stable. These results are similar to those predicted by the multibody Bombardier Iltis model presented by Minaker and Rieveley [57], that have been shown to correlate with benchmark data provided in [47].

Table 3.2: *Multibody BMW 330i eigenvalues at 25 m/s: nominal configuration, planar motion constraint.*

Mode	Re $\left[\frac{1}{s}\right]$	Im $\left[\frac{rad}{s}\right]$	Frequency [Hz]	Damping [%]
1 vehicle lateral	0	0	·	·
2 vehicle lateral	0.00243	0	·	·
3 vehicle lateral	-7.96	$\pm$ 0.973	1.28	99.3
4 front wheel hop: in phase	-13.2	$\pm$ 41.5	6.93	30.2
5 front wheel hop: out of phase	-13.2	$\pm$ 41.5	6.93	30.2
6 rear wheel hop: in phase	-12.4	$\pm$ 49.6	8.14	24.2
7 rearwheel hop: out of phase	-12.4	$\pm$ 49.6	8.14	24.2

Table 3.3: *Multibody BMW 330i eigenvalues at 25 m/s: nominal configuration.*

Mode	Re $\left[\frac{1}{s}\right]$	Im $\left[\frac{rad}{s}\right]$	Frequency [Hz]	Damping [%]
1 vehicle lateral	0	0	·	·
2 vehicle lateral	0.0801	0	·	·
3 vehicle lateral	-7.95	0	·	·
4 vehicle lateral + cabin roll	-11.9	0	·	·
5 cabin bounce	-2.79	$\pm$ 2.92	0.643	69.1
6 cabin roll	-5.26	$\pm$ 10.5	1.87	44.8
7 cabin pitch	-1.06	$\pm$ 16.1	2.56	6.6
8 front wheel hop: in phase	-10.8	$\pm$44.2	7.24	23.8
9 front wheel hop: out of phase	-11	$\pm$ 43.1	7.07	24.7
10 rear wheel hop: in phase	-11.7	$\pm$48	7.87	23.7
11 rear wheel hop: out of phase	-12.5	$\pm$47.5	7.82	25.5

3.4 Nonlinear Model

To extend upon the results obtained using the detailed linearized models, a high fidelity virtual prototype was developed using CarSim® [3]. CarSim® is a modelling package developed exclusively for generating systems of equations for vehicle dynamics, offering accuracy and ease-of-use at the expense of flexibility when compared to its generalized counterparts.

Within this code, systems of ordinary differential equations are generated using a set of predefined solvers depending on the vehicle topology. The predefined solvers were developed and are continuously refined using VehicleSim®, replacing initial efforts with AutoSim® [80]. The model developed within this study made use of the 'independent-independent' (i-i) model, comprised of 102 ODEs expressing the dynamic and kinematic vehicle behaviour. This model was composed of 32 bodies, 16 multibody DOF, 42 multibody coordinates, 16 multibody speeds acted on by 61 active forces and 47 active moments. The sprung mass of the vehicle has 6 DOF including longitudinal, lateral and vertical translations with roll, pitch and yaw rotations. Two DOF representing the vertical and rotational motions of each wheel are also included. The effects of suspension compliance and kinematics are also considered. Suspension kinematics were determined using look-up tables for quantities including camber, caster and toe change, defined using the kinematics and compliance test data presented in Appendix A. A nonlinear look-up table based tire model defined with the Salaani tire data was used with different tires on the front and rear axles as outlined within the vehicle definitions.

3.4.1 Model Verification

To validate the developed CarSim® model, a set of test simulations emulating those presented by Heydinger were conducted [33]. The validation tests conducted included quasi-steady state ramp steer and step steer, as well as, transient pulse steer and double lane change lateral dynamics simulations. Longitudinal dynamics simulations evaluating the straight-line braking and acceleration of the nominal vehicle were also conducted.

The results pertaining to the handling response of the nominal vehicle are presented in Figure 3.11 and Appendix B. From these tests it was shown that the model accurately replicated the response of the experimental vehicle in all of the test conditions. Figure 3.11 illustrates the response of the nominal vehicle configuration throughout a double lane change at 50 km/h. In this test the experimental steer input given in [33] was used to excite the vehicle model. It can be seen that the vehicle reaches a maximum of 0.75 g's of lateral acceleration representing an emergency lane change condition.

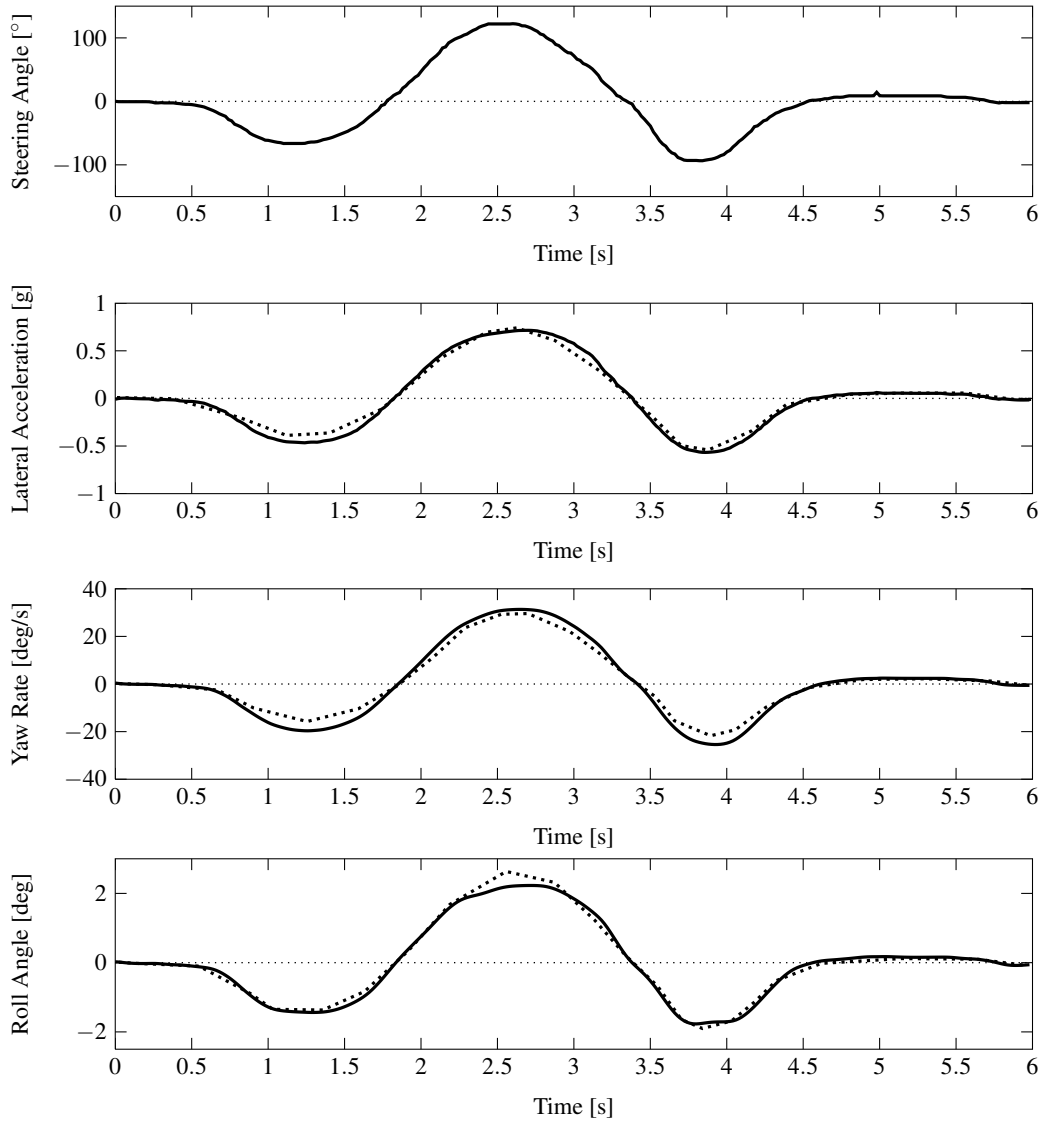

Figure 3.11: *CarSim® model double lane change validation at 50 km/h: nominal configuration*. The figure presents the double lane change response for the nominal 2006 BMW 330i with an initial forward speed of 50 km/h. The experimental steering wheel input given in [33] was used as the input for the simulation. This simulated result (solid) correlates well with those presented in the literature (dotted).

3.4.2 Dynamic Response

Stability analysis of nonlinear models is more complicated than that of linearized models, as various equilibrium points, stochastic elements or other significant nonlinearities may be present [82]. The use of time domain stability analysis techniques becomes more valuable. Phase portrait analysis is a useful tool illustrating the dynamics of a nonlinear system by comparing various system states through time. In this method, the free state response of a perturbed system can be used to indicate stable equilibrium points, marginally stable or divergent instabilities appearing as stable nodes, saddle points and unstable nodes. Traces within this space can also be used to illustrate the forced response of the system through a manoeuvre. These traces may be used to indicate the proximity of the vehicle response to stable or unstable points and regions in the phase plane throughout a manoeuvre as proposed in [46].

The free and forced $\dot{\beta} - \beta$ phase portraits for the developed nominal BMW 330i model at 100 km/h are given in Figure 3.12. The phase plane trajectories presented indicate the stable free response of the model around the zero-zero equilibrium point at the given speed. It can also be seen that as the side slip angle increases the model response exhibits a more unstable behaviour as the response becomes less predictable. This can lead to divergent responses outside of a given operational region. Also presented are the forced responses of the nominal, forward CG and rearward CG configurations through a double lane change manoeuvre with identical steer inputs. From the phase plane traces, it can be seen that the nominal and forward centre of gravity configurations remain well within the stable region, while the rearward centre of gravity case remains stable but approaches the less stable region of the phase portrait. A visualization of the responses of the vehicles tested is also shown in Figure 3.13. It can be seen that the nominal (black) vehicle successfully completes the manoeuvre with the given steer input, while the forward centre of gravity configuration hits the first lateral cone and the rearward centre of gravity hits the final cone. It can be seen that the oversteering configuration is more responsive to driver input and operates at a much higher side slip angle than the other two configurations. From these results it can be seen that longitudinal shifts in the vehicle centre of gravity can significantly effect vehicle handling and response to driver steering wheel input.

3.5 Linear and Nonlinear Model Comparison

To evaluate the efficacy of the developed linearized vehicle models in predicting the time domain response of the actual vehicle, the predicted response of the linear models were compared to that of the nonlinear CarSim® model. Figure 3.14 compares the double lane change response of the developed linear and nonlinear models of the nominal vehicle configuration. In the test condition,

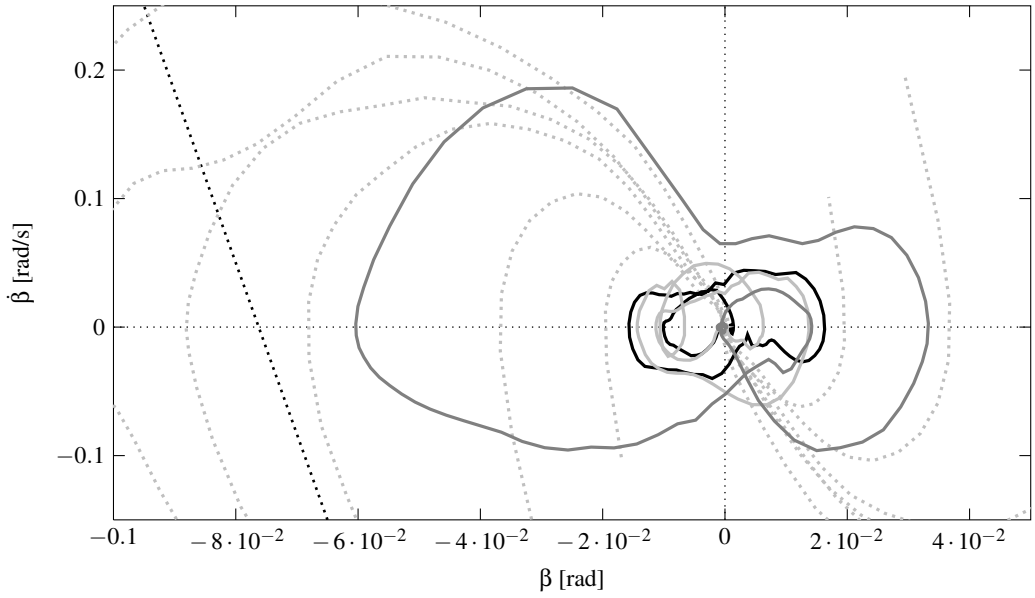

Figure 3.12: *Free and forced* $\dot{\beta}$-β *phase plane portrait at 100 km/h: nominal vehicle*. In the figure the dotted gray lines indicate the free phase plane response to initial perturbation, a stable region to the right of the black dotted line can be seen. When initial conditions for side slip angle and rate are outside the stable region the $\dot{\beta}$-β response of the vehicle becomes less predictable. The double lane change response of the nominal vehicle (black), the forward (light gray) and rearward (dark gray) centre of gravity conditions are shown.

the forward speed was held constant at 72 km/h, and a set of steering wheel inputs producing 0.3, 0.6 and 0.8 g's of lateral acceleration were given as inputs. It can be seen that the linear model replicates the nonlinear response of the vehicle quite well. At both low and high steer inputs the linear and nonlinear predictions for lateral side slip velocity correlate well, with reduced fidelity with mid-range steer inputs. The yaw rate response of the nonlinear model is predicted well in the case of low to mid-range steer inputs, with reduced correlation for the high steer input case. Similar results were obtained for the forward and rearward centre of gravity cases. However, it should be noted that in general, the yaw-plane model is expected to accurately predict vehicle response up to 0.4 g's of lateral acceleration [89]. The extended range of valid prediction of the current model can be attributed to the high cornering stiffnesses of the tires given by the Salaani tire model.

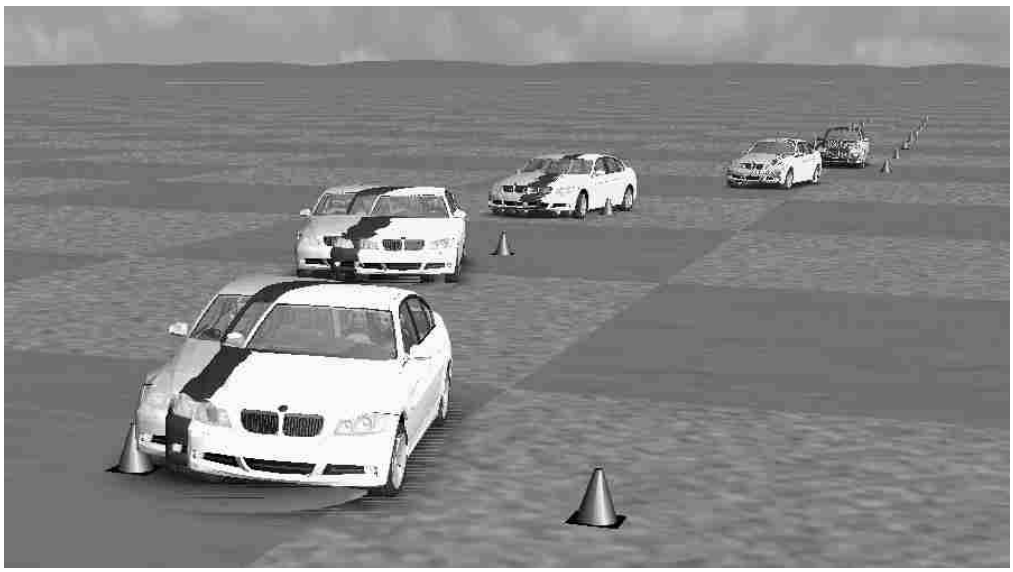

Figure 3.13: *CarSim® response for a double lane change at 100 km/h.* Visualization of the response of the three vehicle configurations during double-lane change manoeuvre at 100 km/h, given the identical steering wheel input. The white, black and gray vehicles represent the forward, nominal and rearward centre of gravity vehicle configurations respectively. The forward centre of gravity configuration hits the first lateral cone. The rearward centre of gravity hits the final cone. It can be seen that longitudinal shifts in the vehicle centre of gravity can effect vehicle handling and response to driver steering wheel input.

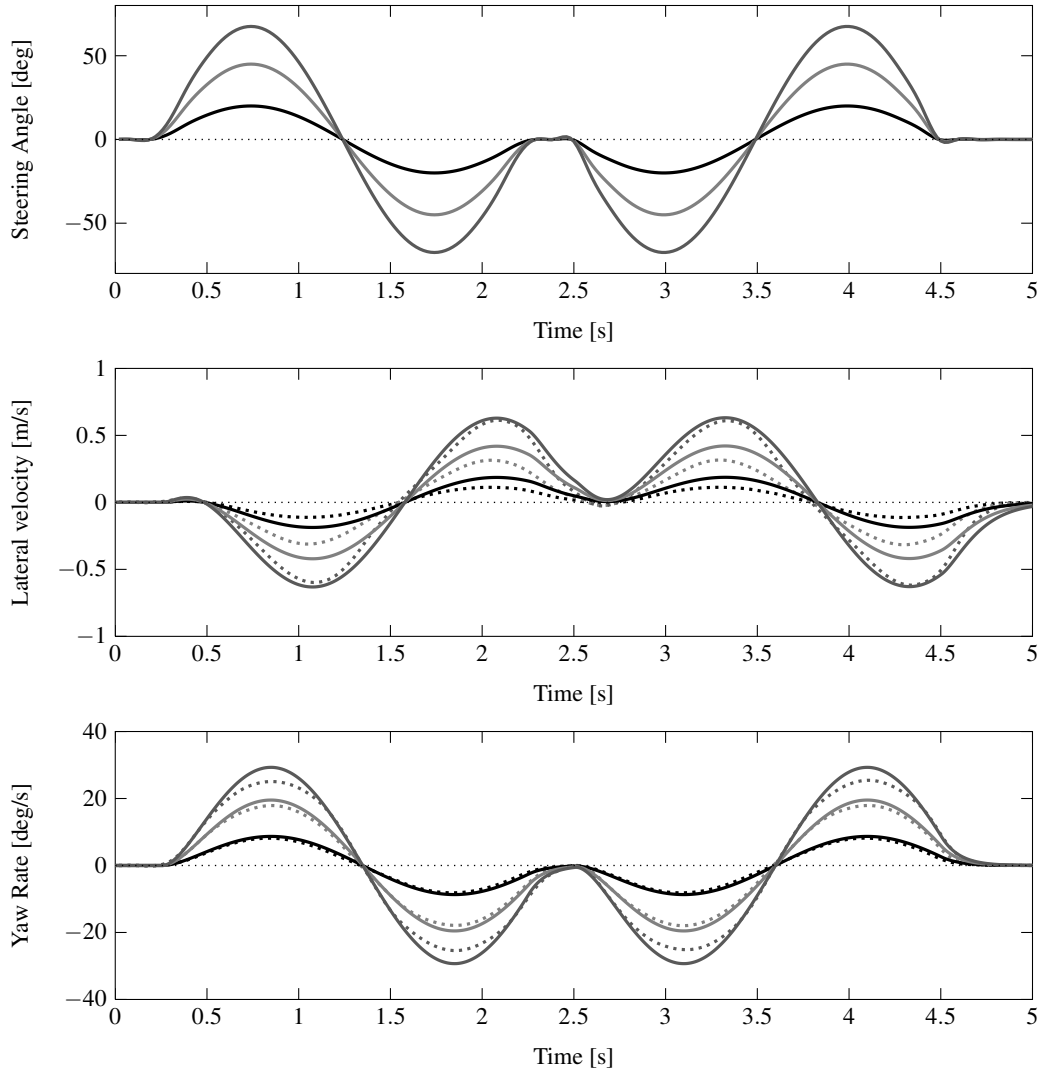

Figure 3.14: *Linear and nonlinear model comparison for double lane change: nominal configuration.* The figure presents the vehicle response predicted by the CarSim® virtual prototype (dotted) and two degree of freedom linear yaw-plane EoM (solid) BMW 330i models with forward speed of 72 km/h and various steer input.

3.6 Summary

This chapter has detailed the development and validation of a set of mathematical vehicle models of a 2006 BMW 330i. The vehicle models were developed for a nominal, forward centre of gravity and rearward centre of gravity configurations using a novel method for automatic generation of the equations of motion for systems with nonholonomic constraints. The eigen-response of yaw-plane models of each configuration were shown to be stable over the expected range of operational speeds. A full multibody model was then developed, introducing additional stable modes associated with bounce, pitch and roll motions of the chassis, as well as wheel hop motions.

A nonlinear CarSim® vehicle model was developed and time-domain simulations were shown to correlate well with those found in literature. A phase plane analysis was used to show that the nominal configuration of the vehicle exhibits stable response. The forced response of the nonlinear vehicle models through a double lane change were presented showing that the vehicles operate within the stable region through a double lane change at 100 km/h.

Finally, the linear models have also been shown to accurately predict vehicle response in a number of cases with increasing lateral acceleration. However, this result is not attributed to the method used for generating the equations of motion and are more likely caused by the cornering stiffnesses of the tires used within the vehicle model.

Chapter 4

Driver Modelling

The dynamic response of a conventional road vehicle relies heavily on the interactions between the vehicle and the human operator. Due to this reliance, the driver model is critical to obtaining robust closed-loop model predictions of driver-vehicle behaviour. This chapter details the relevant methods and development of a hybrid driver model for vehicle simulations. The application of this model to the current research, as well as vehicle design simulations [74] and a novel project-based course element developed for the 06-94-463 Vehicle Dynamics course at the University of Windsor [72] are presented.

4.1 Human Driver

Human control tends to exhibit both deterministic and non-deterministic qualities, relying on human learning, involving biological processes including perception, data processing and neuro-muscular interactions. The study of each is a research topic on its own. However, a detailed, tuneable and modular deterministic driver model was desired to realistically evaluate the vehicle models and control methods developed within the scope of this research. This was accomplished through the synthesis and extension of various algorithms that have shown to accurately emulate the vehicle control processes of human drivers. Within this synthesis, the tasks of the driver were broken into separate tasks involving navigation, guidance and stabilization.

4.1.1 Navigation and Guidance

The processes of navigation and guidance occur on the macro and micro scale involving tasks such as route planning, path planning, traffic monitoring and obstacle avoidance. Contributions within this scale have focused on the development of a path planning algorithm. Path planning requires detailed information regarding the road geometry, which must be conveyed to the driver in a mean-

ingful manner.

Road Geometry

The definition of road geometry is important in the determination of the desired future path of a vehicle. The definition should include information regarding the road geometry, surface quality and obstacles. Conventionally, the road centreline geometry is reproduced using a set of data points, or parameterized straight line, spiral and circular arc segments, with the number and resolution of road segments adjusted as required [42]. Traditional methods can lead to definition problems when considering the path planning problem, with overlapping and non-uniform elements, as illustrated in Figure 4.1a. In certain cases, more information regarding road width, height and other characteristics are required, leading the integration with simulation models to be more cumbersome [10]. Regardless, the path obtained from the defined road geometry should adhere to the following:

- Continuity of path, as the path must be complete and without gaps, as no vehicle can move instantly from one discrete point to another
- Continuity of curvature, as an instantaneous change in road curvature will cause instantaneous change in the expected rotational velocity of the vehicle
- Differentiability of course, as sharp bends lead to infinite curvature that can not be traversed by a real vehicle

In general, information regarding the desired global directions, curve radius, yaw rates, and appropriate forward speeds to traverse the road should be obtainable from the road definition. To this end, a track definition method utilizing the meshing of road geometry with mapped track elements was developed, similar to those used in finite element analysis [9].

Mapped Road and Path Geometry

A method for the coupled definition of road and path geometry was developed during the course of this research. The developed method allows the definition of complex road geometry to be generated from either tabular data, or aerial photographs, as detailed in [74]. Further, this method defines the desired path within a given road geometry with a diminutive set of way-point data. The definitions created have been shown to be beneficial in the area of optimal path planning.

The developed algorithm requires the definition of vectors containing the left and right road edges, that are used to generate meshed elements, as shown in Figure 4.1b. Under the developed method, these vectors may contain irregular spacing, as edge orthogonality of the elements is not required; however, elements should be properly proportioned and without extreme angularities to

ensure that a proper mapping of the meshed elements can be obtained. Within the defined methodology, the data points are meshed moving in a counter-clockwise direction around the boundaries of the elements, and mappings are created, as shown in Figure 4.1c. The figure illustrates the use of a four point mapping to a 2x2 square mapped space, with Lagrange interpolation between node points [9]. The global location of each mapped coordinate can be expressed using a linear mapping as

$$\begin{Bmatrix} x(s,t) \\ y(s,t) \end{Bmatrix} = \begin{bmatrix} x_1 & x_2 & x_3 & x_4 \\ y_1 & y_2 & y_3 & y_4 \end{bmatrix} \mathbf{N} \tag{4.1.1}$$

where x_i and y_i are the nodal coordinates in the global frame and $\mathbf{N}$ represents the interpolation functions given as

$$\mathbf{N} = \begin{pmatrix} \frac{1}{4}(1-s)(1-t) \\ \frac{1}{4}(s+1)(1-t) \\ \frac{1}{4}(s+1)(t+1) \\ \frac{1}{4}(1-s)(t+1) \end{pmatrix} \tag{4.1.2}$$

where s and t are the mapped element coordinates. Further, the Jacobian on each mapped element can be evaluated to assure valid mappings, such that

$$\det\left(\begin{bmatrix} \frac{\partial x}{\partial s} & \frac{\partial x}{\partial t} \\ \frac{\partial y}{\partial s} & \frac{\partial y}{\partial t} \end{bmatrix}\right) > 0 \text{ for } -1 \leq s,t \leq 1 \tag{4.1.3}$$

Once the valid elements are generated, information regarding the desired path can then be added. This is realized as way-point data, detailing the lateral offset position at the leading edge of each track element. At this point, it can be shown that the path defined by this way-point data although sufficient, may not exhibit continuity of curvature. To correct this, additional point data between the defined way-points is required. To maintain the minimal nature of the definition, the use of interpolation techniques can be applied, similar to those proposed by Crittenden [18]. With the addition of heading angles at the leading edges of the elements, Hermite interpolation can be used to generate a unique third degree polynomial spline in the local frame of each mapped element, using only the lateral offset and heading angle information for consecutive elements. Using this interpolation any number of sub-way-points defining the path across an element can be generated, to meet 1 dimensional (1D) path and curvature continuity conditions.

The developed mapped-way-point road and path definition is well suited for the optimal path planning problem, where a search space must be defined. The minimal nature of this definition allows potentially large search spaces to be defined using minimal data, as is explored in the following section.

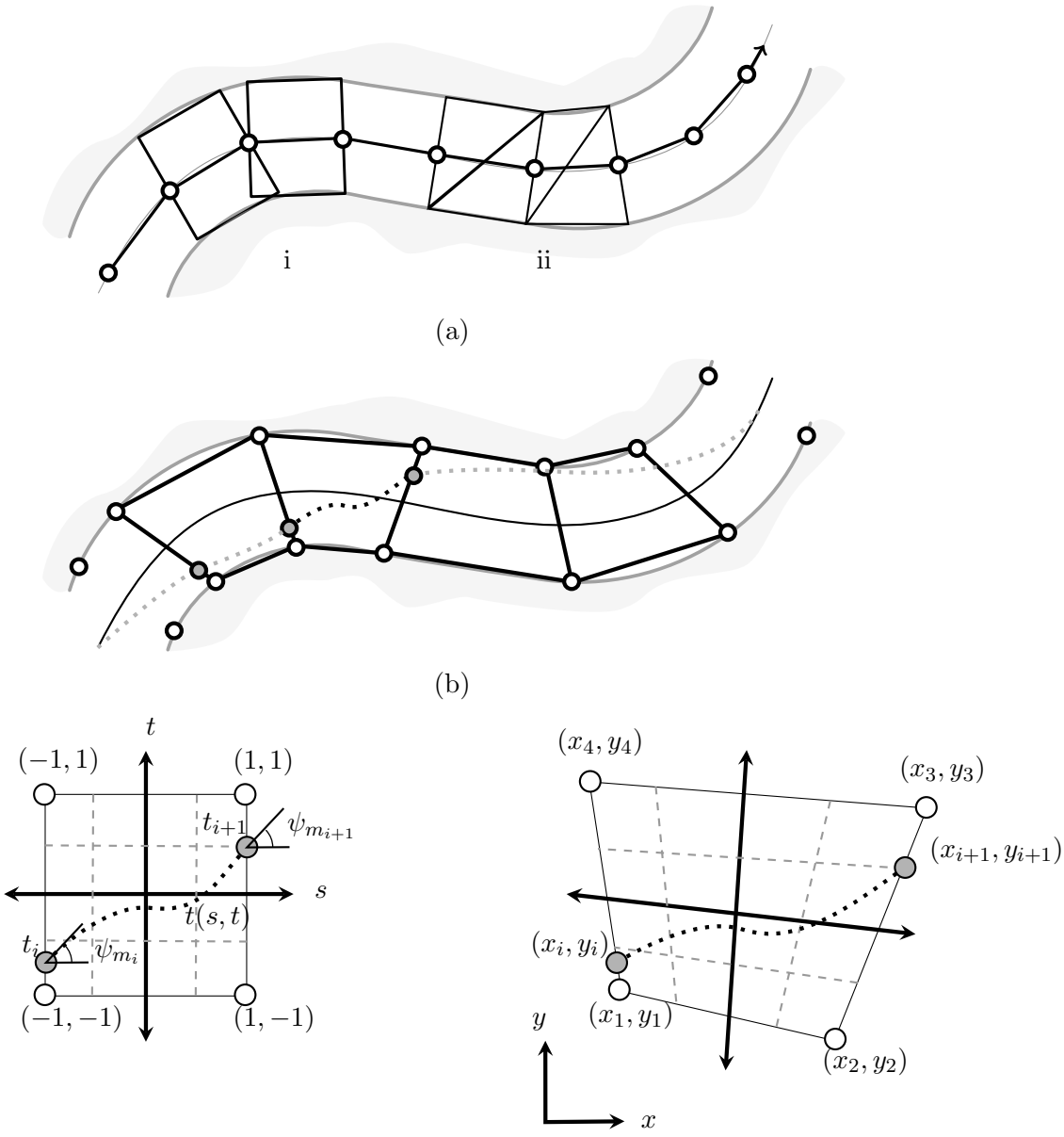

Figure 4.1: *Mapped road geometry*. The figure shows the detailed method of producing mapped road geometry. (a) shows (i) the conventional method of road geometry definition using centreline and road width, and (ii) a triangular mesh of road geometry. (b) shows the road geometry definition using meshed elements determined from x-y pairs (white dots). An example mapping is then generated for each meshed element using a four node method. Additional way-point information regarding the lateral deviation and heading angle are illustrated in (c) (gray dots), along with sub-way-point functions (black dotted).

Optimal Path Planning

The driver model must take the road geometry and environmental information and choose an appropriate path to traverse. The simplest method, is to assume the road path or centreline is the intended path of the driver; however, this is rarely the case, as the vehicle may be free to traverse laterally within or across lanes. This is the case in a racing environment, where the driver will make full use of the road width to obtain the minimal lap time.

The use of genetic based search algorithms to determine optimal paths within operating environments have been independently proposed by Lu and Wang [52, 85]. Within a genetic algorithm, a genome defining a set of solution parameters is developed. Further, an initial set of 'parent' solutions are generated, and subsequently used to generate new 'child' solutions that contain genetic information from each parent. These solutions are evaluated using a penalty function, leading the search to evolve to an optimum solution within the defined search space. It should be noted that the method is non-deterministic and that convergence to the global optimum is not guaranteed within any number of generations, and is largely dependent on the size of the search space.

To minimize the search space of the optimization problem, the previously described mapped road and path definition can be utilized. Within this definition the way-point data describing the lateral offset and heading angle at the start of each road element can be used as solution parameters. These solution parameters can then be compiled, yielding a fixed length genome given as

$$\mathbf{G} = \begin{bmatrix} t_1, & t_2, & t_3, & ..., & t_n \\ \psi_{m_1}, & \psi_{m_2}, & \psi_{m_3}, & ..., & \psi_{m_n} \end{bmatrix} \tag{4.1.4}$$

where $\mathbf{G}$ is the fixed length genome, t_i and ψ_{m_i} with $i = 1, 2, ..., n$ represent the mapped lateral offset and heading angle of the n way-points given by the road definition.

As an example, a genetic algorithm based search was used to determine an optimal path for the geometry given in Figure 4.3, where the dark gray boxes represent penalty regions to be avoided. A search space involving five equally spaced discrete values of lateral offset in the range of $\pm 90\%$ of the road width from centreline, and five equally spaced heading angles in the range of $\pm 22^\circ$ were used. The proposed genetic algorithm was seeded with an initial population comprised of a set of random variations about the track centre line. Child genomes were generated from two mating parent solutions from the previous generation, using a single point crossover algorithm that divided and joined the parent genomes at a randomly determined point. The mating pairs were selected depending on solution fitness, with the top 50% of solutions from each generation given the ability to mate. Elitism was used ensure that the best solution of each generation was directly carried to the child populations. These child solutions were also allowed to mutate randomly across the genome within the given search space.

The fitness of each solution was inferred from the lap time of the proposed path, obtained using a quasi-steady state (QSS) lap time simulation algorithm that ignored the influence of lateral load transfer. This algorithm assumed that changes in vehicle state occur slowly and continuously. The solution with the lowest and highest lap times were considered the most and least fit solutions respectively. Under the QSS algorithm the maximum speed at each corner apex was determined from the path curvature assuming

$$u_i = \sqrt{\mu m g \rho} \tag{4.1.5}$$

where μ is the coefficient of friction, m is the vehicle mass, g is the gravitational constant and ρ is the cornering radius. The QSS algorithm then calculated the maximum allowable speed profile under throttle and braking away from and leading to each corner apex using a friction ellipse analysis. A cross-over acceleration-braking point was determined from the obtained acceleration and braking velocity profiles, as shown in Figure 4.2. The speed profile for the given genetic solution was then generated combining the speed profiles between each cross-over point. The lap time was then determined by integrating the speed profile giving the solution fitness for the genetic search algorithm. More information regarding lap time estimation can be found in [74].

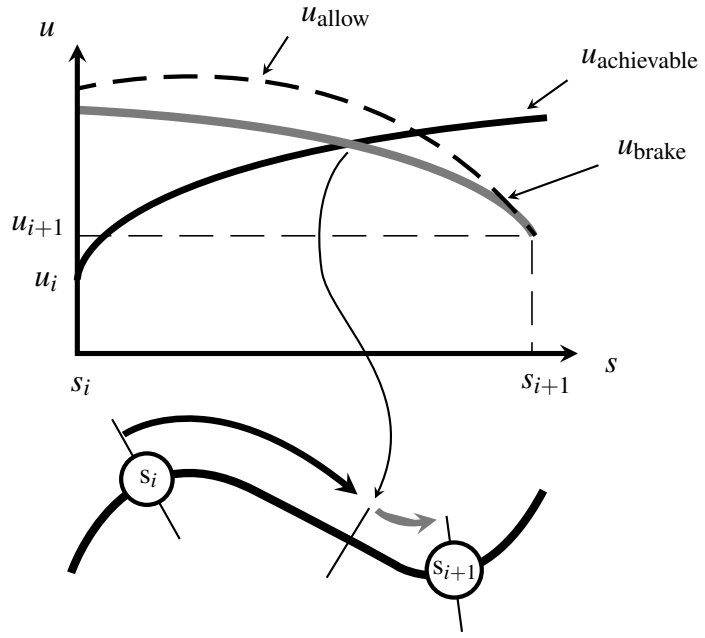

Figure 4.2: *Quasi-steady state velocity profile determination.* This figure illustrates the method for determining the speed profile for the given genetic solution. The speed profile was comprised of acceleration and braking events between each acceleration-braking cross-over point.

The path determined using the presented method successfully avoids the given obstacles and road geometry, as shown in Figure 4.3a with the fitness of each solution shown in Figure 4.3b. It can be seen that the minimum traversing time of the most fit solution is reduced significantly over the first 26 generations, where the initial penalty boundary crossings are present in most solutions. After this point, traverse time is reduced through reductions in path curvature allowing higher longitudinal speeds to be maintained. While most solutions are closely packed around the minimum time, solution groups containing one, two and three (i,ii,iii) penalties can be attributed to mutation in the double-lane change region imposed by the penalty regions.

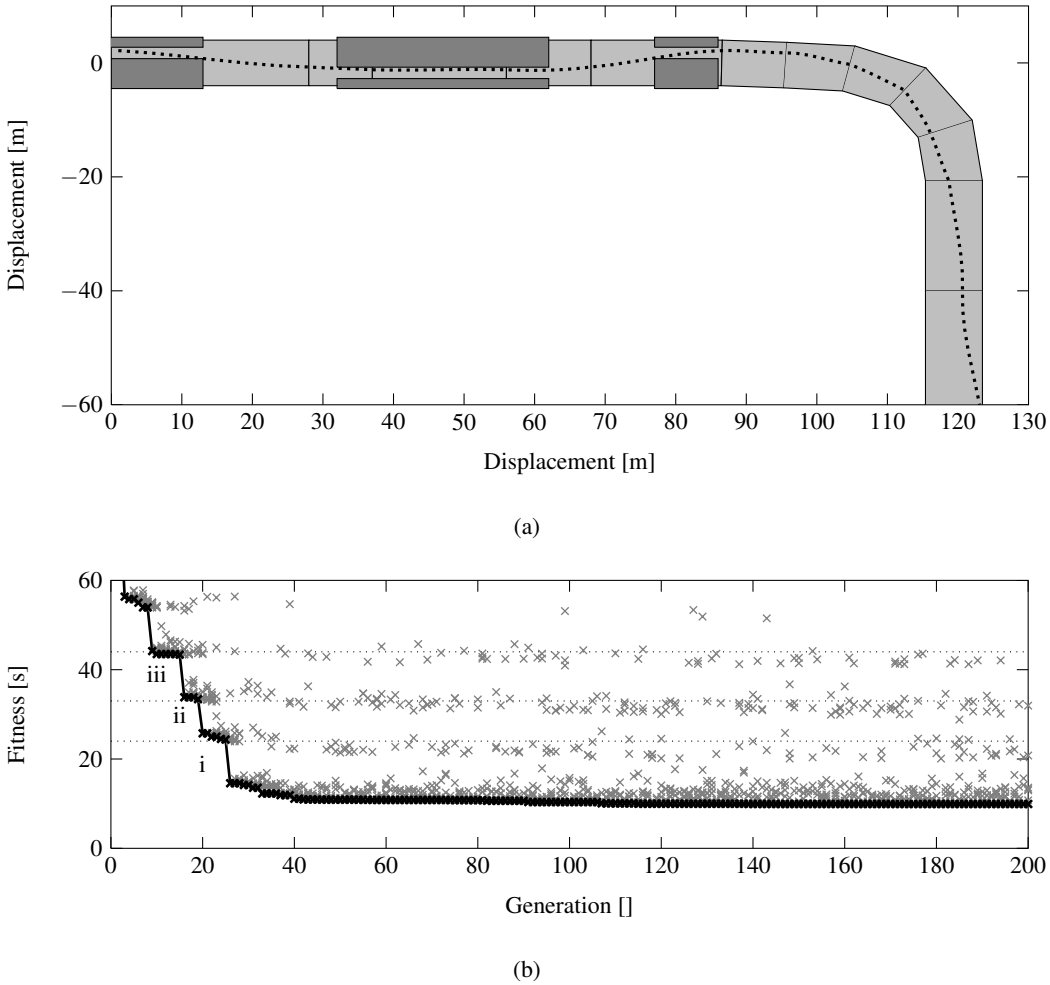

Figure 4.3: *Genetically determined path.* This figure shows the path determined using the genetic optimal path algorithm using minimum time criteria determined with a quasi-static lap time estimation. Initial population genomes were seeded randomly. New populations were defined using crossover mating of the top 50% fittest parent solutions with a mutation rate of 50%, elitism was also enforced. (a) shows the minimum time path, with penalty regions. (b) shows the genetic fitness of each solution (gray) and the maximum fitness envelope (black) with respect to generation. Marks i,ii and iii indicate solutions that trigger one, two and three penalty regions. It can be seen that the majority of solutions clear the penalty regions by generation 26, with minor fitness improvements in traversing time due to turning radius improvements in following generations.

4.1.2 Stabilization

The stabilization regime involves driver tasks that immediately effect the response of the vehicle, including steering wheel angle, throttle, and brake inputs to the vehicle system. The control algorithms chosen to emulate the driver must be robust to changes in the vehicle configuration and environment. In order to accomplish this, the driver control tasks can be separated into separate lateral and longitudinal controls, determining the required steering wheel angle and powertrain control signals respectively.

Lateral Control

When a human interacts with a vehicle, it is widely believed that appropriate control actions are determined using a predictive internal representation or input-output mapping of the dynamic system [69, 54, 84]. It is believed that this internal representation is learned and is refined with experience, improving the pursuit and compensatory actions of the driver. A method assuming the driver behaves as an optimal predictive control was proposed by MacAdam [54]. In this method an internal model is used to predict the future positions of the vehicle, and an optimal cost function is used to determine the desired control signals, as illustrated in Figure 4.4. The steering control is found by minimizing a cost function of the form

$$j = \frac{1}{t_\mathrm{f}} \int_0^{t_\mathrm{f}} \{(y_\mathrm{d}(t) - y(t))\}^2 w(t) dt \tag{4.1.6}$$

where j is the cost, t and t_f are the current and preview times respectively. The predicted and desired lateral displacements in the local frame are represented by y and y_d, and $w(t)$ is a weighting function. When the system input is constant over the preview period, the lateral offset can be expressed as

$$\boldsymbol{y}(t) = \mathcal{C} e^{\mathcal{A}t} \boldsymbol{q}_\mathrm{o} + \mathcal{C} \left[\int_0^t e^{\mathcal{A}(t-\tau)} d\tau \right] \mathcal{B} \boldsymbol{u} \tag{4.1.7}$$

where $\mathcal{A}$, $\mathcal{B}$, $\mathcal{C}$ and $\mathcal{D}$ represent the dynamics of the internal model when $\boldsymbol{u}$ is assumed constant over the preview horizon. Substituting this relationship into the cost function and rearranging into a discrete form, the steering angle control law can be expressed as

$$\delta_\mathrm{f} = \frac{\sum_{i=1}^{n} \{\boldsymbol{y}_{d_i} - \Phi_i \boldsymbol{q}_\mathrm{o} - \Psi_{2i} \boldsymbol{u}_{\mathrm{o}_2}\} \Psi_{1i} w_i}{\sum_{i=1}^{n} \Psi_{1i}^2} \tag{4.1.8}$$

where δ_f is the front steering angle, Φ and Ψ are the discrete state transition matrices for the ODE system relating the initial state $\boldsymbol{q}_o$ and the remaining system inputs $\boldsymbol{u}_{\mathrm{o}_2}$. The state transition terms

$\Phi \boldsymbol{q}_{\mathrm{o}}$ and $\Psi_{2i} \boldsymbol{u}_{\mathrm{o}_2}$ can be evaluated numerically, assuming that the forward velocity and inputs to the system remain constant over the preview period.

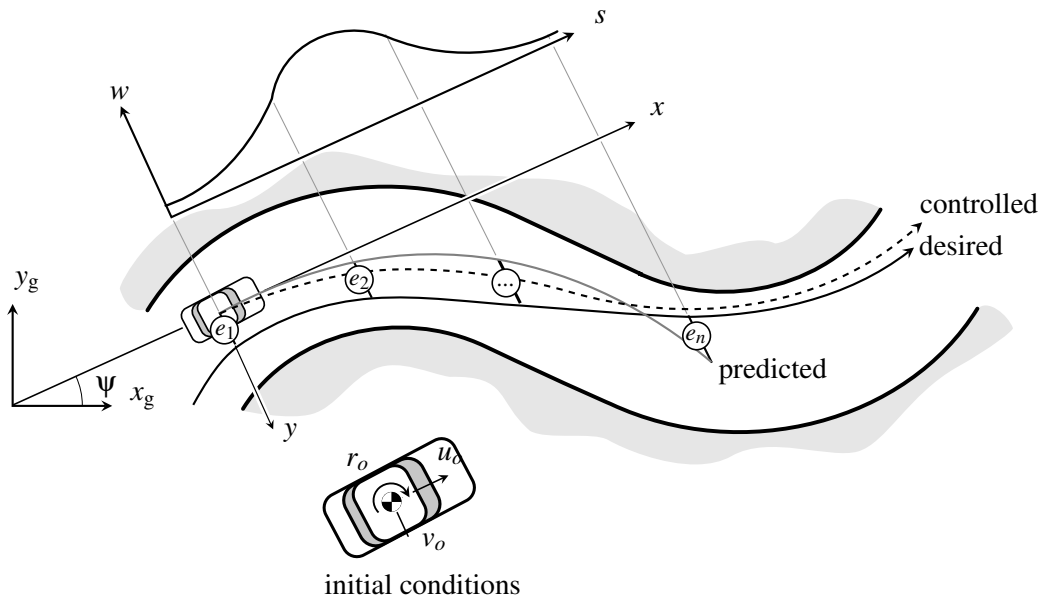

Figure 4.4: *Model predictive path follower.* The lateral path following driver model determines steering wheel angle commands using the weighted predicted lateral errors e_i where $i = 1..n$ to the desired path in the local frame over the preview period. Future predicted positions (gray line) are determined numerically using a yaw-plane model given the initial longitudinal, lateral and yaw velocities are given as u_{o}, v_{o} and r_{o} respectively. Error weightings w are given as a function of longitudinal preview distance s. The dotted line indicates the resulting trajectory.

Figure 4.5 illustrates the steering angle input determined by the detailed optimal preview control when attempting to replicate the double-lane change test presented in Chapter 2. In this example, the developed two DOF linear BMW 330i model in the nominal condition was used as the internal driver model. Various preview horizon times were tested showing driver model dependence on preview time. In typical daily driving situations, a preview horizon of 1-1.5 seconds can be shown to provide a smooth pursuit dominated vehicle response during path following. However, these results indicate that using a shorter preview horizon better replicates the experimental emergency avoidance test condition. It can be seen that using a preview horizon of 0.55 seconds, the steer angle and path are replicated with sufficient accuracy. As the preview horizon time is increased, an effective damping is applied to the path following response of the driver vehicle system. If the preview time is reduced, the path following exhibits a more oscillatory behaviour as the control

efforts are more compensatory.

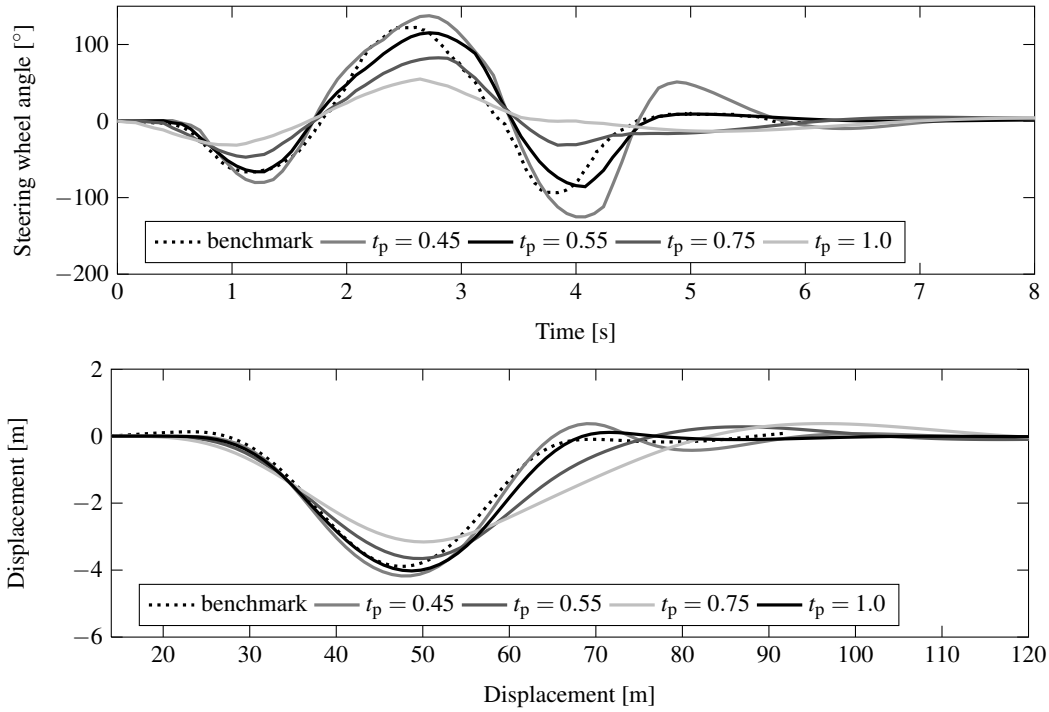

Figure 4.5: *Driver model steer control.* This figure shows the steering angle and global position for the simulations of an emergency double lane change manoeuvre. The dotted line represents the benchmark results obtained using the steering wheel angle given in the benchmark test from Chapter 2 [33]. The responses determined using the developed lateral steer control are given by the solid lines with 0.45, 0.55, 0.75 and 1.0 second preview horizons respectively. The given benchmark steering input is well replicated by the developed optimal preview control with a preview time of 0.55 seconds.

Longitudinal Control

The modelling of driver longitudinal control can be evaluated as a more discrete process with a set of distinct operational regimes, including straight line, braking, and cornering conditions, as illustrated in Figure 4.6. The human driver uses visual and vestibular feedback information to determine desired speed and acceleration profiles to successfully negotiate a given manoeuvre.

This perceived nature of longitudinal control can be emulated using finite state machine (FSM) representing the long term memory of the driver, as proposed in [42]. A FSM is an automata designed to provide particular output given a set of inputs, as it moves from one state to another. As

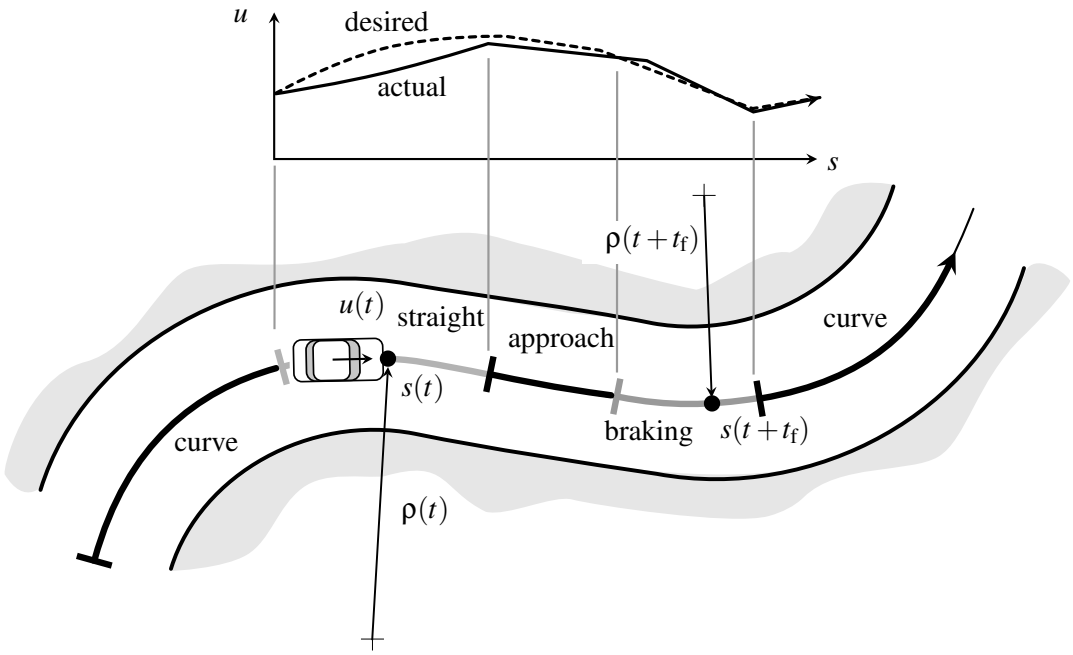

Figure 4.6: *Longitudinal driver operational states*. A discrete state longitudinal driver model used to determine operational conditions defined as straight, approaching curve, braking and curve. This can be accomplished with a limited set of vehicle state and path geometry data including; the current forward velocity $u(t)$ along with the current and future path radii, $\rho(t)$ and $\rho(t+t_f)$ respectively. Given this data, an algorithm can be used to determine reference vehicle states throughout a manoeuvre.

a state transfer occurs, output values are calculated using a set of input variables. A realization of a FSM for driver model application is shown in Figure 4.7. This finite state machine is comprised of six operational regimes, including initialization, straight line, approaching curve, braking, waiting and in curve. A set of entry and exit transition conditions are given, with reference velocity and acceleration values determined with calculation algorithms evaluated within each regime, as given in Appendix C.

Throttle and Brake Commands

The required throttle and brake pedal commands can now be determined by comparing vehicle states to the reference speed and acceleration values given by the FSM. These controls were implemented using transfer functions with switching terms assuring that only one control was active at a given

time. The throttle control can be expressed in transfer function form as

$$p_{\mathrm{t}}(s) = \begin{cases} \dfrac{k_{\mathrm{a}_1} s + k_{\mathrm{a}_0}}{k_{\mathrm{b}_2} s^2 + k_{\mathrm{b}_1} s + k_{\mathrm{b}_0}} & \text{if } \Delta u > \varepsilon u_{\mathrm{ref}} \text{ and } a_{\mathrm{ref}} > 0 \\ 0 & \text{if } \Delta u \leq 0 | p_{\mathrm{t}} \leq 0 \\ 1 & \text{if } p_{\mathrm{t}} > 1 \end{cases} \tag{4.1.9}$$

where p_{t} is the throttle position, Δu is the difference between the reference and forward speed of the vehicle, and a_{ref} is the driver model longitudinal reference acceleration. The brake master cylinder pressure expressed in transfer function form as

$$p_{\mathrm{b}}(s) = \begin{cases} \dfrac{k_{\mathrm{a}_0}}{k_{\mathrm{b}_1} s + k_{\mathrm{b}_0}} & \text{if } \Delta u < -\varepsilon u_{\mathrm{ref}} \text{ and } a_{\mathrm{ref}} < 0 \\ 0 & \text{if } a_{\mathrm{ref}} \geq 0 | p_{\mathrm{b}} \leq 0 \\ p_{\mathrm{b}_{\max}} & \text{if } p_{\mathrm{b}} > p_{\mathrm{b}_{\max}} \end{cases} \tag{4.1.10}$$

where p_{b} is the master brake cylinder pressure and $p_{\mathrm{b}_{\max}}$ is the maximum allowable master brake cylinder pressure. In both cases switching terms have been incorporated ensuring that in each case only the throttle or brake is used at a given instant.

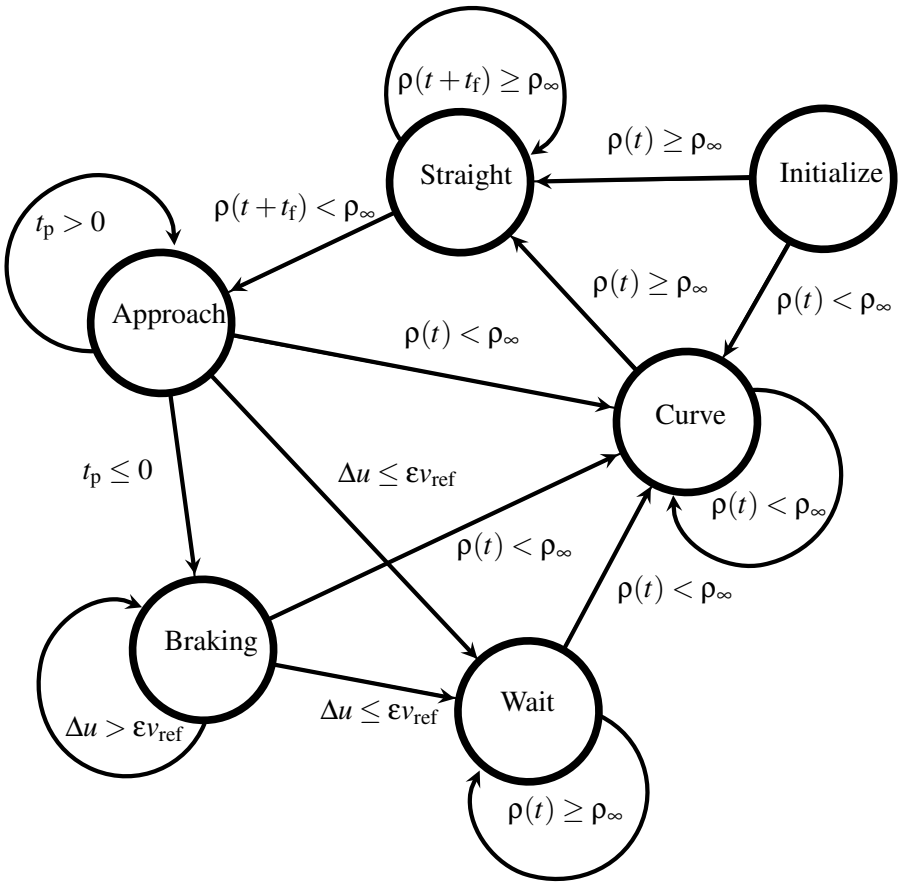

Figure 4.7: *Longitudinal driver finite state machine*. The desired vehicle reference velocity and acceleration are set using a finite state machine. The driver determines the operational condition based on preview road curvature. Only one operational condition may be active a one time, with a set of rules governing switches between states given by the arrows.

4.2 Applications

4.2.1 University of Windsor FormulaSAE Racing Lap Simulator

The developed path planning method and driver models have been implemented in a closed-loop racing lap simulation environment for the University of Windsor FormulaSAE team (UWFSAE). The simulations described were achieved through co-simulation of purpose developed MATLAB® models and CarSim®. The focus of the algorithm and model development was to produce a model that determined appropriate intended path and control signals of an actual human driver form basic vehicle and road data. The proposed driver model and developed simulation environment have been tuned and compared with experimental racing lap data acquired using the 2007 UWFSAE vehicle. This test data was acquired during racing laps, conducted with a UWFSAE driver with previous karting experience attempting to follow an intended racing line at the Point Pelee Karting track in Leamington, Ontario. The data was recorded using an onboard MSD engine controller and AiM Sports Pista data acquisition system (DAQ). The AiM Sports Pista DAQ was configured to record 8 analog channels including; 4 linear variable displacement transducers (LVDT) recording suspension deflections, 1 rotary potentiometer recording the steer angle, 2 brake pressure sensors monitoring front and rear brake line pressures, a non-driven wheel speed sensor, as well as the integrated $\pm$ 10 g lateral accelerometer and additional digital signals from the MSD MEFI-4b engine controller at 50 Hz. As no GPS data of the vehicle location was available, the racing line traversed by the human driver was reconstructed from the recorded data using the method detailed in [74]. In the simulated case, the path followed by the driver model was determined using the detailed genetic optimization path planning algorithm, and was shown to be similar to the one used in the experimental test.

A comparison showing the correlation between the simulated and experimental driver steer and vehicle speed lap data can be seen in Figure 4.8. The steering input determined by the driver model can be shown to predict the the trends of steering input of the human driver quite well; however, variations between the experimental and simulated data can be seen. These differences can be attributed to unmodelled non-deterministic correcting behaviour, and the differences in intended vehicle path. The unmodelled non-deterministic steering response can be seen at approximately 8.5 and 14 seconds, where the human driver is quickly modulating the steer angle of the vehicle in a compensatory corrective manner. The apparent time lag and amplitude errors in steer angle between 8-10, 16-18 and 22-24 seconds respectively can attributed to differences in the intended path of the vehicle. It was shown that the path determined by the developed path determination algorithm exhibited slightly different curvature and desired velocity profiles than that of the human driver. However, the path and control signals determined by the developed algorithms and models from road data have been shown to be representative of those of a human driver.

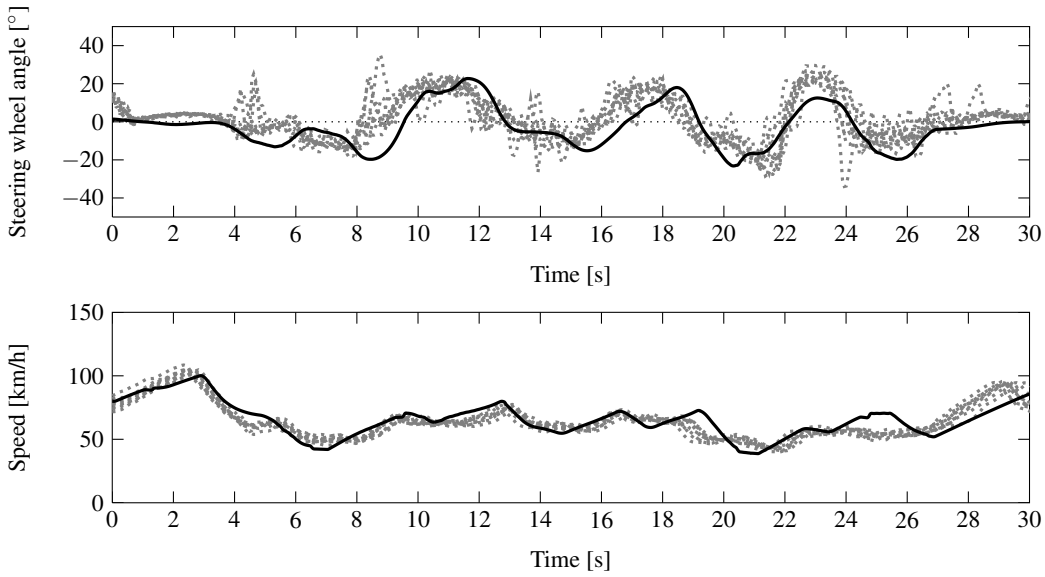

Figure 4.8: *UWFSAE driver model comparison*. This figure compares the response determined using the hybrid driver structure proposed (solid), with that of a student FSAE driver (dotted).

4.2.2 Formula463

The modelling techniques described within this chapter have been applied to a novel competitively based course project entitled Formula463, which has been integrated within the Vehicle Dynamics (06-94-463) course at the University of Windsor from 2007-2010. This project requires senior level engineering students to design and analyze virtual race cars, that are evaluated and raced within a closed-loop simulation environment. The focus of this project was to reinforce the direct link between theoretical material and application, while providing objective evaluation. Students were provided with in-house developed analysis tools, and were encouraged to develop their own simulation code. Vehicle evaluations of longitudinal, lateral, and ride dynamics were conducted using high-fidelity closed-loop co-simulation models. Students were given the opportunity to revise their designs after analyzing data from each test run. More information regarding the details of this project can be found in [72, 73].

The simulations were conducted using a nonlinear CarSim® vehicle model, with the specific design parameters defined by the student teams. To accommodate the expected variance in vehicle handling behaviour, the hybrid driver model structure detailed was utilized to control the vehicle during each test and race evaluation run. The performance of the developed driver model has been

tested through various situations including drag strip, skid pad and race circuits with multiple vehicle types and configurations. These simulations indicated that the driver model was capable of successfully navigating the prescribed courses with little user intervention and minimal input data. The path tracking capabilities of the model can be seen in Figure 4.9 along with the control inputs determined by the driver model. Low tracking error can be seen through both transient and steady-state cornering when tested on a prescribed path. Reduced tracking capability can be seen at approximately 80 and 110 seconds, corresponding to a hairpin corner and a high-speed low curvature corner. The reduced tracking fidelity in these regions can be attributed to a distinctly understeering vehicle configuration. Further, the throttle and brake commands are shown indicating the ability of the finite state machine driver model to determine appropriate throttle and brake commands. From the simulations conducted within this project, the hybrid driver model developed has been shown to be robust to variations in vehicle response associated with vehicle design parameters.

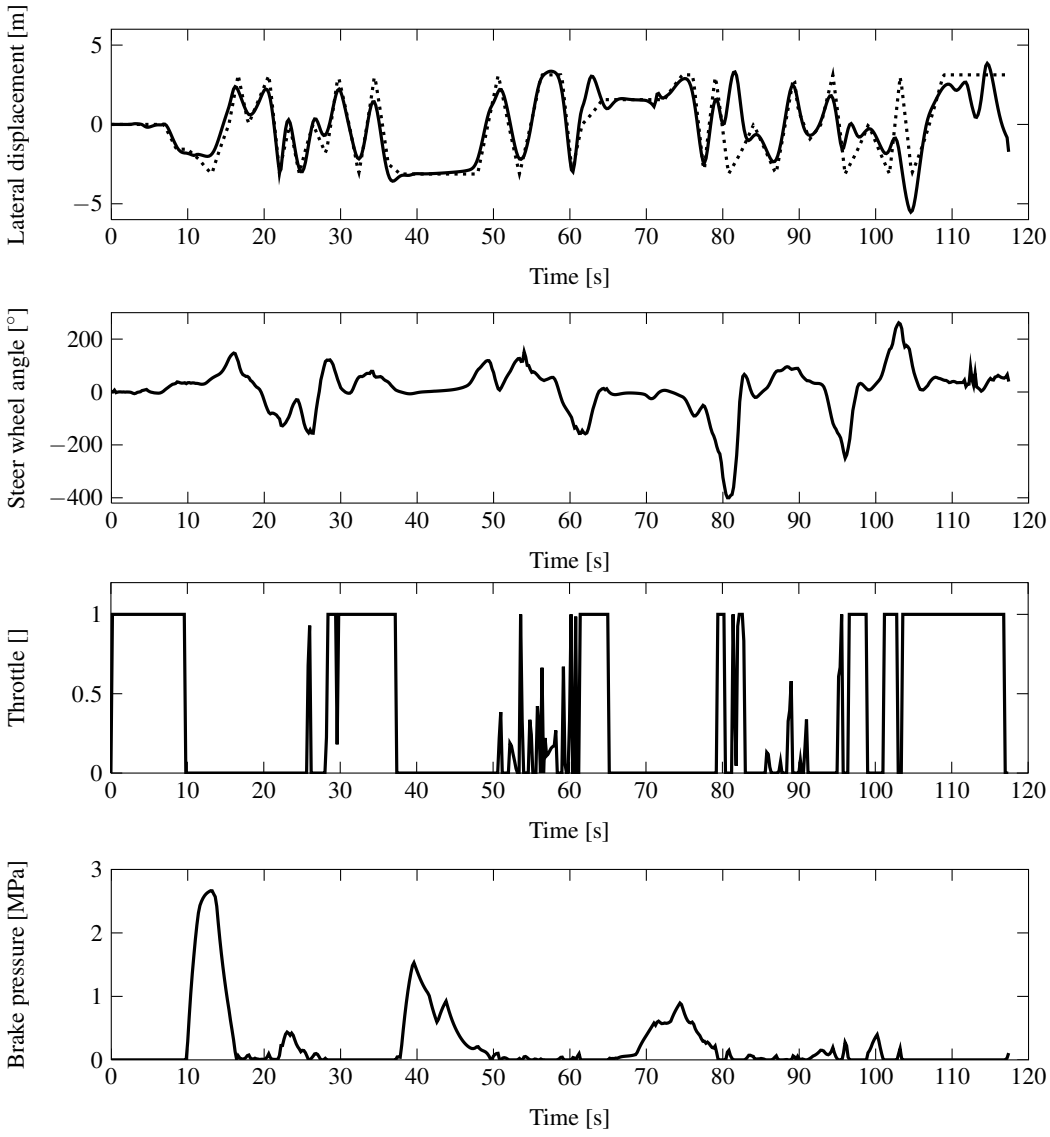

Figure 4.9: *Formula463 driver model path following capability*. This figure illustrates path following capability of the hybrid driver model, along with the control signals determined through a simulated racing lap, within the Formula463 project. The driver model control signals and lateral offset (black) and the intended lateral offset (dotted) are shown. Through the simulations conducted within this project, it has been shown the hybrid driver model structure developed is robust with regard to changes in vehicle design parameters.

4.3 Summary

This chapter detailed the modelling of human drivers for closed-loop vehicle dynamics simulation. To this end a tunable and robust driver model was developed capable of determining driver control inputs from vehicle and road data.

First a novel method for path determination using mapped track elements and genetic algorithms was presented. The mapped road geometry definition and implementation developed were shown to provide detailed information of the road geometry from planar information of the road edges. This definition has the potential to overcome potential shortcomings of other definitions and is well suited for the optimal path planning problem. An example was presented where intended path geometry and velocity profiles were determined from road geometry and vehicle data. In this case, a genetically based search algorithm minimizing traversing time was used, and the fitness of the determined solutions was shown to improve as the number of iterations increased. The method presented was shown to determine intended path information with minimal user input and *a priori* knowledge.

The modelling of the longitudinal and lateral stabilization tasks of the driver were also presented and model predictive control techniques were detailed. Software implementations of the detailed methods have been used to show the dependence on driver preview time on the steering response of the driver. As well, a hybrid longitudinal control scheme incorporating a finite state machine reference value calculation was shown to be robust in various vehicle control cases.

Finally, applications of the developed hybrid driver model to closed-loop vehicle dynamics simulations were presented. First, the the developed path planning algorithm and driver models were shown to determine driver control inputs from simple road and vehicle data. Next, the driver model developed was shown to be robust to vehicle design parameters through application to the Formula463 virtual grandprix project, in which the driver model controls student designed vehicles around a simulated race circuit.

The driver modelling tools and techniques detailed within this chapter have been shown to tunable and robust, while correlating well with experimental data. The developed driver model was shown to be beneficial in closed-loop vehicle simulations, that are capable of reducing the time and cost associated with developing and analyzing vehicle dynamics control systems.

Chapter 5

Vehicle Dynamics Control Development

The previous chapters detailed the development of driver and vehicle models for the analysis of stability and handling response. To attempt to improve upon the inherent vehicle responses, the use of active dynamics control is proposed. This chapter details the development of a set of model-based closed-loop integrated steer and yaw moment control strategies for road vehicles with imposed design and actuator constraints. To illustrate the proposed methods, an application of the developed controls to a prototype hybrid vehicle configuration is presented.

5.1 Vehicle Motion

The development of an active control requires a suitable trajectory or set of reference states, defining the desired response of the system. In the case of vehicle control, these trajectories may take the form of a desired path or vehicle states, given road geometry, or an internal reference model respectively. Typically, these methods produce conventional trajectories emulating those of conventional road vehicles; however, more unconventional trajectories may be followed in cases with increased control actuators [38]. While it is believed that the driver attempts to control the yaw rate of the vehicle, it has been shown that simultaneously tracking both yaw rate and side slip angle reference states can provide benefits in handling and stability [61, 88].

In the current research, conventional yaw rate and side slip angle trajectories are determined using reference models automatically generated using the EoM implementation presented in Chapter 2. Specifically, the two DOF yaw-plane models generated are used to predict the desired yaw rate and side slip velocity response of the driver.

5.2 System Actuators

Generally, active control systems require actuators that convert control signals into forces and moments that act on the system. In a road vehicle, potential actuators include chassis components such as steering, braking and active suspension systems, as well as mechanical and electrical powertrain systems. In an ideal case, full unlimited control over every facet of the vehicle would be possible. This would allow for optimal control over the efficiency, handling, and stability of the vehicle. However, this ideal is rarely achieved, as limitations exist imposed by physical hardware and alternative design criteria, namely cost.

The research conducted was part of AUTO21 projects E03-RGB and E301-EHV, which focused on improving the efficiency and safety of hybrid vehicles. Within this scope, a number of series and parallel hybrid vehicle configurations of varying complexity were evaluated, investigating the effect of powertrain layout on active control. The three motor configuration shown in Figure 5.1 was chosen to illustrate the proposed control methods, as the powertrain layout is well suited for various control strategies, while imposing a set of constraints short of the optimal case given in [58]. Within this vehicle configuration, the driving and braking motor torques on the front driveshafts are identical, while independent control of the driveshaft torques on the rear axle is possible. A steer by wire actuator is added to the front wheels to investigate the mitigation of steer effects caused by drive torques applied to the steered front wheels, as well as the effect of active steering on the efficacy of yaw moment control. The actuator configuration given can also be shown to complicate the control problem, as input-output uniqueness is not guaranteed with a potential manifold set of solutions to the control allocation problem.

5.3 Open-loop Response

The actuators chosen for the control system must be capable of modulating the response of the system. Within the presented vehicle architecture, both steering and direct yaw moment about the vertical axis of the vehicle are chosen as potential inputs to the system. An open-loop analysis can be conducted to determine the suitability of each possible control actuator. First, a linear analysis can be conducted considering the augmented two DOF yaw-plane model as

$$\begin{bmatrix} m & 0 \\ 0 & i_z \end{bmatrix} \begin{Bmatrix} \dot{v} \\ \dot{r} \end{Bmatrix} + \begin{bmatrix} \dfrac{(c_f + c_r)}{u} & \dfrac{(l_f c_f - l_r c_r)}{u} + mu \\ \dfrac{(l_f c_f - l_r c_r)}{u} & \dfrac{(l_f^2 c_f + l_r^2 c_r)}{u} \end{bmatrix} \begin{Bmatrix} v \\ r \end{Bmatrix} = \begin{bmatrix} c_f & 0 \\ l_f c_f & 1 \end{bmatrix} \begin{Bmatrix} \delta_f \\ \wp_z \end{Bmatrix} \tag{5.3.1}$$

where $\wp_z$ is the direct yaw moment about the vertical axis of the vehicle imparting no lateral force. By setting δ_f to zero, steady-state transfer functions relating side slip angle and yaw rate to the direct

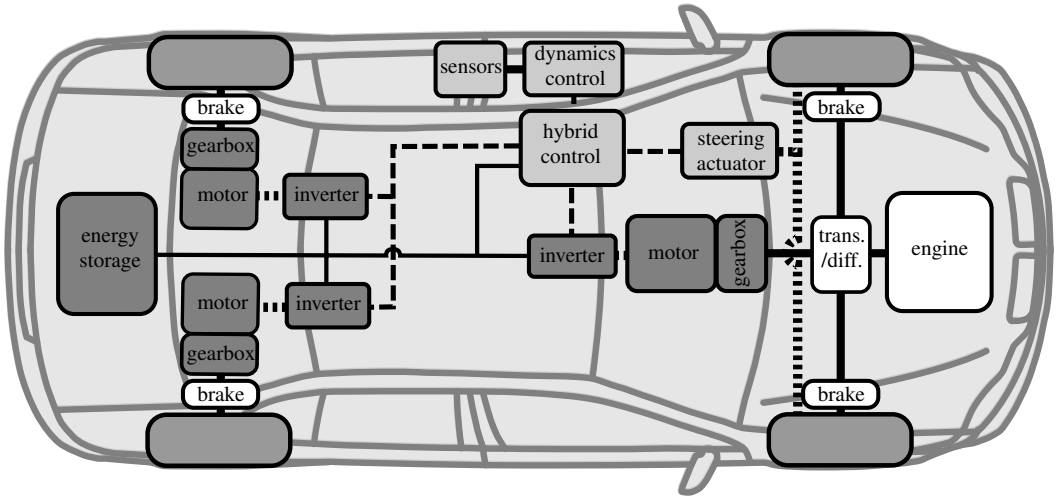

Figure 5.1: *Proposed hybrid architecture for BMW 330i*. During the course of AUTO21 projects E03-RGB and E301-EHV a number of hybrid powertrain architectures have been proposed and evaluated. One such architecture well suited for application of yaw moment control is comprised of a mechanical internal combustion engine with three electric motors and an energy storage bank. In this figure solid lines indicate electrical and mechanical power transfer connections, dotted lines indicate control connections, and dashed lines indicate data connections.

yaw moment can be expressed as

$$\frac{\beta}{\wp_z} = \frac{1 + \dfrac{mu^2}{(l_f c_f - l_r c_r)}}{\dfrac{(l_f + l_r)^2 c_f c_r}{(l_f c_f - l_r c_r)} - mu^2} \tag{5.3.2}$$

$$\frac{r}{\wp_z} = \frac{\dfrac{(c_f + c_r)}{(l_f c_f - l_r c_r)} u}{\dfrac{(l_f + l_r)^2 c_f c_r}{(l_f c_f - l_r c_r)} - mu^2} \tag{5.3.3}$$

Alternatively, a set of nonlinear open-loop simulations can be conducted to determine the input-output response of the system in the presence of nonlinearities. Figure 5.2 illustrates the output-to-input normalized linear and nonlinear steer and direct yaw moment input response with forward speed ranging from 0-40 m/s. It can be seen that, the transfer functions developed with the augmented linear two DOF model accurately predict both the side slip angle and yaw rate response of the vehicle in the presence of both applied steer angle and direct yaw moment. Also, the effective-

ness of steer input to modulate side slip angle and yaw rate of the vehicle deteriorates at speeds greater than 30 m/s, where nonlinear tire response is present. This nonlinear deterioration can cause reduced effectiveness of active front wheel steer controls in this region. The side slip angle and yaw rate response of the vehicle in the presence of applied yaw moment are shown to exhibit a more linear characteristic. However, it can be seen that the nonlinear vehicle exhibits a large slip angle response leading to a spin instability at 40 m/s with an applied yaw moment of 2500 N·m. This spin occurs at a speed where large drive forces are required on the rear wheels to maintain the high forward speed leading to tire saturation, limiting the vehicle to a lateral acceleration of 0.5 g's.

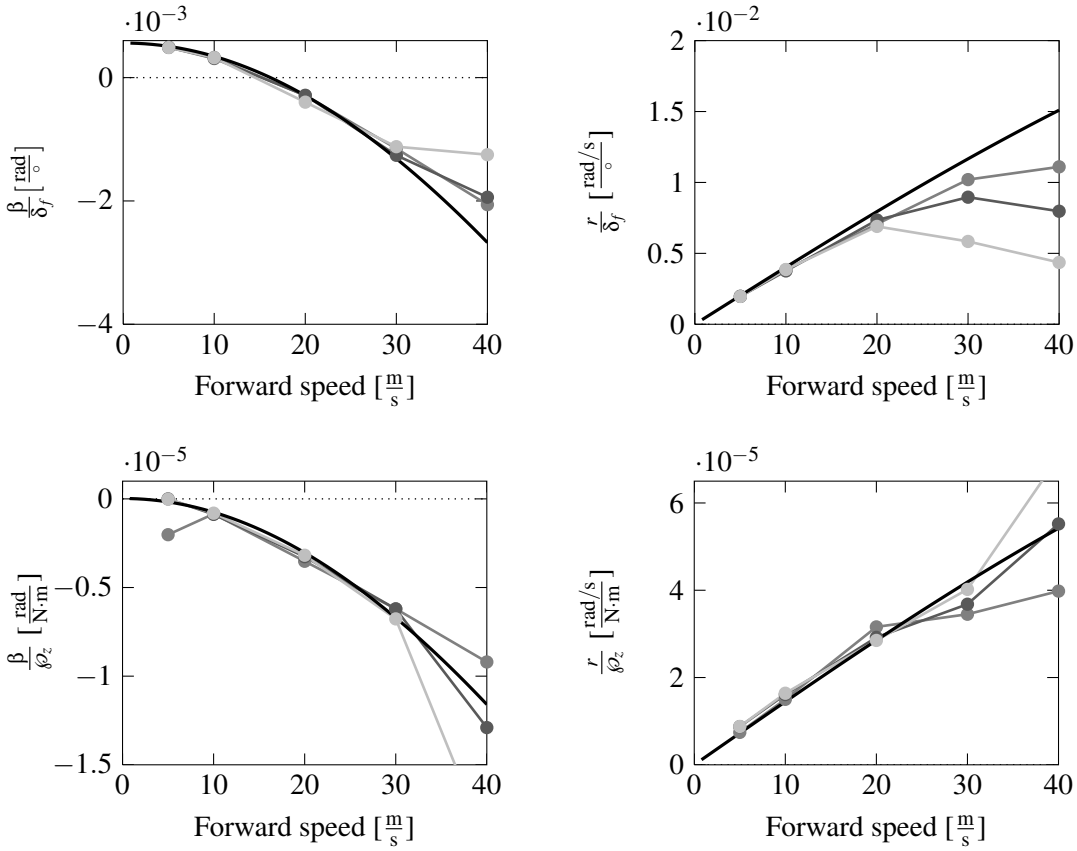

Figure 5.2: *Normalized steady-state vehicle response to input*. The figure presents the normalized side slip angle (left) and yaw rate (right) response of the nominal vehicle to changes in steering wheel angle (top) and applied direct yaw moment (bottom). The solid black line indicates both the hand and EoM derived transfer functions using a two DOF yaw-plane model. The marked gray lines indicate the normalized open-loop response predicted using the CarSim® model. In the top figures steering wheel angles of 10 (gray), 25 (dark gray) and 50 (light gray) degrees are shown. The bottom figures illustrate the response of the vehicle to an external moment about the vertical axis of the vehicle of 1000, 2000 and 2500 N · m.

5.4 Active Controller

In the vehicle control case presented the control problem can be broken into three separate problems to determine the appropriate control signals. The first problem is to determine the driver intentions, the second is to determine the appropriate control action, and the last is to allocate the control signals to the appropriate control actuators given a potentially under or over actuated control system. To achieve the control goal a hierarchical control structure is proposed. This structure is comprised of separate components to interpret the driver intentions, determine required control requests and allocate control requests to the actuators of the system as shown in Figure 5.3.

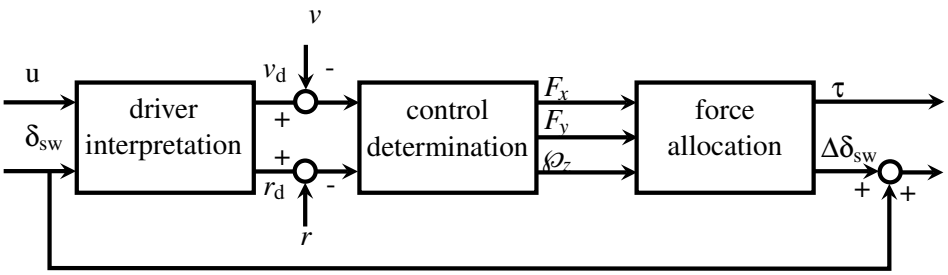

Figure 5.3: *Hierarchical control structure*. The figure presents the hierarchical control structure proposed for the human controlled vehicle system. The control is comprised of components to interpret the driver intentions, determine required control requests and allocate control requests to the actuators of the system.

5.4.1 Linear Control

A method for automatic generation of control gains was desired to minimize the development time of vehicle dynamics controls. To this end, a method capable of interfacing with the developed EoM implementation of the method for generating linearized equations of motion presented in Chapter 3 was desired, allowing for the analysis of ever more complicated systems. As the equations developed by the detailed method are linearized, linear control methods can be easily applied. Linear control methods can be applied to linear systems and systems where minimal nonlinearities occur about the operational point or region. These linear controls can be used to stabilize or alter the response of the system. Given the state-space form of a LTI system in Equations 3.1.17 and 3.1.18 a full-state feedback control can be defined as

$$\boldsymbol{u} = \mathbf{K}_c \boldsymbol{q} \tag{5.4.1}$$

Table 5.1: *Linear quadratic regulator gains @ 70 km/h*. The diagonal elements of the Q matrix are the yaw rate and lateral velocity error weightings. The diagonal elements of the R matrix are the steering wheel angle and direct yaw moment penalty weightings.

Configuration	diag($\mathbf{Q}$)	diag($\mathbf{R}$)	$\mathbf{K}_{\text{lqr}}$
1 forward COG	[3e5,2e4]	[5e0,1e-5]	[-61.018,16.365;-1.4058e+05,-10002]
2 forward COG	[1e5,1e4]	[5e0,1e-5]	[-30.729,7.7422;-73062,-6798.8]
3 forward COG	[3e5,0]	[5e0,1e-5]	[-65.868,0.58945;-1.3639e+05,1164.3]
4 forward COG	[3e5,0]	[5e5,1e-5]	[-0.0006892,6.4845e-06;-1.4263e+05,1279.7]
5 forward COG	[0,4e4]	[5e0,1e-5]	[3.6447,19.532;-31283,-30289]
6 forward COG	[0,4e4]	[5e5,1e-5]	[3.9216e-05,0.00020271;-32304,-31535]
7 rearward COG	[3e4,2e4]	[1e0,1e-5]	[-70.008,10.519,-1.395e+05,-12111]

where $\mathbf{K}_{\text{c}}$ is a matrix of control gains that can be determined using an optimal control method such as the linear quadratic regulator (LQR) or similar methods. The LQR requires that the system model must be controllable and observable or at least stabilizable and detectable, stipulating that the system be minimal. While a minimal realization is not guaranteed by the previously discussed method for automatic generation of the equations of motion, one can be obtained readily from the resulting equations. The optimal LQR control gains can be found to minimize the penalty function, expressed as

$$j = \int_0^\infty \left(\boldsymbol{q}^{\text{T}}\mathbf{Q}\boldsymbol{q} + \boldsymbol{u}^{\text{T}}\mathbf{R}\boldsymbol{u}\right) dt \tag{5.4.2}$$

where $\mathbf{Q}$ and $\mathbf{R}$ are user defined positive definite penalty matrices associated with the state and control input respectively. The $\boldsymbol{q}^T\mathbf{Q}\boldsymbol{q}$ term minimizes the weighted squared state error, where the $\boldsymbol{u}^T\mathbf{R}\boldsymbol{u}$ minimizes the control energy. The control gain matrix satisfying this cost function is

$$\mathbf{K}_{\text{lqr}} = -\mathbf{R}^{-1}\mathcal{B}^{\text{T}}\mathbf{P} \tag{5.4.3}$$

where $\mathbf{P}$ is the matrix determined by solving the matrix Riccatti equation

$$\mathbf{P}\mathcal{A} + \mathcal{A}^{\text{T}}\mathbf{P} - \mathbf{P}\mathcal{B}\mathbf{R}^{-1}\mathcal{B}^{\text{T}}\mathbf{P} + \mathbf{Q} = \mathbf{0} \tag{5.4.4}$$

The LQR control gains determined using the two DOF model for a set of vehicle configurations and penalty weightings with a forward speed of 70 km/h are presented in Table 5.1. In this case, the system states are yaw rate and lateral velocity respectively, with steer and direct yaw moment inputs. It can be seen that the optimal control gains can vary widely based on the user specified penalty weightings, and that care should be taken to appropriately assign these values.

The described LQR requires full-state feedback to properly determine the control inputs. In

reality, some states may not be sensed or measured within a given application. Various methods can be applied to account for this shortcoming, including the use of state observers [53, 49] and sub-optimal partial state feedback methods, as proposed by Cai [13].

Linear State Observers

States and quantities that are not readily measured using sensors can be estimated using state observers [53, 49]. A linear high gain observer can be used to make an asymptotic estimate of state output measurements. Given an observable LTI system $[\mathcal{A}, \mathcal{C}]$ the separation principle can be used to design a high gain observer apart from any system controller [41]. Assuming the estimator form

$$\dot{\hat{\boldsymbol{q}}} = \mathcal{A}\hat{\boldsymbol{q}} + \mathcal{B}\boldsymbol{u} + \mathbf{H}(\boldsymbol{z} - \hat{\boldsymbol{z}}) \tag{5.4.5}$$

where $\mathbf{H}$ is a vector of observer gains with $\hat{\boldsymbol{q}}$ and $\hat{\boldsymbol{z}}$ the state and output estimates respectively. In this formulation the $\mathbf{H}(\boldsymbol{z} - \hat{\boldsymbol{z}})$ term is a proportional output error feedback, rejecting output error. The estimate and the rate of error can be expressed as

$$\begin{aligned} \hat{\boldsymbol{e}} &= \boldsymbol{q} - \hat{\boldsymbol{q}} \\ \dot{\hat{\boldsymbol{e}}} &= (\mathcal{A} - \mathbf{H}\mathcal{C})\,\hat{\boldsymbol{e}} \end{aligned} \tag{5.4.6}$$

where $\mathbf{H}$ is chosen Hurwitz to guarantee the error $\boldsymbol{e}$ of the full-state estimation converges to zero as time approaches infinity. In many cases, full-state observation may not be required as certain states may be measured with sensors. A Luenberger reduced state observer can be used to estimate only the states that are not measured [49]. However, for the research, the presence of noise and modelling uncertainty limited the application of high gain reduced order linear observers, as inferior state estimates were generated when compared to the full state case. This can be attributed to the use of measured states from the nonlinear plant being used directly in the observer state, causing the effects of noise and uncertainty to be amplified by the required high observer gains.

The determination of observer gains can be accomplished by hand for small systems, however, search methods such as those proposed by Yang [87] are more beneficial for larger systems, or where equations of motion are generated using automatic means. The method proposed determines the observer gains by solving a least squares minimization using using a Levenberg-Marquardt 'trust region' based search algorithm, that can be shown to converge quadratically near the solution. The observer gain search problem can be expressed as

$$\min_{\mathbf{H} \in \mathbb{R}^{m \times n}} \frac{1}{2} \left\| \boldsymbol{\lambda}(\mathcal{A} + \mathcal{B}\mathbf{H}\mathcal{C}) - \boldsymbol{\lambda}_d \right\|_2^2 \tag{5.4.7}$$

where $\mathbf{H}$ is determined to minimize the error between the desired and observed system eigenvalues

$\boldsymbol{\lambda}_d$ and $\boldsymbol{\lambda}$. To ensure eigenvalue differentiability within the trust region, the desired eigenvalues must be distinct, or at least distinct with small separation. This requires small perturbations to be applied to repeated poles in the desired eigenvalue vector, as can be present in vehicle models containing modes with oscillatory response or symmetric suspensions.

5.4.2 Nonlinear Control

The presence of large nonlinearities and unmodelled system dynamics around the operational point may reduce the effectiveness of linear controls, leading to a need for robust nonlinear control methods. Sliding mode control (SMC) has been shown to be effective in the presence of nonlinear plant response and external disturbances. For the given vehicle control case, a state tracking SMC can be developed given a reference model

$$\dot{\boldsymbol{q}} = \mathcal{A}\boldsymbol{q} + \mathcal{B}\boldsymbol{u} + \boldsymbol{\sigma} \tag{5.4.8}$$

where $\boldsymbol{\sigma}$ is a vector of disturbances acting on the system. A sliding surface can be defined as the tracking error between the desired and measured system outputs as

$$\chi = \mathcal{C}^T(\boldsymbol{q} - \boldsymbol{q}_d) \tag{5.4.9}$$

where $\boldsymbol{q}_d$ is the desired state vector. A yaw rate tracking control can then be developed as

$$\wp_z = \frac{1}{\mathcal{B}_2}[-\mathcal{A}_{21}v - \mathcal{A}_{22}r + \dot{r}_d - k_1(r - r_d) + k_2 \text{sat}\left(\frac{\chi}{\varepsilon}\right)] \tag{5.4.10}$$

where k_1 and k_2 are positive constants. The saturation function $\text{sat}(\frac{\chi}{\varepsilon})$ is used to eliminate control chattering due to the switching discontinuity near the sliding surface χ, defining a boundary layer of linearity about the sliding surface. The non-linear gain k_2 can be found to satisfy the surface reaching condition in the presence of the parameter uncertainties that occur over the operational range of the vehicle where

$$\frac{1}{2}\frac{d}{dt}s^2 \leq -\eta|s| \tag{5.4.11}$$

where η is a positive constant. This method was applied to the development of a control law in [71].

5.5 Control Allocation

The addition of individual wheel torques to the control of a road vehicle can create an over-actuated system, where manifold solutions to the control problem are possible. In this case, a direct yaw moment can be generated using one, or a combination of various forces generated at the wheels. Therefore, the allocation of control forces amongst the possible actuators must be considered. This

is similar to applications in aviation, where aircraft with coupled roll-yaw surfaces or thrust vectoring have redundant actuators. Various approaches have been proposed to solve this problem, including manual static allocation, and using allocation methods that impose further constraints on the control problem eliminating the manifold solutions.

5.5.1 Direct Allocation

Direct allocation of control requests may be achieved by setting user defined algorithms. These algorithms can be very development intensive and require care of the designer to specify algorithms for each operating condition. In the case presented in [71], a direct allocation algorithm was developed where YMC control forces were determined by dividing requests equally across both rear drive motors as

$$\Delta\tau = \frac{2\wp_z r_e}{l_t} \tag{5.5.1}$$

where $\Delta\tau$ is the torque difference between the motors on the rear axle. A limit on the control force was enforced given the saturation of the individual rear tire. The developed control was applied within a model of a hybridized Chrysler Pacifica, with independent drive motors on the rear wheels. In this case, the control attempted to track a neutral steering reference model through a double lane change with varying road friction with a forward speed of 80 km/h, with open-loop driver steer input. The simulated results are presented in Figure 5.4. It can be seen that the uncontrolled vehicle (FWD) exhibits a spin instability while the controlled vehicle (VTD) remains relatively on course tracking the reference model. The normalized force plot shows that the right rear tire becomes saturated at 2.7 seconds, given the symmetrically distributed motor torques. It can be seen that the motors are saturated in order to track the reference in the given configuration. To reduce the amount of motor saturation additional actuators could be added; however, this would further complicate the definition algorithms capable of direct allocation of control forces.

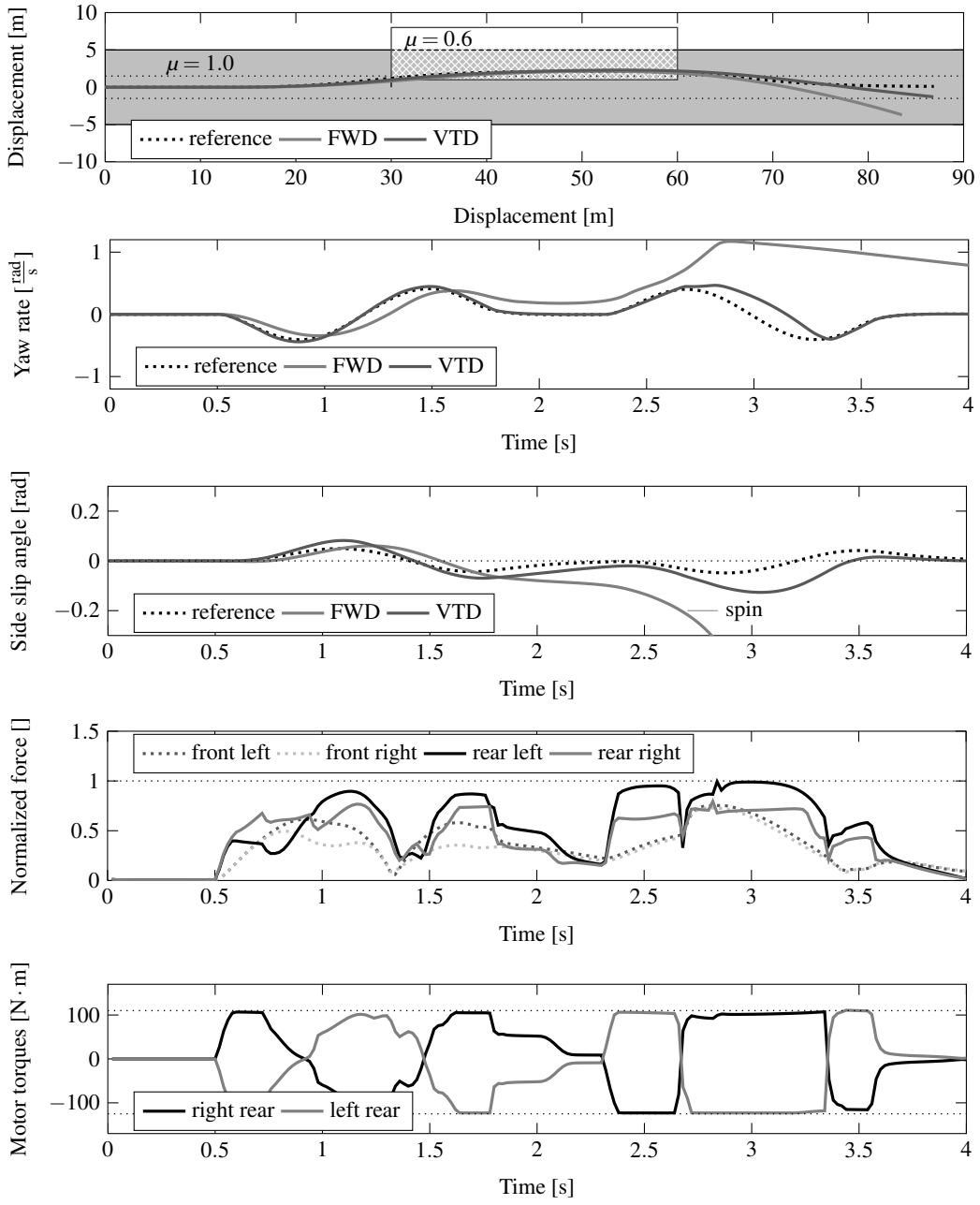

Figure 5.4: *Direct control allocation example: double lane change*. This figure illustrates the double lane change response of a 2004 Chrysler Pacifica with open-loop driver steer input. The controlled vehicle (black) is shown to have increased tracking capability to the reference vehicle (dotted), when compared to the uncontrolled vehicle (gray). The applied motor torques are symmetric, and reach saturation at various points throughout the simulated test manoeuvre. The applied yaw moment control maintains the vehicle stability throughout the manoeuvre.

5.5.2 Indirect Allocation

Indirect allocation algorithms have been shown to be powerful tools in the determination of control values in over-actuated systems as detailed by [32, 12, 7]. Many of these algorithms attempt to enforce added rules, constraints, objectives and limits on the system and actuators to eliminate manifold solution conditions. This allows a unique mapping between the required actuator signals and the desired global control forces. In the case of the planar motion of a road vehicle, the global control and effector forces can be related as

$$\boldsymbol{F} = \begin{bmatrix} \boldsymbol{F}_{\mathrm{x}} \\ \boldsymbol{F}_{\mathrm{y}} \\ \wp_{\mathrm{z}} \end{bmatrix} = \mathbf{E}\boldsymbol{f} \tag{5.5.2}$$

where $\boldsymbol{F}$ is a vector of global control signals in vehicle frame, comprised of the desired longitudinal and lateral forces $\boldsymbol{F}_{\mathrm{x}}$ and $\boldsymbol{F}_{\mathrm{y}}$, as well as the desired yaw moment $\wp_{\mathrm{z}}$. A transformation matrix $\mathbf{E}$ relating forces $\boldsymbol{f}$ in the tire reference frame to forces in the vehicle reference frame can be expressed for the given configuration as

$$\mathbf{E} = \begin{bmatrix} \cos\delta_{\mathrm{f}} & -\sin\delta_{\mathrm{f}} & \cos\delta_{\mathrm{f}} & -\sin\delta_{\mathrm{f}} & 1 & 1 \\ \sin\delta_{\mathrm{f}} & \cos\delta_{\mathrm{f}} & \sin\delta_{\mathrm{f}} & \cos\delta_{\mathrm{f}} & 0 & 0 \\ -l_{\mathrm{t}}\cos\delta_{\mathrm{f}} & l_{\mathrm{f}}\sin\delta_{\mathrm{f}} & l_{\mathrm{t}}\cos\delta_{\mathrm{f}} & l_{\mathrm{f}}\sin\delta_{\mathrm{f}} & -l_{\mathrm{t}} & l_{\mathrm{t}} \end{bmatrix} \tag{5.5.3}$$

where $\boldsymbol{f}$ in the tire reference frame can be expressed as

$$\boldsymbol{f} = \begin{bmatrix} f_{x_1} \\ f_{y_1} \\ f_{x_2} \\ f_{y_2} \\ f_{x_3} \\ f_{x_4} \end{bmatrix} = \hat{\boldsymbol{f}} + \tilde{\boldsymbol{f}} \tag{5.5.4}$$

where the tire force vector is broken into two components. The vector of the current estimated wheel forces is $\hat{\boldsymbol{f}}$, and $\tilde{\boldsymbol{f}}$ is the change in planar forces from the control, as illustrated in Figure 5.5. The system is under-constrained with three global forces and six possible wheel forces with steering, brake and drive motor effectors. This over-actuation problem can be resolved by placing additional constraints, objectives and penalties on the allocation.

5.5.3 Allocation Limitations

Various limitations can be enforced on the system to ensure stability by minimizing the possibility of tire and motor saturation. As discussed in Section 3.2.1, there is a finite resultant force that can be generated by a tire, so for a given operating condition there is a limit to the amount of control force that can be applied, as shown in Figure 5.5a. The magnitude of this vector can be used to define a stable search region for the allocation algorithm. This envelope ensures that as the tire nears saturation, the change in force allowed will be reduced, minimizing the chance of unfavourable control forces. Similarly, actuator limits of the electric motors can be addressed, as shown in Figure 5.5b. At an operational speed, the torque required to maintain longitudinal speed reduces the availability of motor torque for additional control applications. Additional effector limitations, including those of braking and steering actuators can also be considered. These limits can be combined to define a feasible search space for the control allocation, as shown in Figure 5.5c.

Tire Forces

Pneumatic tires exhibit a limited force generating capability, limiting on the magnitude of the possible control force $\bar{f}$ for a given operating condition as illustrated in Figure 5.5a. However, the determination of this quantity relies on measurements or estimations of the current forces on the tire. In order to achieve this, an algorithm was developed where the vertical, longitudinal and lateral forces on the tires could be estimated, given sensor measurements of longitudinal, lateral accelerations and yaw rate.

Under the proposed algorithm, the planar forces at each tire are required. The work of Daily [20] proposed a method to accomplish this, relying on global positioning system (GPS) data, predicting tire forces quite well. However, a minimum set of sensors was desired for application, so a similar method was developed to reduce the amount of required sensor data. The planar motion of the vehicle can be expressed using

$$-f_{\mathrm{x_r}} - f_{\mathrm{x_f}}\cos\delta_{\mathrm{f}} - f_{\mathrm{y_f}}\sin\delta_{\mathrm{f}} = ma_{\mathrm{x}} \tag{5.5.5}$$

$$f_{\mathrm{y_r}} - f_{\mathrm{x_f}}\sin\delta_{\mathrm{f}} + f_{\mathrm{y_f}}\cos\delta_{\mathrm{f}} = ma_{\mathrm{y}} \tag{5.5.6}$$

$$l_{\mathrm{f}}\left(f_{\mathrm{y_f}}\cos\delta_{\mathrm{f}} - f_{\mathrm{x_f}}\sin\delta_{\mathrm{f}}\right) - l_{\mathrm{r}}f_{y_r} + \frac{l_{\mathrm{t}}}{2}\left(\Delta f_{x_r} + \Delta f_{\mathrm{x_f}}\cos\delta_{\mathrm{f}} - \Delta f_{\mathrm{y_f}}\sin\delta_{\mathrm{f}}\right) = i_{\mathrm{z}}\dot{r} \tag{5.5.7}$$

where $f_{\mathrm{x_f}}$,$f_{\mathrm{x_r}}$ and $f_{\mathrm{y_f}}$ and $f_{\mathrm{y_r}}$ are the axle forces in the longitudinal and lateral vehicle directions respectively. The difference in force across the front and rear axles is given by $\Delta f_{\mathrm{x_f}}$ and $\Delta f_{\mathrm{x_r}}$ respectively, where the steer angles of the rear axles are assumed fixed. The equations can be rearranged

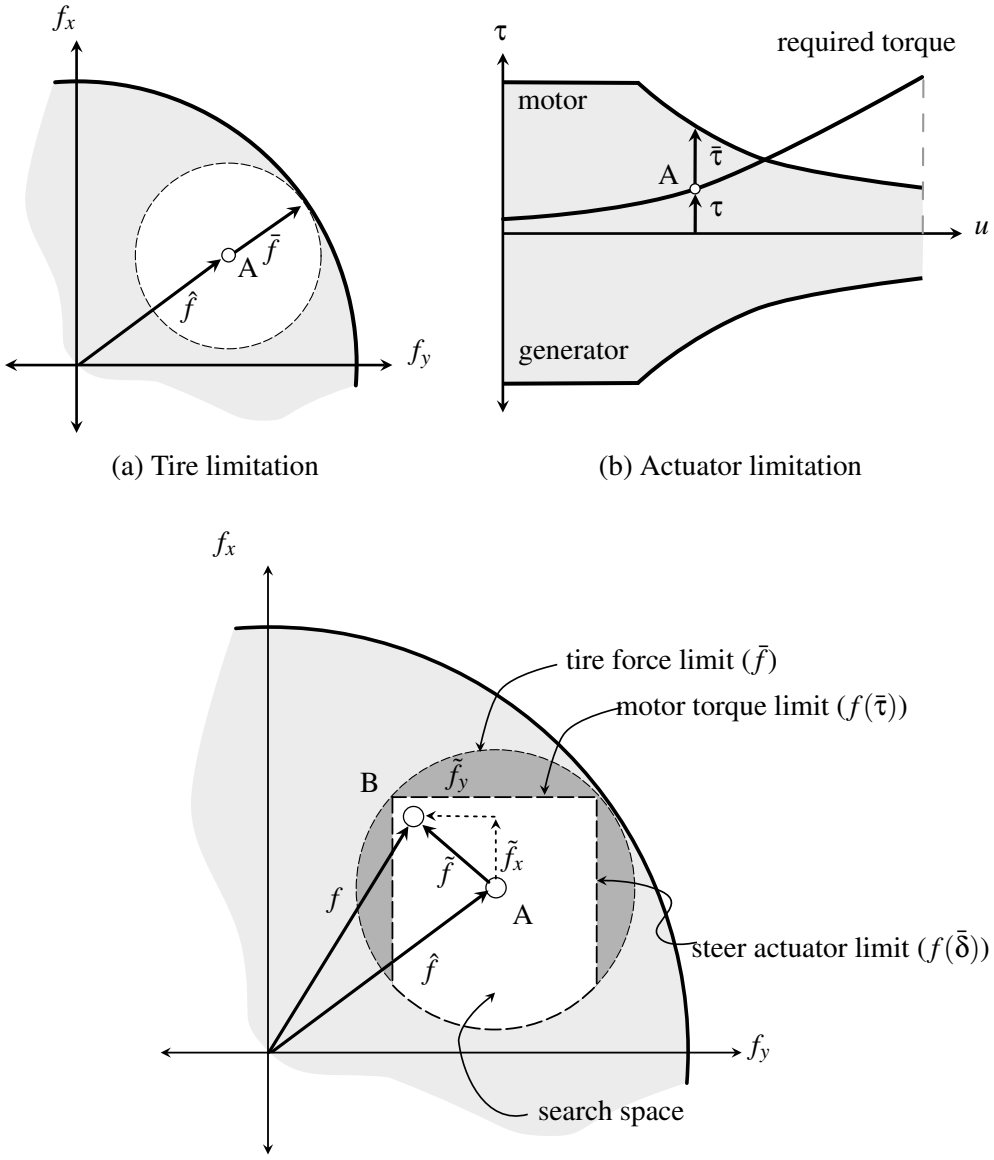

(a) Tire limitation

(b) Actuator limitation

(c) Combined limitations

Figure 5.5: *Control allocation search region*. The control allocation search space is defined using tire (a) and actuator force (b) limits that are inherent and imposed on each wheel of the vehicle. The control force allocation divides the total force into two components, the current (estimated) force $\hat{f}$ and the allowable force $\bar{f}$ for operational condition A. Figure (c) illustrates the combined search region, with the allocated force $\tilde{f}$ with the components $\tilde{f}_x$ and $\tilde{f}_y$ leading to operational condition B with the total force f. The inherent and imposed limits may reduce the ability of the allocation algorithm to achieve desired response, but serve to minimize loss of control situations due to instability.

to solve for the lateral axle forces, yielding

$$\begin{Bmatrix} \hat{f}_{\mathrm{y_f}} \\ \hat{f}_{\mathrm{y_r}} \end{Bmatrix} = \begin{bmatrix} \cos\delta_{\mathrm{f}} & 1 \\ l_{\mathrm{f}}\cos\delta_{\mathrm{f}} & -l_{\mathrm{r}} \end{bmatrix}^{-1} \begin{bmatrix} ma_{\mathrm{y}} + \hat{f}_{\mathrm{x_f}}\sin\delta_{\mathrm{f}} \\ i_{\mathrm{z}}\dot{r} - \dfrac{l_{\mathrm{t}}}{2}(\Delta\hat{f}_{\mathrm{x_r}} + \Delta\hat{f}_{\mathrm{x_f}}\cos\delta_{\mathrm{f}}) + l_{\mathrm{f}}\hat{f}_{\mathrm{x_f}}\sin\delta_{\mathrm{f}} \end{bmatrix} \tag{5.5.8}$$

where the longitudinal forces $\hat{f}_{\mathrm{x_f}}$ and $\hat{f}_{\mathrm{x_f}}$ can be approximated using quasi-static approximations as

$$\hat{f}_{\mathrm{x}_i} = \frac{\hat{\tau}_i}{r_{\mathrm{e}}} \tag{5.5.9}$$

where $\hat{\tau}_i$ is the estimated drive axle torque from the motor control unit where $i = 1,2,3,4$. The individual lateral tire forces can now be determined. Assuming that the slip angle on the left and right sides of the vehicle are the same, the lateral force developed by a given tire is significantly dependent on the vertical load of the tire. The vertical load on a tire in the presence of load transfer can be approximated using a load transfer analysis as in [62]. The load transferred longitudinally during acceleration can be expressed as

$$\Delta\hat{f}_{\mathrm{z}}^{l} = \left(\frac{ml_{\mathrm{h}} + \left(m + \dfrac{i_{\mathrm{w_f}}}{r_{\mathrm{e}}^2} + \dfrac{i_{\mathrm{w_r}}}{r_{\mathrm{e}}^2} \right) r}{l_{\mathrm{f}} + l_{\mathrm{r}}} \right) a_{\mathrm{x}} \tag{5.5.10}$$

where $\Delta\hat{f}_{\mathrm{z}}^{l}$ is the estimated longitudinal load transfer, and $i_{\mathrm{w_f}}$ and $i_{\mathrm{w_r}}$ are the front and rear rotational wheel inertias. The load transferred laterally can be expressed as

$$\Delta\hat{f}_{\mathrm{z}}^{*} = \frac{1}{l_{\mathrm{t}}} \left(\frac{k_{\mathrm{r_{f/r}}} mg\mathrm{hs}}{(k_{\mathrm{r_f}} + k_{r_{\mathrm{r}}} - mgh_{\mathrm{s}})} + f_{\mathrm{z}}^{\mathrm{s}} h_{\mathrm{rc}} \right) a_{\mathrm{y}} \tag{5.5.11}$$

where $\Delta\hat{f}_{\mathrm{z}}^{*}$ is the estimated lateral load transfer, and $f_{\mathrm{z}}^{\mathrm{s}}$ is the static vertical load at equilibrium. The total vertical load on the tires can be expressed as

$$\hat{f}_{\mathrm{z}_{2(i-1)+j}} = \frac{1}{2} \left(f_{\mathrm{z}_{2(i-1)+j}}^{s} + (-1)^{i-1}\Delta\hat{f}_{\mathrm{z}}^{l} \right) + (-1)^{j}\Delta\hat{f}_{\mathrm{z}}^{*} \tag{5.5.12}$$

where $i = 1,2$ corresponds to the front and rear axles, and $j = 1,2$ corresponds to the left and right sides of the vehicle. Assuming the vertical vehicle and tire axis are co-linear, the lateral load on the left and right side of the vehicle can now be expressed as

$$\hat{f}_{\mathrm{y}_{2(i-1)+j}} = \frac{\hat{f}_{\mathrm{z}_{2(i-1)+j}}}{\sum_{n=1}^{2} \hat{f}_{\mathrm{z}_{2(i-1)+n}}} \hat{f}_{\mathrm{y}_i} \tag{5.5.13}$$

where $\hat{f}_{y_i}$ represents the estimated lateral force on the front or rear axle.

With the approximations for the longitudinal, lateral and vertical forces at each tire the maximum allowable resultant force at each tire can be estimated as

$$\bar{f}_i = \mu_i \hat{f}_{z_i} - \sqrt{\hat{f}_{x_i}^2 + \hat{f}_{y_i}^2} \tag{5.5.14}$$

where μ_i is the friction coefficient.

Force Estimation Example

To illustrate the efficacy of the proposed estimation algorithm, a set of low and high lateral acceleration double lane change test manoeuvres were simulated with arbitrary disturbance wheel torques applied, as shown in Figure 5.6. The resulting estimations are shown in Figures 5.7 and 5.8. It can be seen that the vertical and lateral forces determined using the proposed method correlate well with simulation data obtained from CarSim®. The normalized tire force and allowable resultant force limit are also correlate well in the low lateral acceleration case. However, regions of reduced correlation to the simulated data given by the dotted lines can be seen in the high lateral acceleration case that can be attributed to the applied disturbance torques which are not considered in the force estimation calculations.

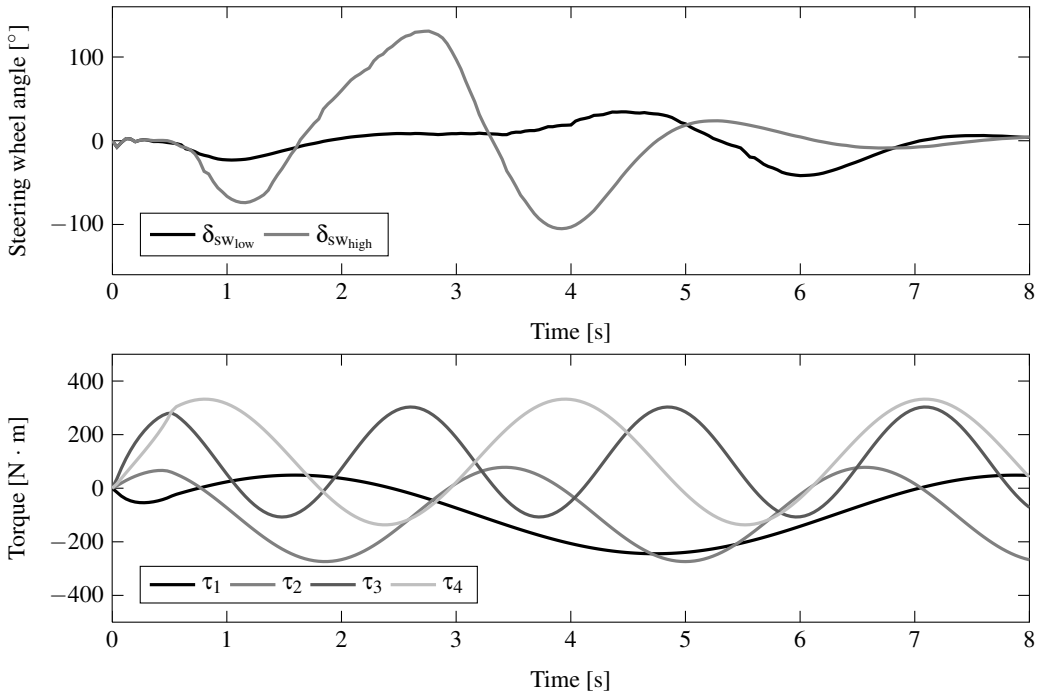

Figure 5.6: *Allocation algorithm test inputs: double lane change steer and arbitrary disturbance wheel torques*. This figure illustrates the steering wheel and arbitrary disturbance wheel torques applied during the low and high lateral acceleration simulated double lane change manoeuvres.

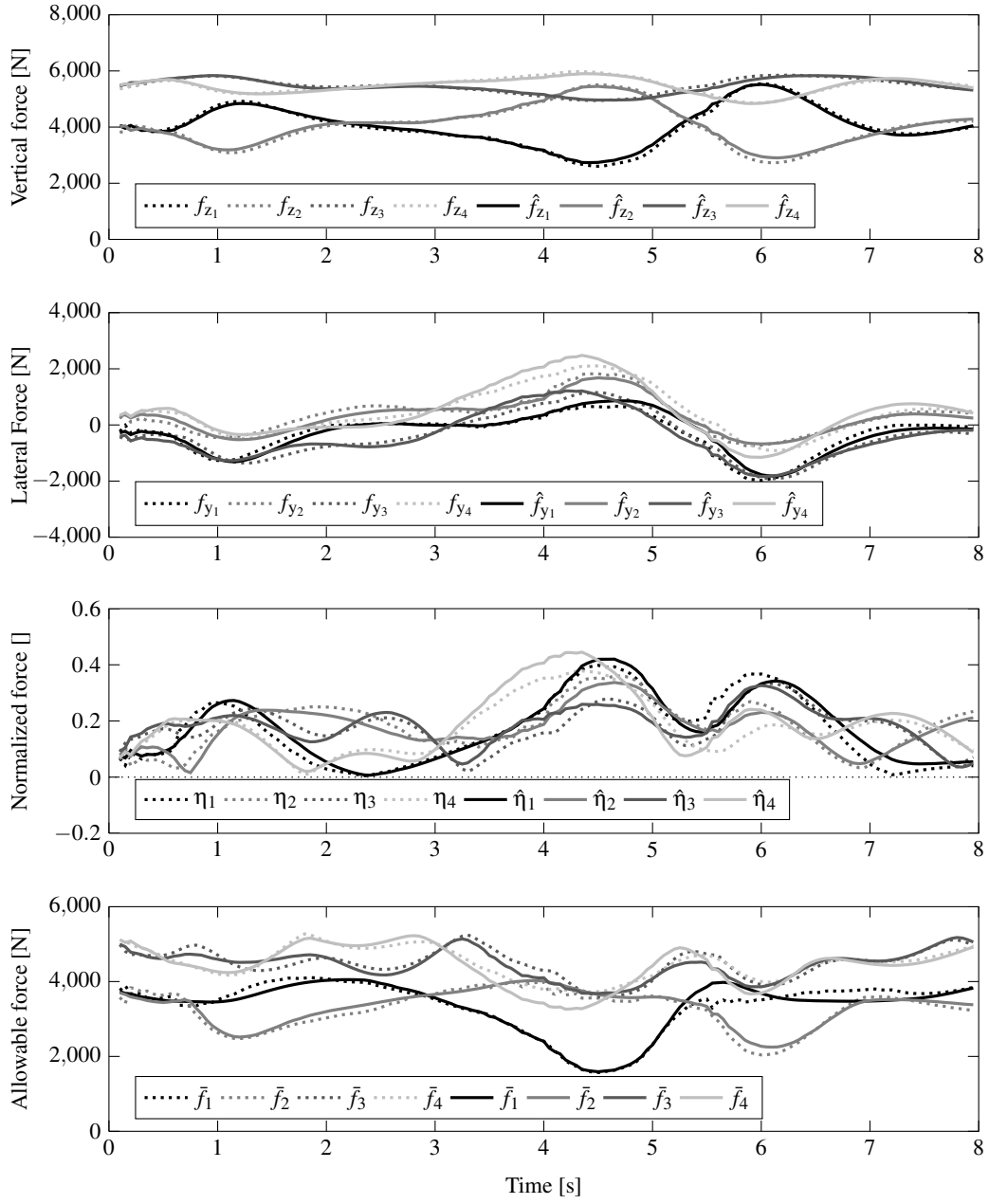

Figure 5.7: *Force estimation for double lane change: low lateral acceleration test.* Tire force estimation for a double lane change at 50 km/h, reaching a maximum 0.3 g lateral acceleration, with arbitrary wheel torques, for rearward centre of gravity configuration. Dashed lines show result from high-fidelity CarSim® model. The solid lines represent the appropriate estimated values, generated using sensor measurements from simulated open-loop test.

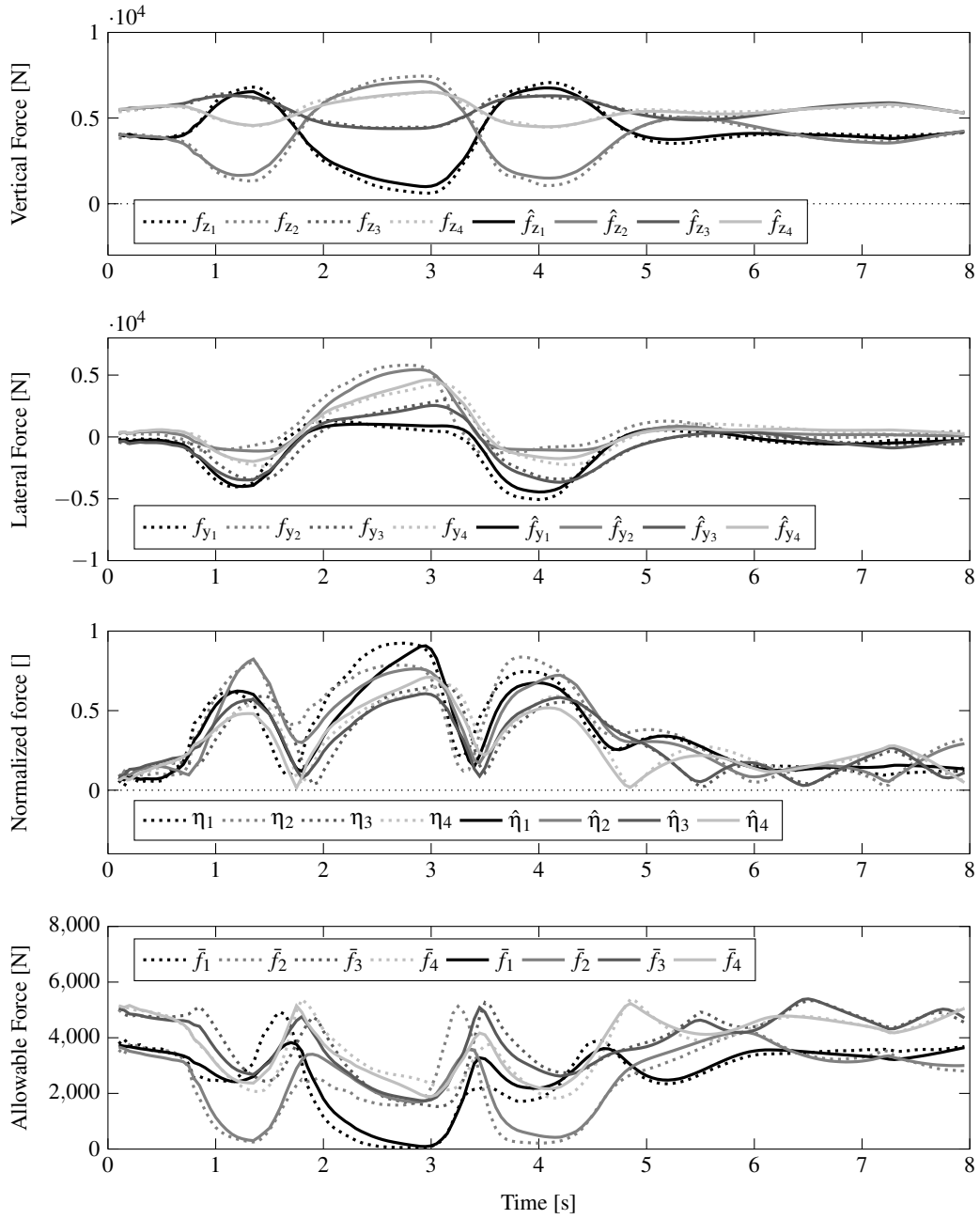

Figure 5.8: *Force estimation for double lane change: high lateral acceleration test.* Tire force estimation for a double lane change at 50 km/h, reaching a maximum 0.6 g lateral acceleration, with arbitrary wheel torques, for rearward centre of gravity configuration. Dashed lines show result from high-fidelity CarSim® model. The solid lines represent the appropriate estimated values, generated using sensor measurements from simulated open-loop test. It can be seen that the front left allowable tire force approaches zero between 2-3 seconds.

5.5.4 Allocation Problem

The allocation problem presented in Equation 5.5.2 can now be combined with a set of constraints and objectives in order to solve for the vector of allocated control forces $\tilde{\boldsymbol{f}}$. The problem can be expressed as a constrained linear least-squares minimization (LLSM) problem as

$$\begin{aligned} \min_{\tilde{\boldsymbol{f}}} \ & \frac{1}{2} \left\| \mathbf{W} \left(\mathbf{E}\tilde{\boldsymbol{f}} - \left(\boldsymbol{F} - \mathbf{E}\hat{\boldsymbol{f}} \right) \right) \right\|_2^2 \\ \text{s.t. } & \mathbf{G}\tilde{\boldsymbol{f}} = \boldsymbol{d} \\ \text{and } & \tilde{\boldsymbol{f}}_{min} \leq \tilde{\boldsymbol{f}} \leq \tilde{\boldsymbol{f}}_{max} \end{aligned} \tag{5.5.15}$$

where $\mathbf{W}$ is a diagonal matrix of weighting values representing the relative importance of the objectives. Control force limits $\tilde{\boldsymbol{f}}_{min}$ and $\tilde{\boldsymbol{f}}_{max}$ enforce the tire force, electric motor torque, and steer actuator limitations. The matrix set of constraint equations defined by the matrix $\mathbf{G}$ and vector $\boldsymbol{d}$, can be used to enforce constraints based on vehicle configuration. For example, a linear configuration constraint enforcing identical front wheel drive forces can be expressed as

$$\begin{bmatrix} 1 & 0 & -1 & 0 & 0 & 0 \end{bmatrix} \tilde{\boldsymbol{f}} = 0 \tag{5.5.16}$$

where the linear equality equation is expressed as a row of the $\mathbf{G}$ matrix and the associated entry in the $\boldsymbol{d}$ vector. The search problem expressed in Equation 5.5.15 requires that the required motions be obtained, such that basic geometric and limiting constraints are met. In certain cases, this can lead to an under-constrained search problem that requires additional objectives to account for additional degrees of freedom. The additional objectives can be defined using an additional objective vector within the least-squares minimization problem, as proposed by Jonasson [38]. This idea is used in the presented work, where the additional objectives are expressed within the linear least-square minimization problem as

$$\begin{aligned} \min_{\tilde{\boldsymbol{f}}} \ & \frac{1}{2} \left\| \mathbf{W} \left(\begin{bmatrix} \mathbf{E} \\ \mathbf{S}_\mathrm{o} \end{bmatrix} \tilde{\boldsymbol{f}} - \begin{bmatrix} \boldsymbol{F} - \mathbf{E}\hat{\boldsymbol{f}} \\ \boldsymbol{s}_\mathrm{o} - \mathbf{S}_\mathrm{o}\hat{\boldsymbol{f}} \end{bmatrix} \right) \right\|_2^2 \\ \text{s.t. } & \mathbf{G}\tilde{\boldsymbol{f}} = \boldsymbol{d} \\ \text{and } & \tilde{\boldsymbol{f}}_{min} \leq \tilde{\boldsymbol{f}} \leq \tilde{\boldsymbol{f}}_{max} \end{aligned} \tag{5.5.17}$$

where $\boldsymbol{s}_\mathrm{o}$ is a vector of additional objectives, and the control and tire forces are related to the additional objectives with the transformation matrix $\mathbf{S}_\mathrm{o}$. This general formulation allows for any number of additional objectives to be enforced on the system, with appropriate weighting factors.

5.5.5 Additional Objectives

Additional objectives that eliminate under-constrained degrees of freedom within the least-squares search can be used to improve the allocation reliability, reduce the allocation search time, and minimize the control effort. As detailed by Kato, the dynamic square analysis produces an envelope defining the operational limits of the vehicle, in the presence of longitudinal and lateral load and torque transfer [40]. In the current research the dynamic square was utilized to define additional search criteria, as the analysis tool can be used to express a multitude of control torque distribution cases, including; pure acceleration, pure braking and combined driving and braking cases. As an example the dynamic square can be utilized to determine the front-to-rear drive and brake force distribution that maximizes the lateral handling capability of the vehicle in both acceleration and braking cases. A dynamic square analysis was conducted for the detailed BMW 330i at 70 km/h, yielding the dynamic square given in Figure 5.9. In this figure the handling limits of the vehicle under longitudinal acceleration are shown using iso-lines, and the torque distribution giving maximum combined acceleration is illustrated by the dotted line, while the dashed line represents a 50:50 front-to-rear torque split. It can be seen that the desired torque distribution presented is rearward biased, and is dependent on vehicle configuration and design parameters.

The desired front-to-rear drive force distribution determined is similar to that of the optimal distribution found from the straight line braking analysis discussed in Chapter 2; however, the current analysis can account for lateral load transfer, suspension, nonlinear tire, and drivetrain effects. Considering the axle force distribution in the first and third quadrants an additional objective in the least-squares minimization can be expressed as

$$\boldsymbol{s}_{\mathrm{o}} = \boldsymbol{f}_{\mathrm{dsm}}(a_{\mathrm{x}}) \tag{5.5.18}$$

where $\boldsymbol{f}_{\mathrm{dsm}}$ is a vector of objective forces with respect to the longitudinal acceleration a_{x}. In the given configuration, the dynamic square objective forces can then be related to the tire forces with

$$\mathbf{S}_{\mathrm{o}} = \begin{bmatrix} 1 & 0 & 0 & 0 & 0 & 0 \\ 0 & 0 & 1 & 0 & 0 & 0 \\ 0 & 0 & 0 & 0 & 1 & 0 \\ 0 & 0 & 0 & 0 & 0 & 1 \end{bmatrix} \tag{5.5.19}$$

where the transformation matrix $\mathbf{S}_{\mathrm{o}}$ considers only the longitudinal forces at the tire contact patches. Figure 5.9b can be developed illustrating the function of the desired front-to-rear force ratio with respect to longitudinal acceleration in the first and third quadrants of Figure 5.9a. In this case the rear axle will be the limiting case in the lateral acceleration capability of the vehicle, as the desired

case falls within the oversteer region of the dynamic square. It should be noted that other front-to-rear force distribution relationships can be determined such that the limiting condition exhibits an understeer, or more neutral steer condition by allocating more of the drive force to the front axle of the vehicle.

Control signals

The developed allocation algorithm determines the desired longitudinal and lateral forces at the individual tires. These forces must then be converted into appropriate control signals for the actuators. This can be accomplished with the use of quasi-static inverse relationships, where the required change in motor torque can be expressed as

$$\Delta\tau_i = k_\tau r_{\mathrm{e}} \tilde{f}_{\mathrm{x_i}} \tag{5.5.20}$$

where longitudinal tire force is related to the required motor torque by the motor transmission ratio k_τ and the effective radius of the tire r_{e}. Further, the required change in wheel steer angle can be expressed as

$$\Delta\delta_{\mathrm{f}_i} = \frac{\tilde{f}_{\mathrm{y}_i}}{c_{\alpha_i}} \tag{5.5.21}$$

The allocated control forces are now expressed in the form of actuator signals.

Control Allocation Examples

To illustrate the capabilities of the developed control allocation algorithm, a set of benchmark examples are presented. In these examples, the ability of the control allocation algorithm to achieve an arbitrary set of desired global control forces is evaluated. In these cases, the required sensor input for the allocation algorithm is defined using the double lane change manoeuvre benchmarks presented in Section 5.5.3. The results of the example tests are shown in Figures 5.10 and 5.11. In the low lateral acceleration case, the desired control forces and moments are replicated quite well, as the required control forces stay within the allowable search region illustrated by the normalized control force. It can also be seen that the allocated longitudinal forces for each axle pair are centred around the dynamic square objective forces. Similarly, in the high lateral acceleration case, the control allocation algorithm is capable of generating the desired control forces and moment. However, a region of reduced fidelity can be seen from 1-3 seconds, where the forces on the rear tires have reached limiting values. This reduces the ability of the allocation algorithm to achieve the desired control forces.

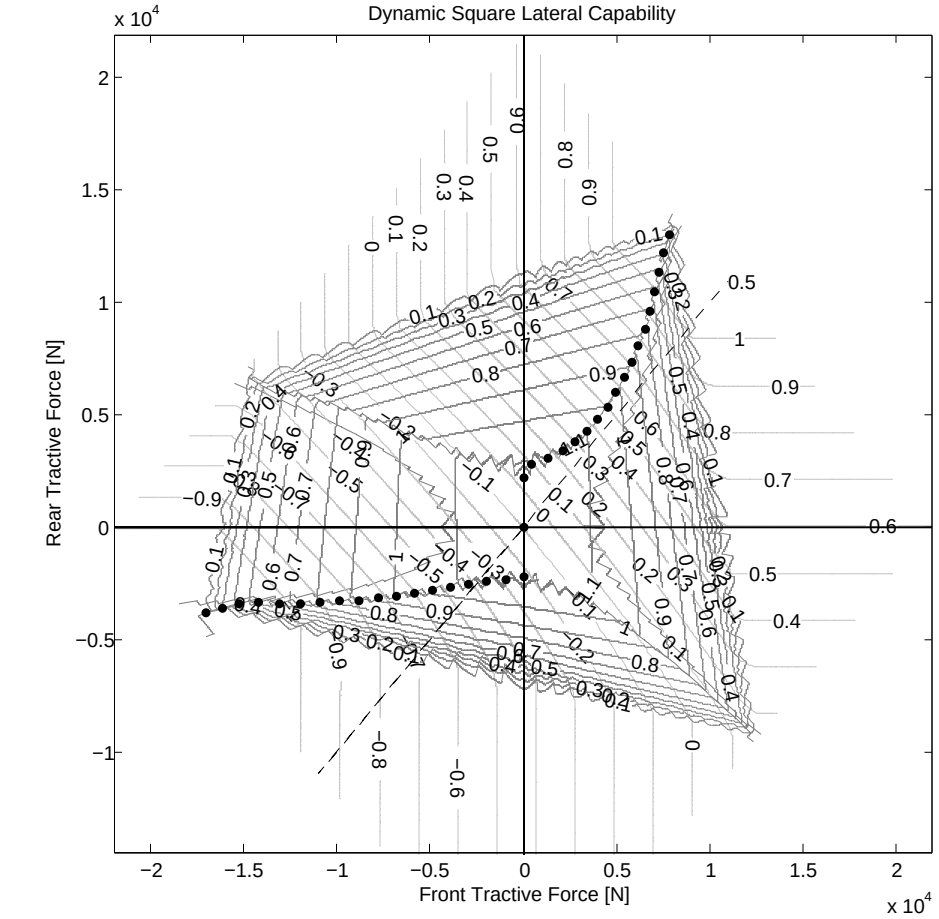

(a)

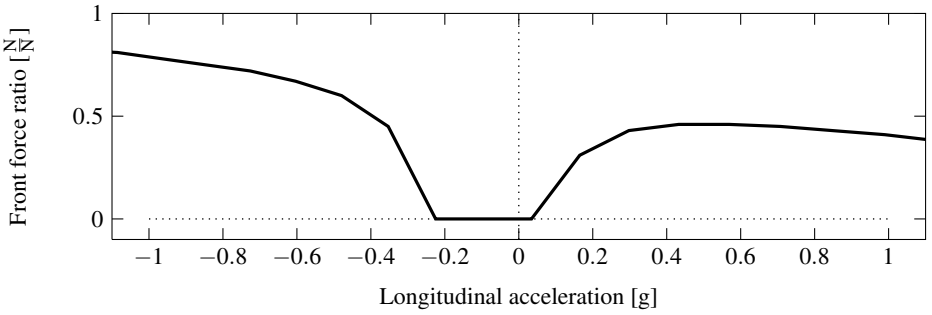

(b)

Figure 5.9: *BMW 330i dynamic square: nominal configuration @ 70 km/h.* (a) presents the dynamic square for the 2006 BMW 330i in the forward CG configuration using a two track vehicle model with roll-stiffness and nonlinear tire properties, illustrating the longitudinal and lateral capabilities of the vehicle with different front-to-rear drive and braking force distribution. The front-to-rear drive ratio providing maximum combined acceleration (dots) can be expressed as a function of longitudinal acceleration (b).

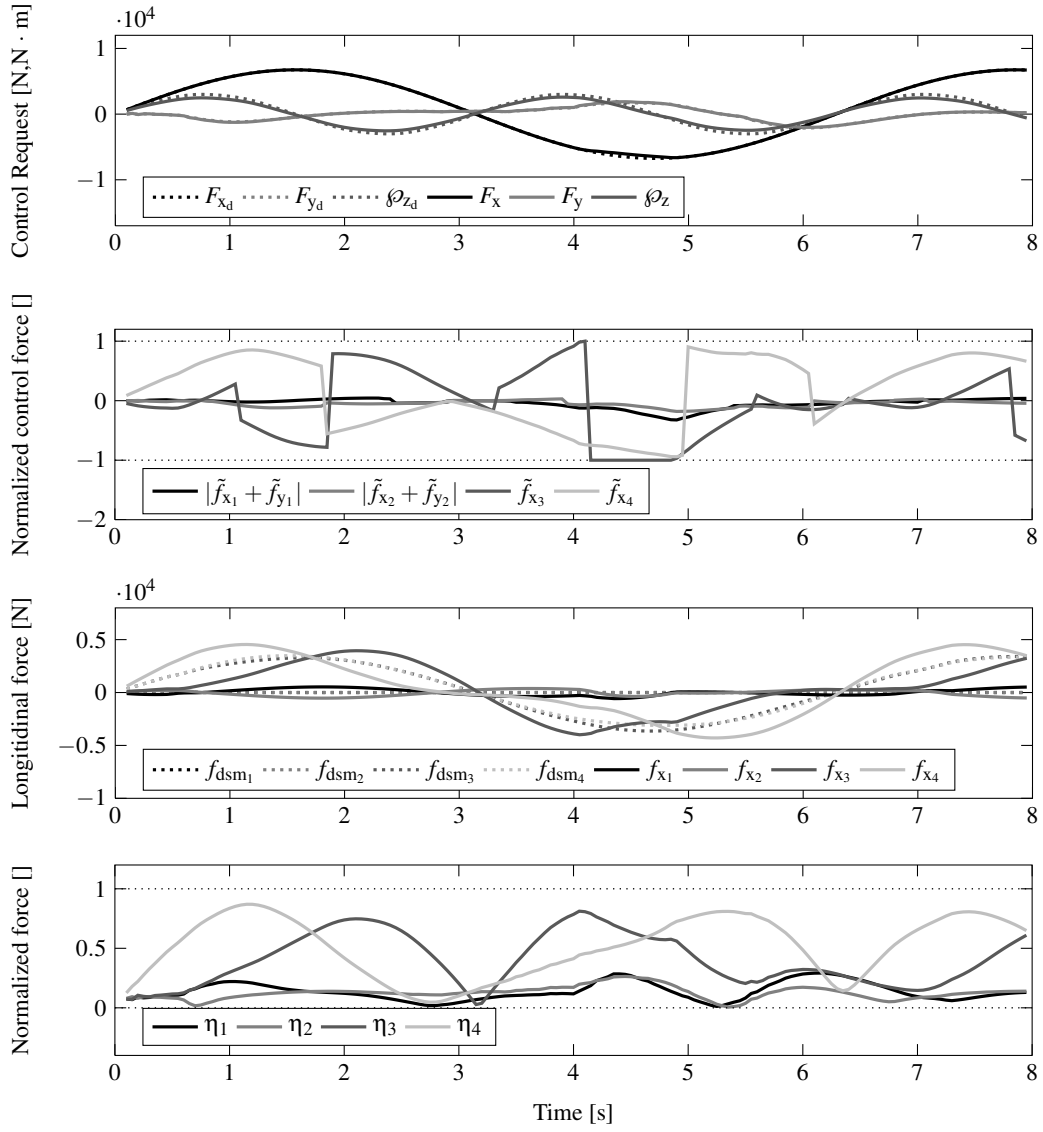

Figure 5.10: *Control allocation for double-lane change: low lateral acceleration test.* This figure illustrates the control force allocation for the low lateral acceleration double lane change case presented in Section 5.5.3. In the first plot, the dashed lines indicate the desired global control forces, the solid lines represent the control forces achieved using the detailed LLSM algorithm. In the current case, the allocation algorithm is capable of reproducing the desired control forces.

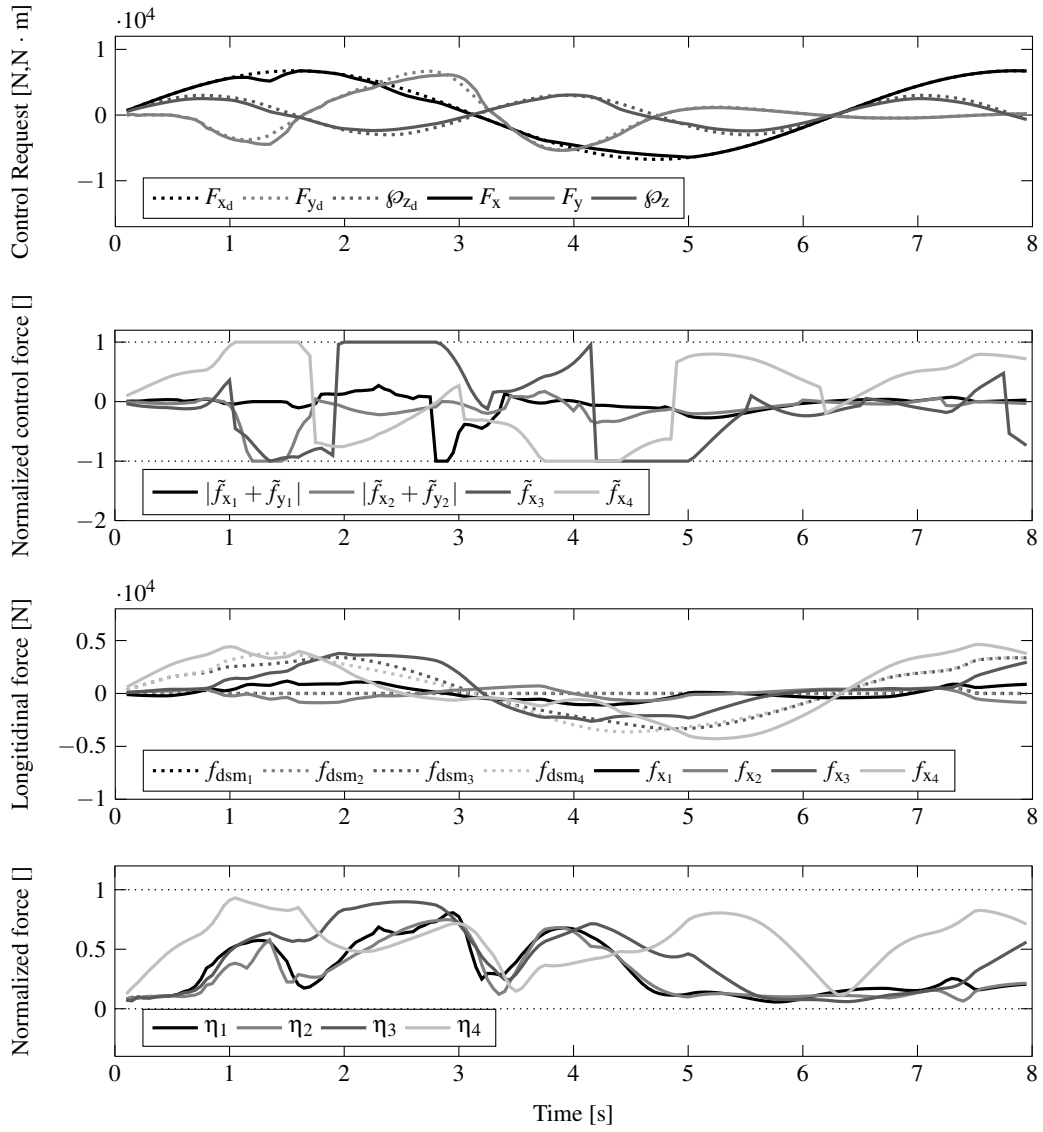

Figure 5.11: *Control allocation for double-lane change high lateral acceleration test.* This figure illustrates the control force allocation for the high lateral acceleration double lane change case presented in Section 5.5.3. In the first plot, the dashed lines indicate the desired global control forces, the solid lines represent the control forces achieved using the detailed LLSM algorithm. In the current case, the correlation between the desired and achieved control forces is reduced in the range of 1-3 seconds where a saturation condition is reached on the rear tires.

5.6 Summary

This chapter detailed the development of hierarchical control strategies for direct yaw moment control, with application to a hybrid electric vehicle within the scope of the research objectives.

First, the open-loop response of the proposed vehicle to steer and direct yaw moment inputs were evaluated and presented indicating the benefits and limits of direct yaw moment control for yaw rate and side slip velocity modulation. It was shown that the nonlinear response remains quite linear in the presented example over the intended operational speed range when compared to that of the driver steer input.

Subsequently, a hierarchical control structure was proposed composed of driver interpretation, control determination and control allocation blocks. Linear and nonlinear control schemes were presented and evaluated. The automatic generation of the linear quadratic regulator and state observers using EoM were presented and implemented in software.

Finally, an indirect control allocation algorithm for over-actuated systems was developed and demonstrated. The posed force based allocation problem was solved using a constrained linear least-squares minimization approach, considering tire and actuator limitations. An additional set of objectives were proposed using a dynamic front-to-rear torque distribution determined using the dynamic square method. The developed control allocation routine was then shown to be effective in allocating control signals within test cases.

Chapter 6

Software Implementation

This chapter presents the synthesis and implementation of the methods presented in the preceding chapters, leading to the development of a closed-loop model of the human operated vehicle system.

6.1 System Model

The complete human operated vehicle system shares the generalized structure given in Figure 2.1, with driver, vehicle dynamics management, and vehicle subsystems communicating both feed-forward and feedback signals. In practice, it can be very difficult to evaluate the interactions between these systems, due to nonlinearities in the vehicle and nondeterministic driver responses. The use of software based models can mitigate these problems, allowing for controlled experiments to be completed. To evaluate the effect of direct yaw moment control on the human operated vehicle system, a software based model was developed. Within this model the system dynamics were represented by:

- driver model - non-linear hybrid model with model predictive lateral control and finite state machine longitudinal control
- vehicle dynamics controller - hierarchical control consisting of a LQR control law with a constrained linear least squares minimization allocation algorithm
- vehicle model - fully nonlinear CarSim® model of 2006 BMW 330i

6.2 Co-simulation

Most systems are multi-domain and difficult to model accurately using a single piece of software. In practice, these multi-domain systems can be broken into a set of subsystems represented by specialized hardware or software models. The resulting co-simulation of various subsystem models allows

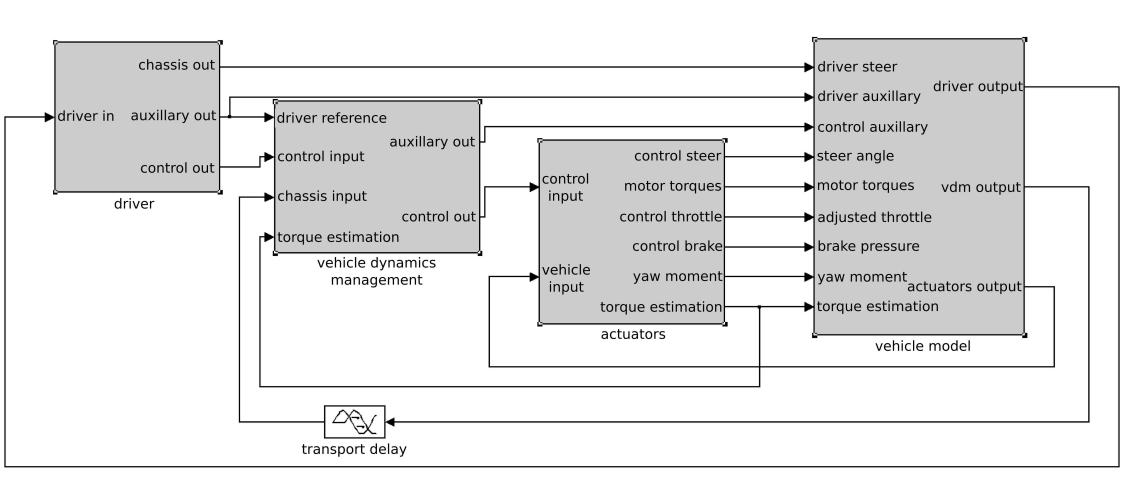

Figure 6.1: *Co-simulation model block diagram.* The figure presents the top level block diagram for the developed co-simulation model involving MATLAB®, Simulink® and CarSim®. The driver, vehicle dynamics management, actuator and vehicle systems blocks can be seen.

the response of the complete system and the interactions between the subsystems to be evaluated within a controlled environment.

The co-simulation model was achieved through the integration of MATLAB/Simulink® and CarSim®. This integration allowed the dynamics of the vehicle to be accurately predicted using the previously presented fully nonlinear BMW 330i vehicle model in CarSim®. The driver and control subsystems were modelled in MATLAB/Simulink®. The interfacing between the individual model components was completed in Simulink, with the top level block diagram shown in Figure 6.1. The specific implementations of these subsystems are discussed in the following sections.

6.2.1 Vehicle Model

Previous studies conducted by the author [19, 71] like those presented in Section 5.5.1 involved the use of an eight degree of freedom Equivalent Roll Stiffness (ERS) model to represent the dynamic response of the vehicle. To increase the fidelity of the implementation detailed in this chapter, a CarSim® model was used to represent the dynamics of the vehicle. The embedded CarSim® solver integrates vehicle states using a single step second-order Runge-Kutta algorithm (RK2). In

Table 6.1: *CarSim® model input variables*. An abbreviated list of the signals used by the CarSim® given by the purpose developed MATLAB/Simulink® models. The signals provided by the driver model (D), control determination (CD), control allocation (CA) and actuator models (A) are presented. Signals used only for display and validation purposes excluded.

Number	Name	Description	Provided by
1	IMP_STEER_SW	driver steering wheel angle	D
2	IMP_STEER_L1	left front steering control angle	CD,CA,A
3	IMP_STEER_R1	right front steering control angle	CD,CA,A
4	IMP_MY_L1	front left drive axle torque	CA,A
5	IMP_MY_R1	front right drive axle torque	CA,A
6	IMP_MY_L2	rear left drive axle torque	CA,A
7	IMP_MY_R2	rear right drive axle torque	CA,A
8	IMP_THROTTLE_ENGINE	IC engine throttle	CA
9	IMP_PCON_BK	brake cylinder pressure	CA

the model states are integrated forward in time as

$$\begin{aligned} k_1 &= \left.\frac{dq(t)}{dt}\right|_t \\ q^*(t+\frac{t_s}{2}) &= q(t)+k_1\frac{t_s}{2} \\ k_2 &= \left.\frac{dq^*(t)}{dt}\right|_{t+\frac{t_s}{2}} \\ q(t+t_s) &= q(t)+k_2 t_s \end{aligned} \tag{6.2.1}$$

where $q(t)$ is the current state, q^* is an Euler approximation of the state at the half step. The half-time step derivative k_2 is then used as the average derivative to solve for the state at the next full time step $q(t+t_s)$. In this integration method, the solver requires state information from the external subsystem models at the half and full time steps.

In the current research, the dynamics of the vehicle system were represented by the validated multibody CarSim® vehicle model presented in Chapter 2. The driver steer, throttle and brake inputs, as well as the electric motor torques modelled outside of CarSim® were specified as inputs to the model, as in Table 6.1. The required sensors were defined as outputs from the model and linked to the Simulink model components, as detailed in Table 6.2.

Table 6.2: *CarSim® model export variables*. An abbreviated list of the signals used by the purpose developed MATLAB/Simulink® models provided by CarSim®. The signals provided to the driver model (D), driver intent (DI), control determination (CD), control allocation (CA) and actuator model (A) blocks are presented. Signals used only for display and validation purposes excluded.

Number	Name	Description	Used by
1	Station	distance travelled in longitudinal direction	D
2	Xo	global position	D
3	Yo	global position	D
4	Yaw	heading angle	D
5	Steer_SW	steering wheel angle	D
6	Vx	longitudinal speed in vehicle frame	D,DI,CD,CA
7	AVz	vehicle yaw rate	D,DI,CD,CA
8	Vy	lateral speed in vehicle frame	D
9	Ay	lateral acceleration of vehicle	CA
10	Ax	longitudinal acceleration of vehicle	CA
11	MuX_L1	front left friction coefficient	CA
12	MuX_R1	front right friction coefficient	CA
13	MuX_L2	rear left friction coefficient	CA
14	MuX_R2	rear right friction coefficient	CA

6.2.2 Driver Model

The proposed hybrid driver model was implemented in MATLAB® m-code. This allowed for the use of pre-defined mathematics and visualization routines. Both the longitudinal and lateral components of the driver model were evaluated as discrete events. The steering wheel inputs determined by the lateral driver model were determined. The future vehicle positions used to determine the lateral path error were determined by numerical integration using the `lsim` function. The finite state machine longitudinal model was also implemented in MATLAB®.

6.2.3 Vehicle Dynamics Controller

The vehicle dynamics controller was comprised of computer implementations of the gain scheduled tracking model, LQR control and indirect allocation method in Simulink®, as shown in Figure 6.2. The gain scheduling driver interpretation and control determination gains were implemented using look-up tables with linear interpolation, defined using values obtained from the developed two DOF EoM models. The solution to the constrained linear least squares minimization allocation problem expressed in Equation 5.5.15 was achieved using the `lsqlin` function from the MATLAB® Optimization Toolbox. In the case of only upper and lower bounds the chosen algorithm uses a trust-region method that iteratively solves the minimization problem, solutions are refined within a trusted subset or neighbourhood about the current solution until convergence is reached. Alternatively, in the case of linear inequalities or equalities a quadratic programming method is used to refine an initial feasible solution using a projection method, determining a feasible set of points that converge to the solution. More information regarding these optimization techniques can be found in [30].

6.2.4 Actuators

Dynamic models of the active steering and electric motor control effectors were included and programmed in Simulink® as shown in Figures 6.3 and 6.4. The dynamics of the DC electric motors can be expressed as

$$\begin{Bmatrix} \dot{i}_{\mathrm{a}} \\ \dot{\omega} \end{Bmatrix} = \begin{bmatrix} -\dfrac{r_{\mathrm{a}}}{l_{\mathrm{a}}} & \dfrac{k_{\mathrm{b}}}{l_{\mathrm{a}}} \\ \dfrac{k_{\mathrm{t}}}{i_{\mathrm{m}}} & -\dfrac{k_{\mathrm{f}}}{i_{\mathrm{m}}} \end{bmatrix} \begin{Bmatrix} i \\ \omega \end{Bmatrix} + \begin{bmatrix} \dfrac{1}{l_{\mathrm{e}}} & 0 \\ 0 & 1 \end{bmatrix} \begin{Bmatrix} v_{\mathrm{a}} \\ \tau_{\mathrm{l}} \end{Bmatrix} \tag{6.2.2}$$

where i_{a} and $\dot{\omega}$ are the armature current and motor rotational speed respectively. System inputs include the applied voltage v_{a} and the load τ_{l}. The armature resistance and inductance are given as r_{a} and l_{a}. The motor rotational inertia is i_{m}, and k_{b}, k_{f} and k_{t} are armature and motor constants.

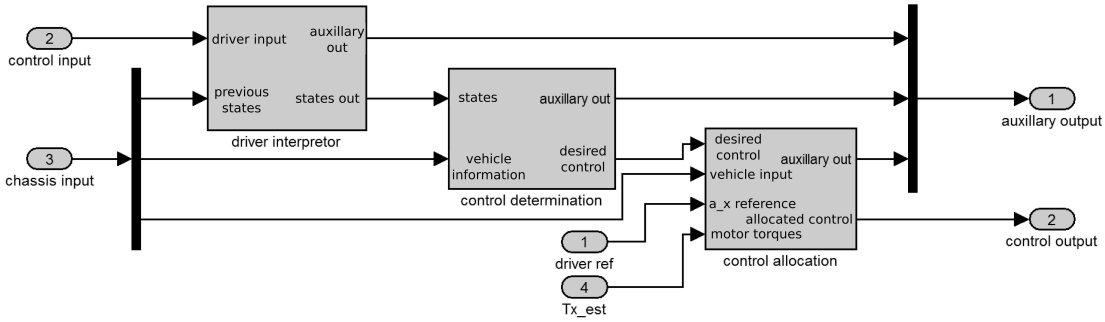

Figure 6.2: *Vehicle dynamics control block diagram.* The vehicle dynamics control was comprised of a driver interpretation, control determination and control allocation blocks.

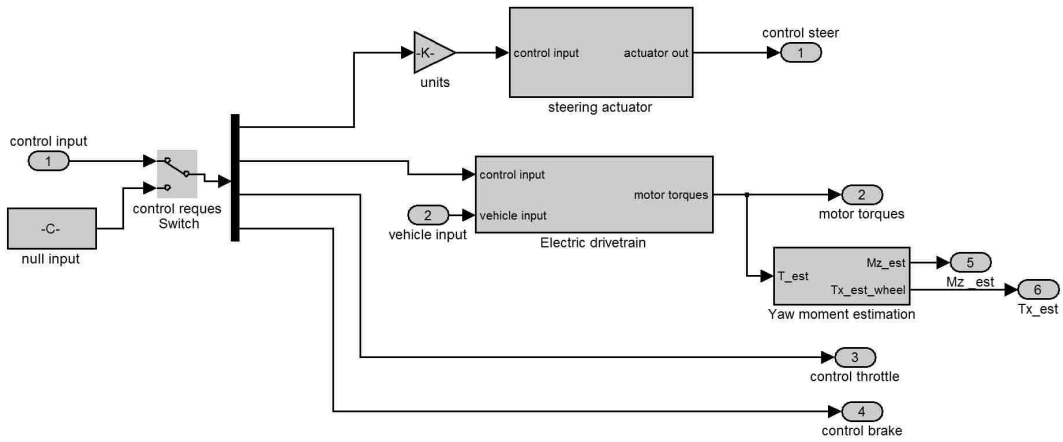

Figure 6.3: *Actuator block diagram.* In the presented case the actuator block was comprised of an active steering actuator and electric drivetrain components.

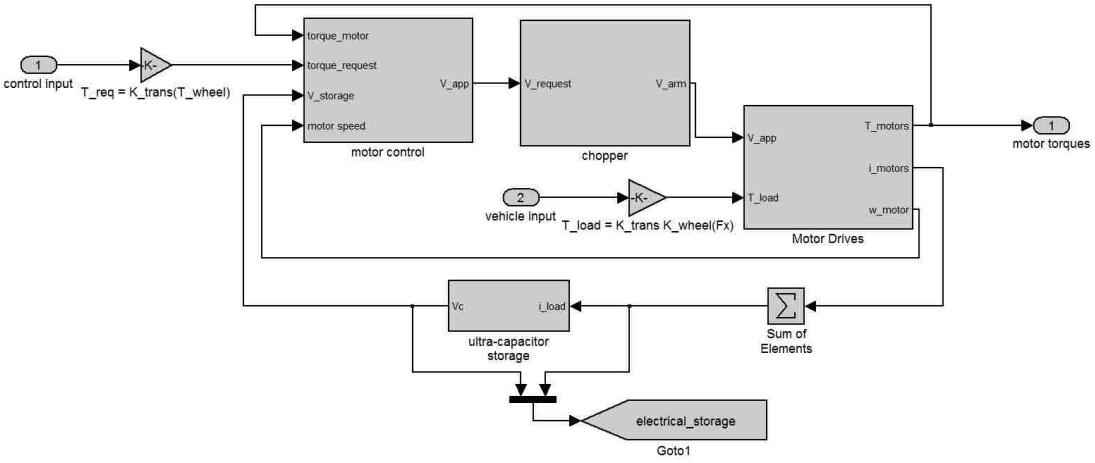

Figure 6.4: *Electric powertrain block diagram.*

Chapter 7

Results

This chapter presents results of numerical simulations using the software implementation presented in Chapter 6. This implementation makes use of vehicle models presented in Chapter 3, the driver models presented in Chapter 4, and the control techniques developed in Chapter 5. The simulated responses of the system under a number of test conditions are detailed. To keep the results to a reasonable breadth, the simulations discussed are limited in scope, as outlined in Table 7.1. First, the responses of a controlled and uncontrolled vehicle are compared with identical open-loop steer inputs. Second, the responses of various controlled and uncontrolled vehicles are presented in the presence of an active driver model.

7.1 Open-loop Driver Input

To evaluate the response of the yaw moment control to open-loop driver steer input, a series of simulations without the driver model are performed. In these simulations, identical steer inputs are given to an uncontrolled and controlled vehicle. In these cases, the integrated steer and yaw moment control is attempting to track a reference vehicle with a neutral steering characteristic. The control requires feedback information regarding the yaw rate and lateral velocity of the vehicle. In these cases, it is assumed that the yaw rate, as well as longitudinal and lateral acceleration, can be directly measured, and the lateral velocity is observed using a linear observer. The response of the controlled vehicle is compared to that of the reference signals and the response of the uncontrolled vehicle.

7.1.1 Case 1: Step Steer Input

In the first case, the steady-state cornering response of the vehicle configurations is evaluated with a step steer input of 50 degrees in a coast down test, with an initial forward speed of 50 km/h. The first set of LQR penalties presented in Table 5.1 are used, and lateral torque vectoring was only

Table 7.1: *Simulated test cases*. This table presents the series of open-loop (OL) and closed-loop (CL) simulated test cases presented, making use of the developed models for the nominal (N) and forward CG (F) vehicle configurations. In the closed-loop cases, the driver attempts to follow either a double lane change (DLC1) or an emergency double lane change (DLC2) path. The LQR control gains (Table 5.1) and observed states are also detailed.

Case	Steer/Path	Type	Vehicle	Driver Internal	Driver Interpreter	LQR Gains	Observed States
1	step steer	OL	F	N	N	1	v
2	sine wave steer	OL	F	N	N	1	v
3	DLC1	CL	F	N	N	1	v
4	DLC2	CL	F	N	N	1	v
5	DLC2	CL	F	N	N	5	v
6	DLC2	CL	F	N	N	5	-
7	DLC2	CL	F	F	N	1	v
8	DLC2	CL	F	N	N	1	v
9	DLC2	CL	F	N	N	1	v

allowed across the rear axle with identical front wheel steer angles enforced. The ground plane responses of the controlled and uncontrolled vehicle are shown in Figure 7.1 and 7.3. The addition of the yaw moment control is shown to improve the yaw response during constant speed operation without additional driver steer input. The control marginally improves the yaw rate tracking of the understeering vehicle to that of a neutral steer vehicle as shown in Figure 7.2. The lateral slip velocity was reduced, approaching the lateral slip velocity of the reference vehicle. As the control is attempting to track both yaw rate and lateral slip velocity, reduced yaw rate tracking capability can be seen as the control attempts to minimize the error in slip velocity.

It can also be seen in Figure 7.2 that the motor torques switch from providing a negative to providing a positive yaw moment. The motor torques were shown to remain well below the rated 100 N·m torque limit of the motors. This can be attributed to the limited difference in handling characteristic between the actual and reference vehicle models with understeer gradients of 0.497 and 0.075 $^\circ/\mathrm{g}$ respectively. With a larger difference in understeer gradient, larger motor torques would be required as shown for the Chrysler Pacifica in Figure 5.4. An increase in rear tire usage can be seen in the normalized force plot due to the application of longitudinal forces applied to the rear wheels. A corresponding increase and decrease in tire usage can be seen on the inside and outside front tires given by η_1 and η_2 due to load transfer across the axle due to an increased lateral acceleration. It can be seen that no motor torque is applied to the front drive axles, as the drive and braking forces on the rear axle are symmetric, maintaining the desired longitudinal acceleration.

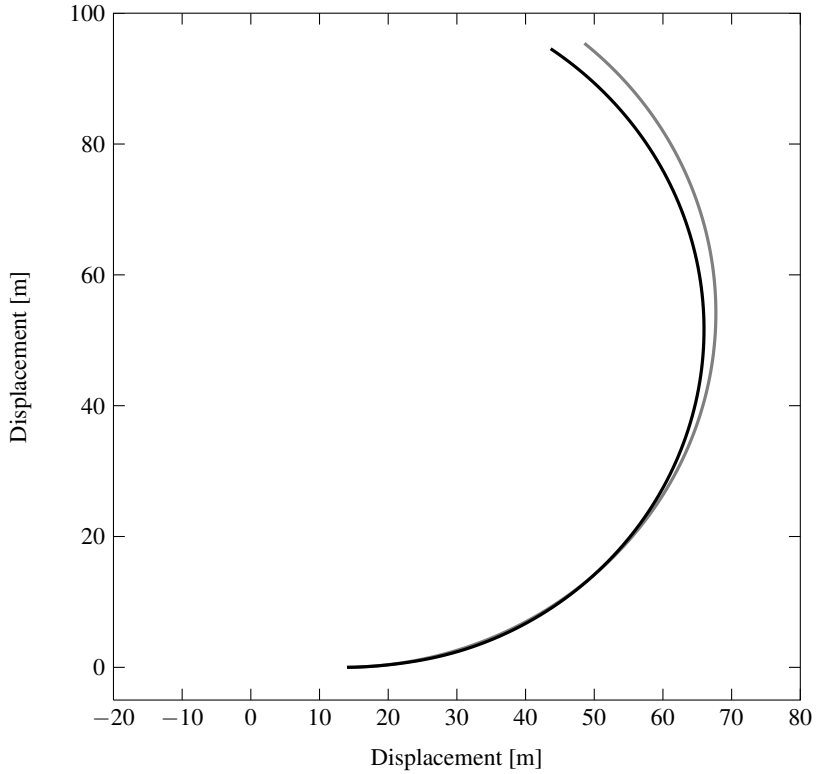

Figure 7.1: *Case 1: open-loop step steer input, ground plane response*. The figure presents the ground plane response of the controlled (black) and uncontrolled (gray) vehicles with identical 50 ° step steer inputs, with an initial forward speed of 50 km/h.

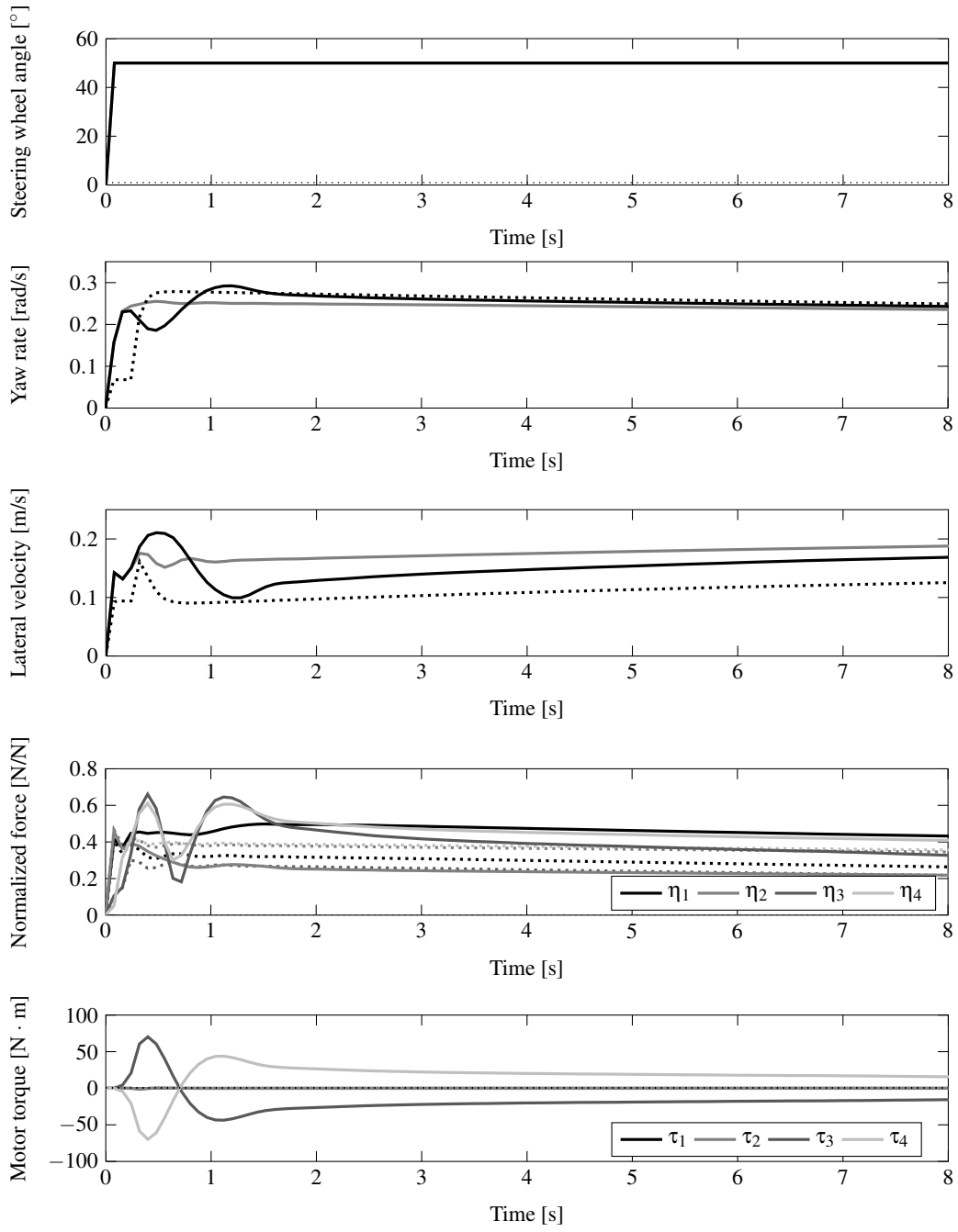

Figure 7.2: *Case 1: open-loop step steer input response*. This figure presents the response of the uncontrolled and controlled vehicle to a step steering wheel input of 50 degrees. The response of the uncontrolled vehicle is given in gray and controlled vehicle is given in black. The reference yaw rate and lateral velocity are given as dotted lines, along with the uncontrolled vehicle normalized tire force. Improved yaw rate tracking to the reference states can be seen with the application of the developed controls.

Figure 7.3: *Case 1: open-loop step steer input response, visualization.* This figure presents the response of the uncontrolled and controlled vehicle to an open-loop 50° step steering wheel input. It can be seen that the applied yaw moment across the rear axle of the controlled vehicle (black) improves cornering response without additional driver steer input.

7.1.2 Case 2: Sine Wave Steer Input

Next, the transient response of the control was evaluated with a sine wave steer input with a frequency of 2 rad/s and an amplitude of 50°, in the presence of a 1 m/s^2 longitudinal acceleration. In the simulated test, the initial speed of the vehicle was 50 km/h, and the first set of LQR penalties presented in Table 5.1 was used. The ground plane responses of the controlled and uncontrolled vehicle are shown in Figure 7.5 and 7.6. The addition of the yaw moment control was shown to increase the handling responsiveness of the vehicle without additional driver steer input. The control improves the yaw rate tracking of the understeering vehicle to that of a neutral steer vehicle as shown in Figure 7.4. As the vehicle speed increases, the difference between the desired and uncontrolled yaw rate becomes larger, as predicted by the understeer gradient. It is clear that the torque vectoring yaw moment control is capable of correcting the understeer characteristic of the vehicle. The lateral slip velocity was shown to change in the presence of the applied yaw moment, when compared to the uncontrolled case. Reduced yaw rate tracking capability can be seen when the deviation between the lateral slip velocity and the reference becomes large, as the control attempts to minimize the error in slip velocity. It should be noted that this effect can be modulated by changing the state penalty weightings, altering the importance of yaw rate and side slip error. Generally, an increase in rear tire usage can be seen, attributed to the increased longitudinal force generated by the requested motor torques to create the desired yaw moment. However, due to the asymmetric application of wheel torques, the inside rear wheel tire usage can be decreased when compared to the uncontrolled case. It can be seen that the motor torques on the front axle are identical and remain near zero, as enforced by the identical torque constraint in the allocation algorithm. The required drive torque to maintain the constant acceleration is applied to the rear axle, as enforced by the dynamic square objective. The motor torques across the rear axle are shown to be unequally distributed, with an offset due to the required drive torque for acceleration. To generate the required yaw moment and longitudinal acceleration the motor torques are mostly positive, but in conditions where a large yaw moment is required, braking torques are applied by the motors.

It can also be seen, that unlike brake based systems that can degrade longitudinal response to improve directional control, integrated steer and torque vectoring control can be used to simultaneously achieve the longitudinal, lateral and yaw moment requests of the driver.

7.1.3 Open-loop Summary

From the open-loop driver input trials, an improvement in vehicle response can be seen without additional driver steering wheel input. As expected the applied control forces have been shown to increase the tire usage, but remain below the saturation limit of the tires. The applied motor torques have also been shown to be well below the rated maximum of the drive motors. This can

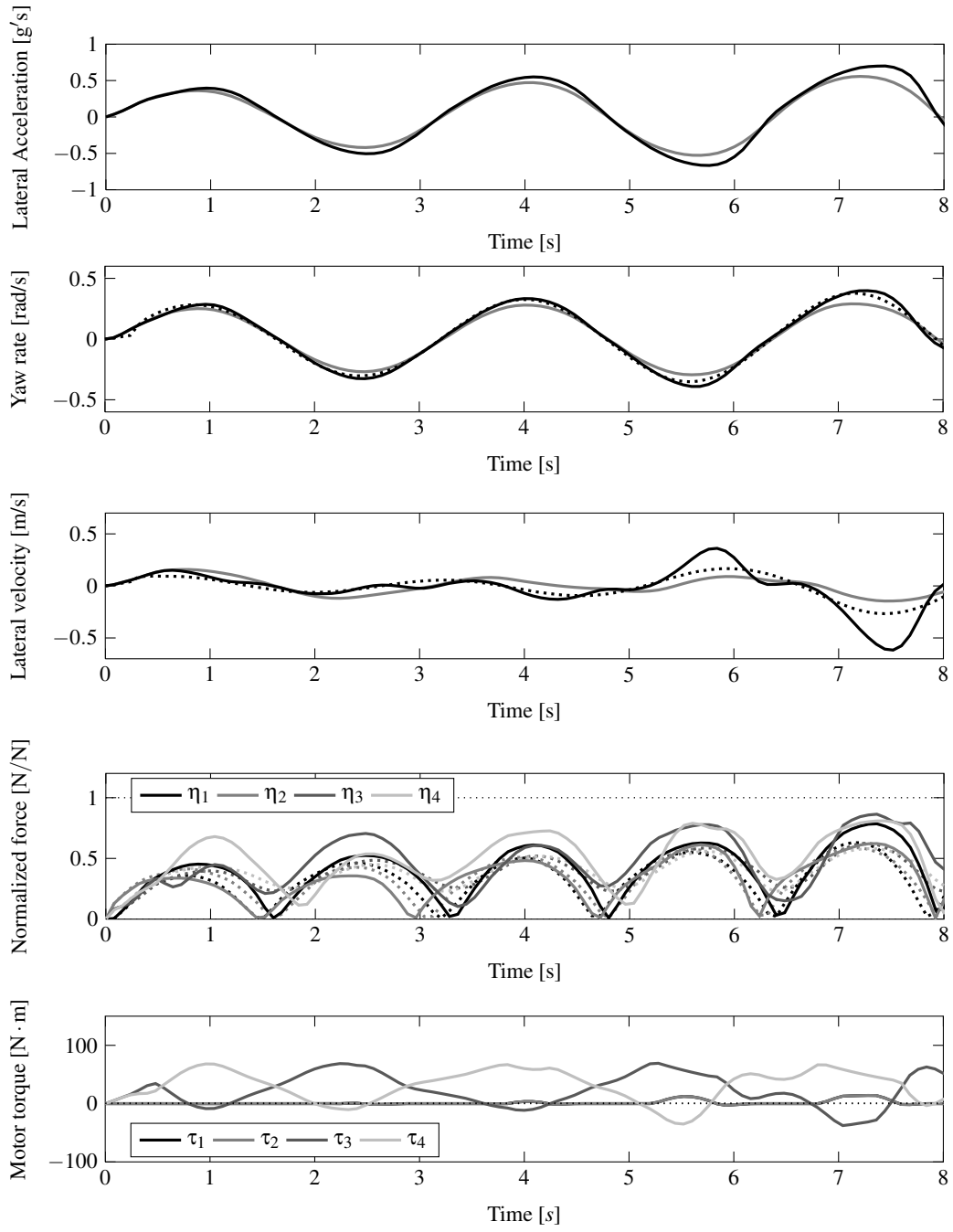

Figure 7.4: *Case 2: open-loop sine wave steer input, response*. This figure presents the response of the uncontrolled and controlled vehicles to a sine wave steer input with a frequency of 2 rad/s and an amplitude of 50°, under a longitudinal acceleration of 1 m/s^2. The controlled vehicle (black) is shown to have increased yaw rate tracking capabilities when compared to the uncontrolled case (gray). The lateral slip velocity is shown to deviate further from the reference state (dotted) as forward speed and tire use increases.

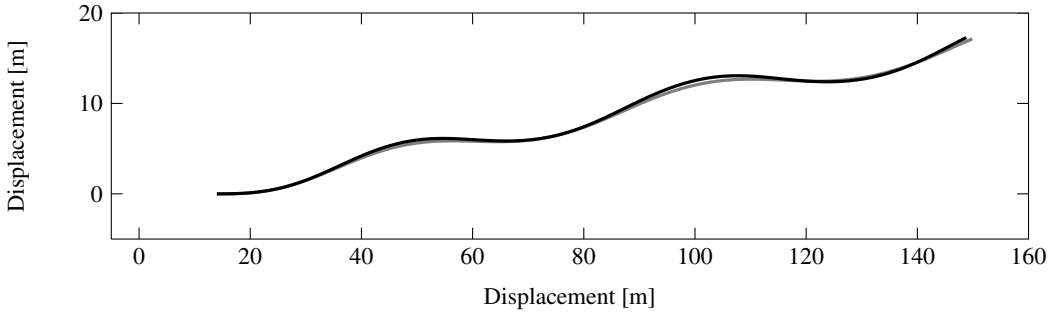

Figure 7.5: *Case 2: open-loop sine wave steer input, ground plane response*. The figure presents the ground plane response of the controlled (black) and uncontrolled (gray) vehicles with identical sine wave input with a frequency of 2 rad/s and an amplitude of 50°, under a 1 m/s^2 longitudinal acceleration.

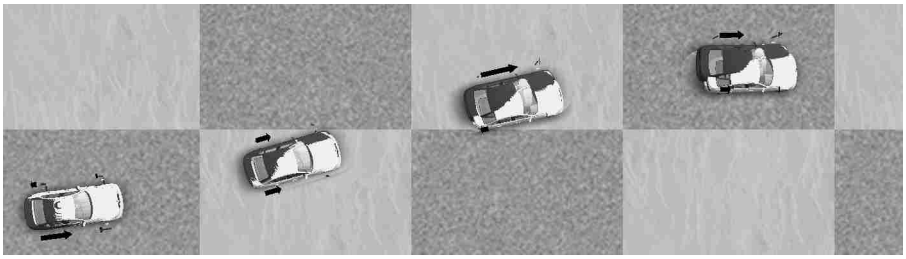

Figure 7.6: *Case 2: open-loop sine wave steer input, ground plane response visualization*. This figure illustrates the improved handling response of the controlled (black) vehicle, when compared to the uncontrolled case (white). The motor torques applied to the rear axle of the controlled vehicle are indicated by the black arrows.

be attributed to the small difference in handling characteristics between the actual and reference vehicles. Larger amounts of left-to-right torque biasing are necessary in cases where the variation between the actual and reference models is more significant, as in the Chrysler Pacifica case given in Chapter 5. The second test case indicates that the developed variable torque distribution yaw moment control can achieve both longitudinal demands and corrective yaw moments simultaneously, where conventional brake based systems degrade longitudinal performance to generate corrective yaw moments.

7.2 Closed-loop Driver Input

To evaluate the response of the closed-loop yaw moment control in the presence of an active driver, a series of simulations with the developed driver model are performed. A vehicle in the forward centre of gravity configuration exhibiting an understeer characteristic was simulated. As with the open-loop tests, reference control states were generated with a two DOF vehicle model in the nominal neutral steering configuration. The response of the controlled vehicle is compared to that of the reference signals and the response of the uncontrolled vehicle. Emergency situations are dominated by transient response, so a set of double lane change manoeuvres are presented to illustrate the abilities of the developed controls, and their effect on the human operated vehicle system.

7.2.1 Case 3: Double Lane Change

First, a simulation replicating a double lane change with low lateral acceleration was conducted. A longitudinal acceleration of 1 m/s^2 was applied to emulate a highway on ramp obstacle avoidance. The active driver model is attempting to follow a prescribed path with a maximum lateral offset of 3.5 meters. The steering wheel input and ground plane responses of the controlled and uncontrolled vehicle are shown in Figure 7.7 and 7.9. In the controlled case, it can be seen that the steering input of the driver is reduced, while the vehicle traverses a nearly identical path to that of the uncontrolled vehicle. The vehicle states throughout the simulated manoeuvre are presented in Figure 7.8, showing increased yaw rate and lateral velocity tracking. However, a region of decreased lateral velocity tracking can be seen starting at 5 seconds, caused by the application of a large yaw moment generated by driving and braking torques across the rear axle. As additional longitudinal force is applied to the rear tires, an increase in the vehicle slip angle is required to maintain the lateral force at the rear tires, as the rear tires can not be steered. It can be seen that the normalized tire force remains below the saturation limit, but approaches the nonlinear region of the rear tires at 5 seconds where larger longitudinal forces are applied. As expected, the required longitudinal drive force is allocated to both the front and rear axles, as imposed by the dynamic square objective. Additionally,

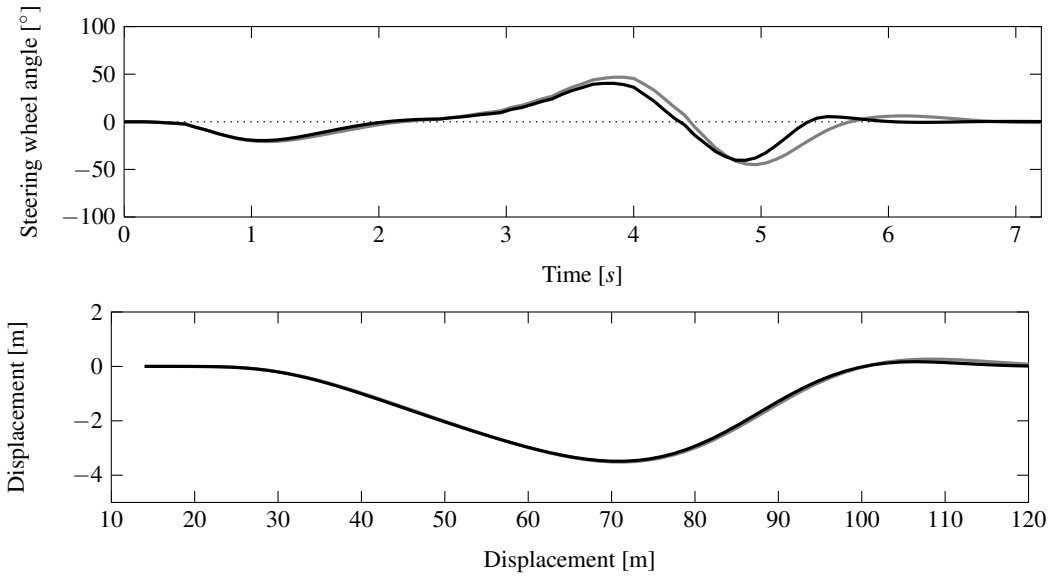

Figure 7.7: *Case 3: closed-loop double lane change, steering and ground plane response* . This figure presents the response of the uncontrolled and controlled vehicle during a double lane change manoeuvre experiencing maximum lateral acceleration of 0.5 g's. In the presented case, the vehicle is shown to traverse nearly an identical path, with reduced driver steer inputs.

a small increase in front drive torque is allocated to the front motors to maintain the longitudinal acceleration in the presence of the braking torque applied to the rear right wheel at 5 seconds.

7.2.2 Case 4: Emergency Double Lane Change

Next, a case with a similar but more demanding lateral avoidance manoeuvre is tested emulating that of the double lane change validation test conducted in Chapter 2. In this test, an initial forward velocity of 50 km/h was set, with zero longitudinal acceleration. The first set of LQR gains presented in Table 5.1 is utilized, tracking yaw rate and lateral slip velocity with both steering and yaw moment inputs. Figure 7.10 presents the steering wheel input and ground plane response of the vehicle. A small improvement in lateral response compared to the uncontrolled vehicle can be seen with a reduced lateral overshoot at 70 meters. This was achieved with a reduced driver steer input throughout the manoeuvre. The vehicle states throughout the manoeuvre are presented in Figure 7.12. This manoeuvre represents a near limit case with a maximum lateral acceleration of 0.75 g's obtained at approximately 3 seconds. Improved yaw rate tracking to the reference vehicle can be seen, with a reduction in lateral velocity from the uncontrolled case. It can be seen that the rear tires

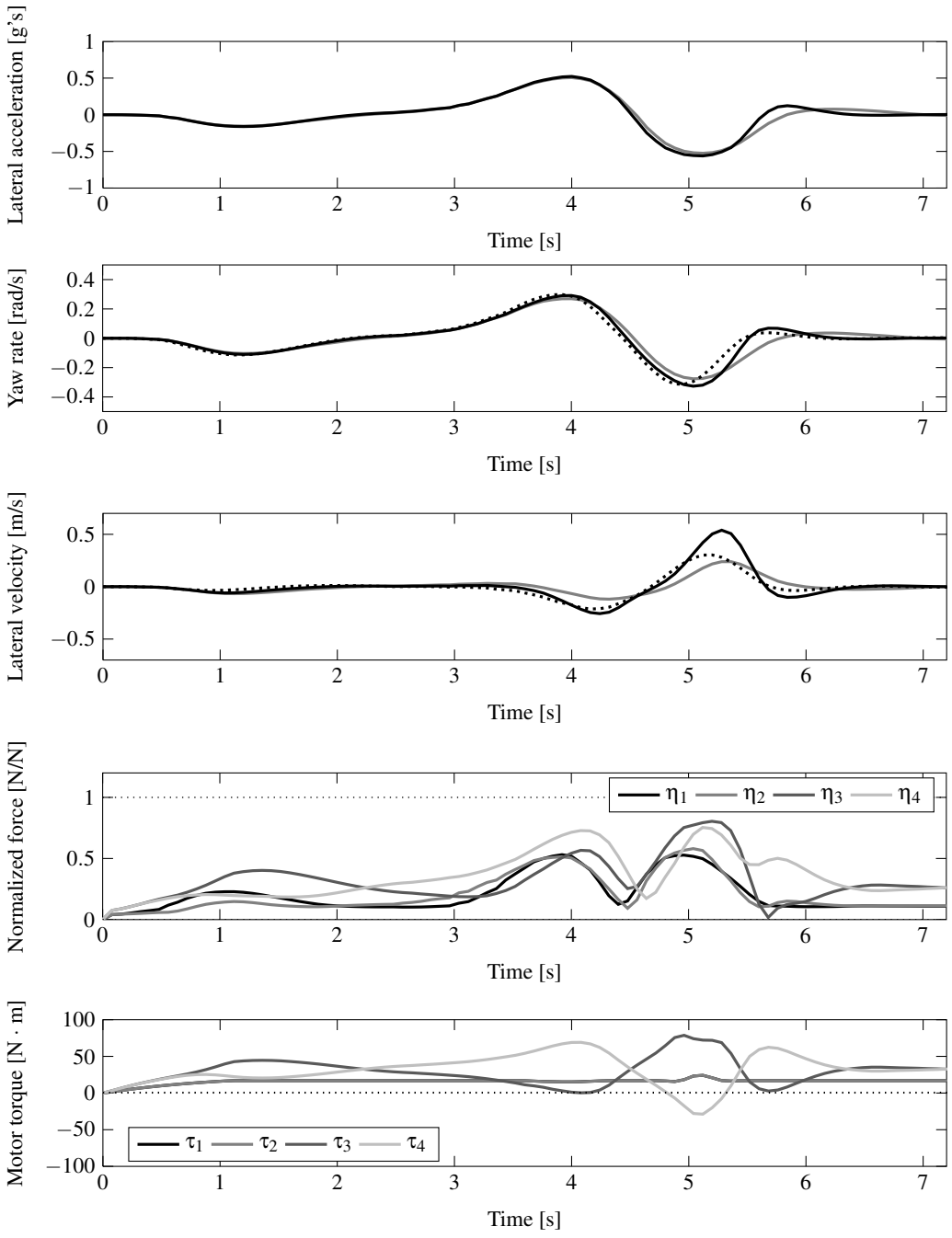

Figure 7.8: *Case 3: closed-loop double lane change response.* This figure presents the response of the uncontrolled and controlled vehicle during a double lane change manoeuvre experiencing maximum lateral acceleration of 0.5 g's. The controlled vehicle (black) is shown to have improved yaw rate and lateral velocity tracking to the desired states (dotted), when compared to the uncontrolled case (gray). However, a region of reduced tracking ability was observed at 5 seconds, associated with the generation of lateral forces at the non-steered rear axle.

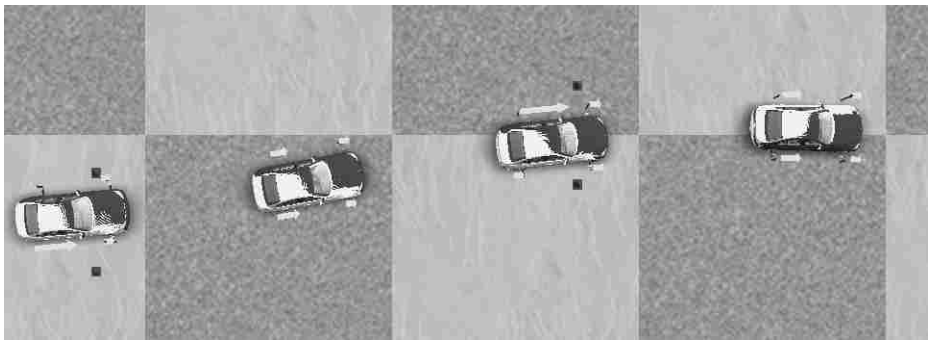

Figure 7.9: *Case 3: closed-loop double lane change, visualization*. This figure illustrates the handling response of the controlled (black) and uncontrolled (white) vehicles from 5-6.5 seconds. The dynamically allocated motor torques of the controlled vehicle are shown.

approach but do not cross the saturation limit. The applied rear axle motor torques are reasonably symmetric and remain below the maximum torque of the motors. A visualization of the responses of the controlled and uncontrolled vehicle can be seen in Figure 7.13.

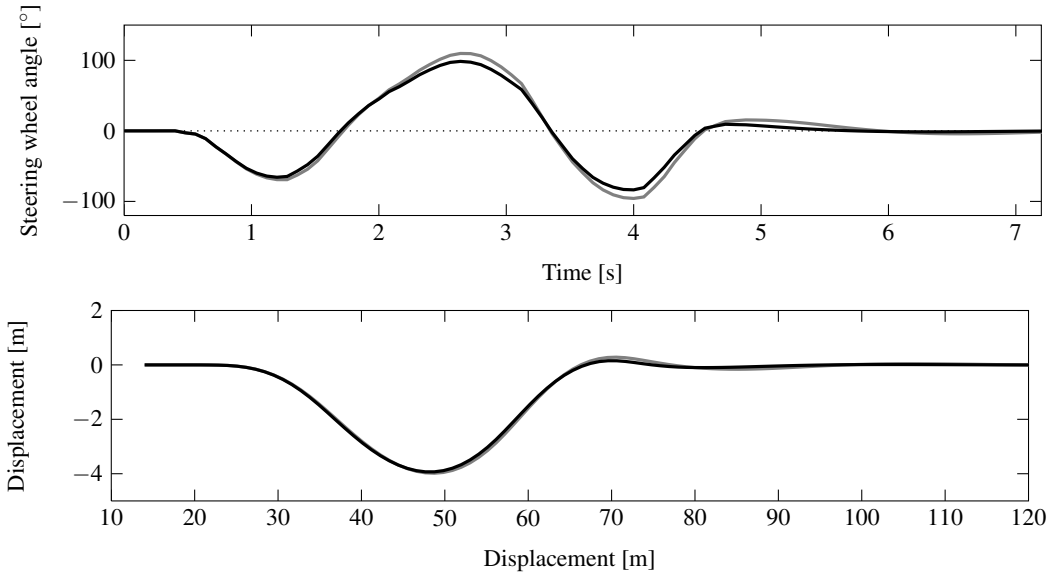

Figure 7.10: *Case 4: closed-loop emergency double lane change, ground plane response*. The figure presents the closed-loop driver steer input and ground plane response for an emergency double lane change manoeuvre.

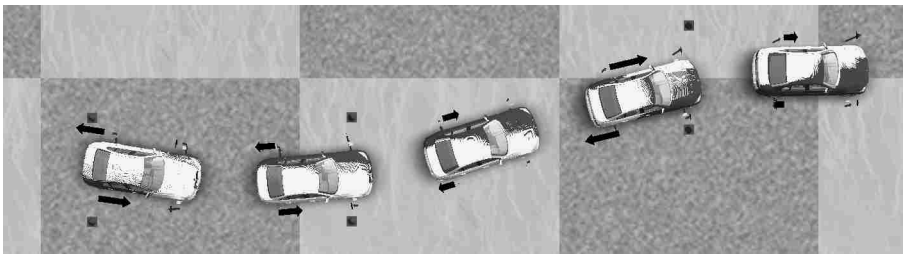

Figure 7.11: *Case 4: closed-loop emergency double lane change, visualization*. This figure illustrates the response of the controlled (black) and uncontrolled (white) vehicles during an emergency double lane change manoeuvre. The motor torques applied to the drive axles are represented by the black arrows.

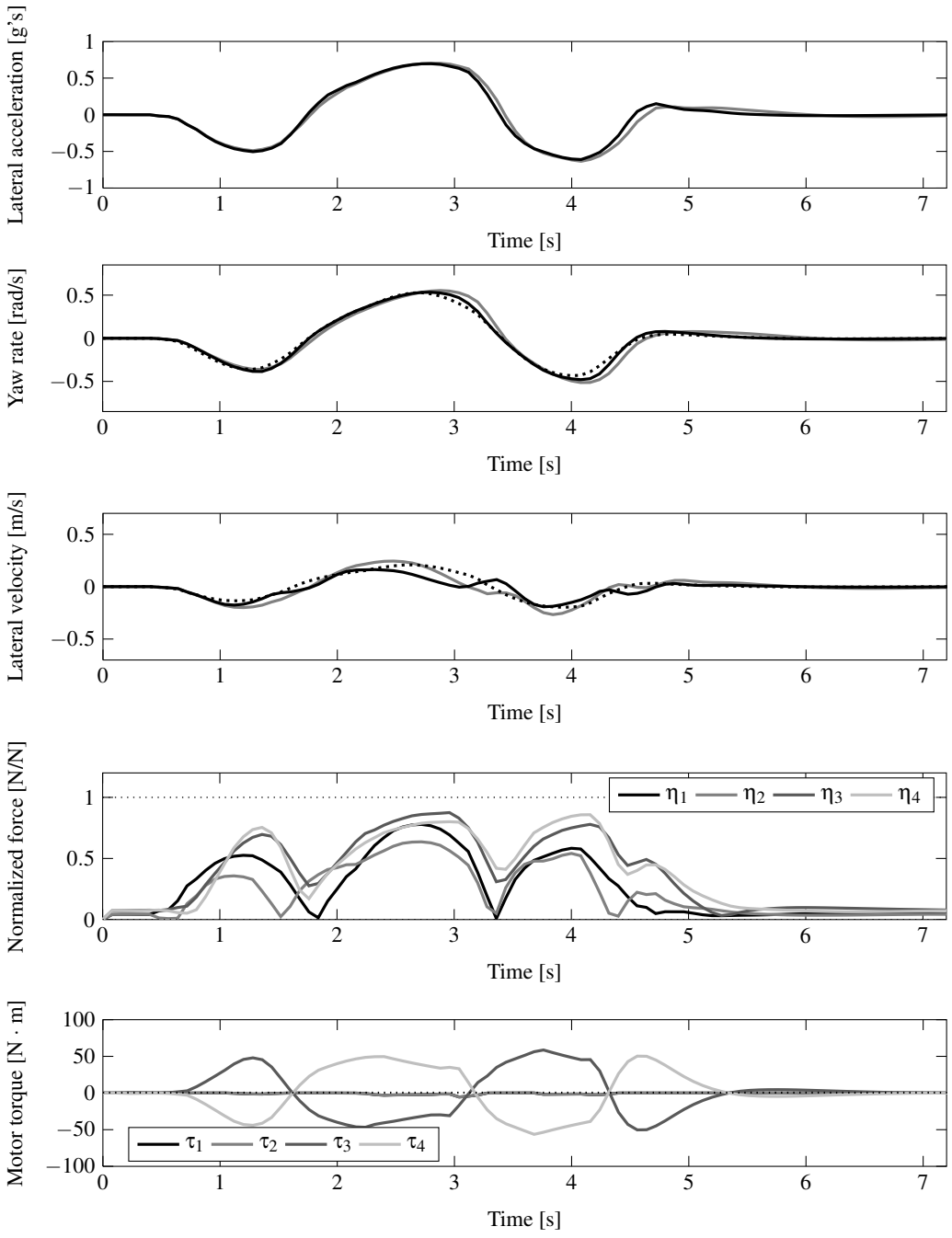

Figure 7.12: *Case 4: closed-loop emergency double lane change response*. This figure presents the response of the controlled (black) and uncontrolled (gray) vehicles during an emergency double lane change manoeuvre. The desired and observed states are given by the black and gray dotted lines respectively. Increased yaw rate and lateral velocity tracking can be seen. The applied motor torques and tire forces were shown to remain below saturation.

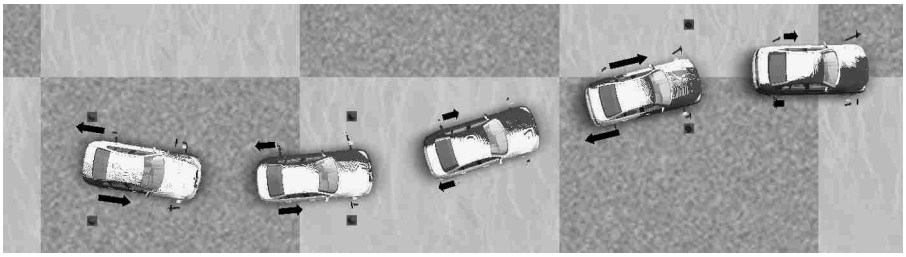

Figure 7.13: *Case 4: closed-loop emergency double lane change, visualization.* This figure illustrates the response of the controlled (black) and uncontrolled (white) vehicles during an emergency double lane change manoeuvre. The motor torques applied to the drive axles are represented by the black arrows.

7.2.3 Cases 5: Effect of Penalty Weightings

Using the previous test condition, an alternative set of LQR gains was tested, this time tracking only lateral side slip velocity. Figure 7.14 presents the response of the controlled vehicle when compared to that of the uncontrolled vehicle. It can be seen that the current LQR weightings improve the lateral slip velocity tracking to the reference vehicle from 1-2 and 4-6 seconds, but reduces the yaw rate tracking while reducing the driver steer input (not shown). However, the lateral velocity tracking is reduced between two and four seconds. Similar to the preceding case, the tire usage nears but does not cross the saturation limit. An increase in rear tire usage can be seen between four and five seconds when compared to the preceding case, as the control is following the desired lateral velocity with higher fidelity. The motor torques are also quite different but remain below the limit. The region of lower lateral velocity tracking can be attributed to the linear observer used. As shown, the observer estimate varies from that of the actual vehicle due to unmodelled nonlinearities. However, it can be seen that the observer estimate does predict the trends of the lateral side slip angle quite well, and generally over predicts the amount of side slip.

7.2.4 Case 6: Effect of Linear Observer

To quantify the effect of potential observer estimation error, a simulation was run with the lateral slip velocity as a measured quantity taken directly from the CarSim® model. The response of the vehicle is given in Figure 7.15. As expected, with no penalty weighting given to yaw rate, tracking is reduced. It can also be seen that in the current case, the driver steer input is increased when compared to the uncontrolled case. It can be seen that the lateral velocity tracking is improved, especially in the region from two to four seconds where the case with the linear observer failed to track the desired response. This can be attributed to state estimate errors obtained from the linear observer, in the presence of tire nonlinearities. This causes the relative error between the observed and reference states to be inaccurate, leading to control requests unable to track the desired lateral velocity. However, using the 'measured' lateral velocity from the CarSim® these problems are removed in the region from 2-4 seconds. This has a marked effect on the torque requests allocated to the motors within this region.

It has been shown that the state estimates obtained using the developed linear observer are sufficiently accurate in cases with low to mid level lateral accelerations, as shown in Figure 7.16. The previously discussed estimation error is evident in Figure 7.17, illustrating the linear observer response in a high lateral acceleration case. The automatically generated high gain linear observers developed have been shown to reject sensor measurement noise, but do not account for tire nonlinearities. However, in the cases presented, the observer estimate allowed for increased lateral slip velocity tracking at low lateral acceleration levels, while the error in the observer estimates at higher

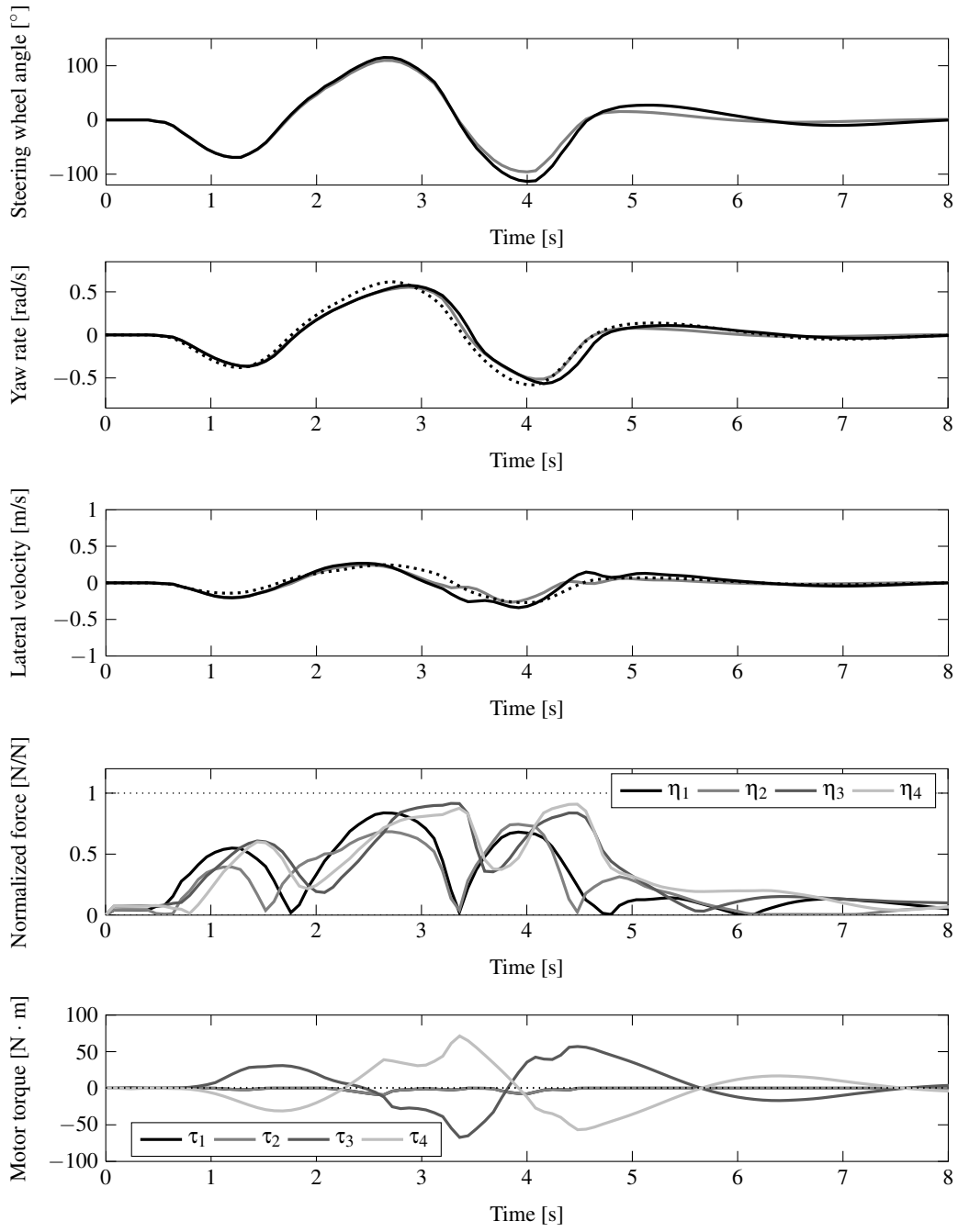

Figure 7.14: *Case 5: emergency double lane change response*. This figure illustrates the response of the controlled (black) and uncontrolled (gray) vehicles during an emergency double lane change manoeuvre. The desired and observed states are given by the black and gray dotted lines respectively. In the controlled case the only the observed lateral slip velocity is being tracked.

levels of lateral acceleration acted to reduce the lateral slip velocity. This could be of benefit as reducing the magnitude of the lateral slip velocity can reduce the onset of loss of control situations. However, further research into this would be required before any formal conclusions could be made. Alternatively, a gain scheduled linear observer or a nonlinear observer [42] could be used to provide more accurate estimates of lateral slip velocity.

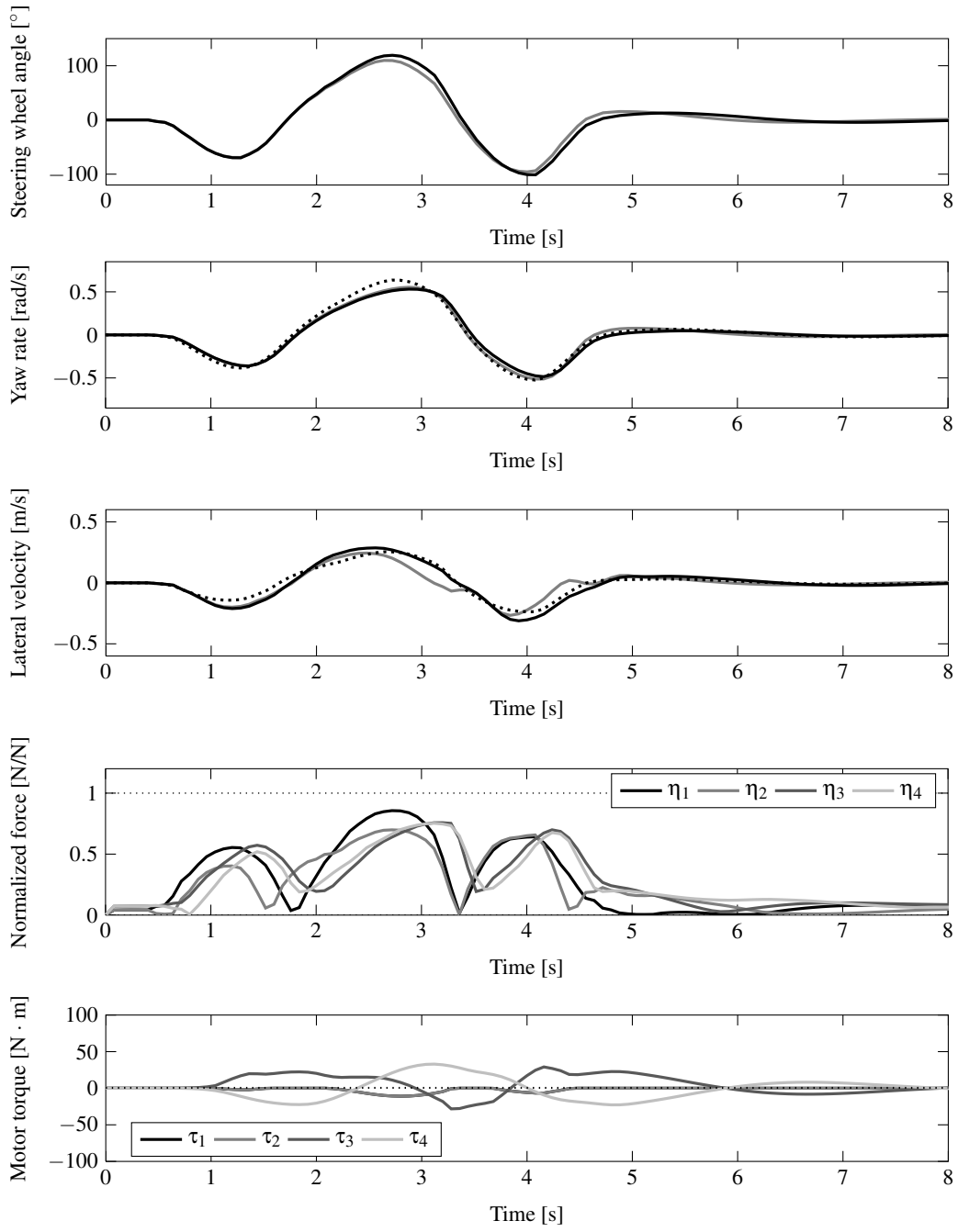

Figure 7.15: *Case 6: closed-loop emergency double lane change response, no observer.* This figure illustrates the case were the lateral slip velocity is directly measured, eliminating the linear observer from the simulation loop. It can be seen that an improvement in lateral slip velocity tracking can be seen when compared to Case 5, where lateral slip velocity is observed.

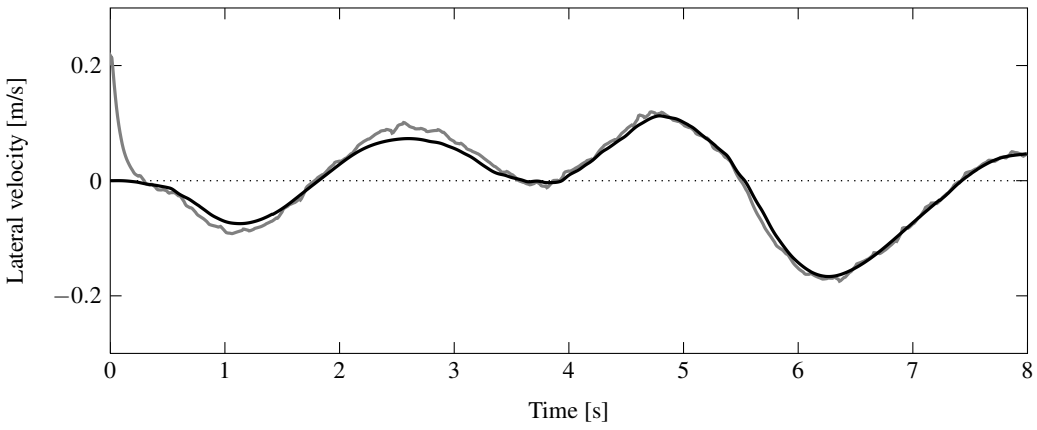

Figure 7.16: *Linear observer lateral slip velocity estimate: low lateral acceleration case*. The developed linear state observer (gray) is shown to accurately estimate the lateral slip velocity (black), when low lateral accelerations are present.

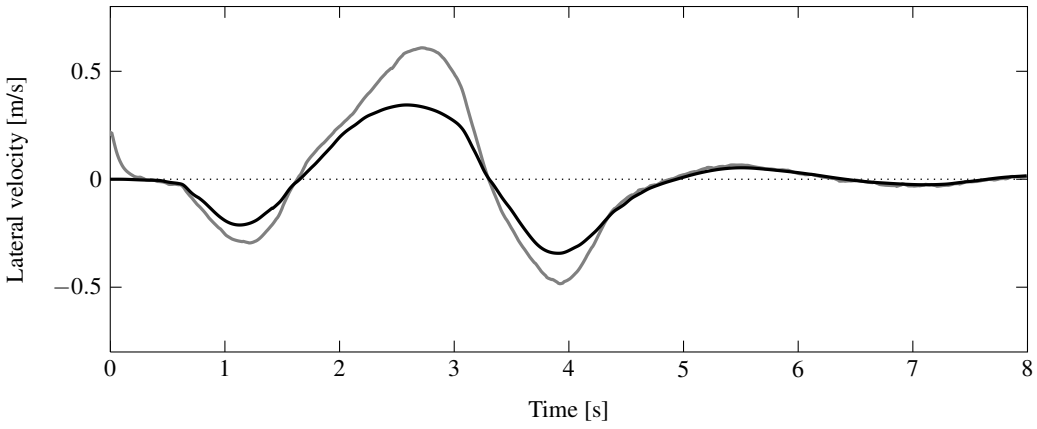

Figure 7.17: *Linear observer lateral slip velocity estimate: high lateral acceleration case*. Error in the lateral slip velocity estimate (gray) of the actual simulated state (black) provided by the developed linear state observer can be seen in the presence of higher lateral accelerations.

7.2.5 Case 7: Effect of Driver Internal Model

To test the effect of the driver experience, the internal predictive model of the driver path follower was changed from a neutral steering vehicle emulating that of the controlled vehicle, to that of an understeering vehicle like the uncontrolled vehicle. This was to emulate the condition where the control would be added without driver knowledge, or where the driver had no previous experience in the controlled vehicle. This causes the driver's intent to be different from the one determined by the driver interpreter in the control. The high lateral acceleration double lane change test case was simulated.

A comparison between the previously presented controlled vehicle and the driver model with the FCG internal model is presented in Figure 7.18. It can be seen that the driver steering input shifts forward in time, as the driver expects the vehicle to understeer, responding slower to steer input when compared to the previous neutral steering case. At 4.5 seconds, a higher yaw rate response can be seen as the controller attempts to track the neutral steer interpreter model, given the increased driver steer angle shown in the first subfigure. At this point in time, the applied motor torques on wheels 3 and 4 are increased causing increased tire usage when compared to the previous case, indicated by the dotted lines. However, even during this corrective manoeuvre only half of the tire saturation is being used on the rear tires. Conversely, a reduction in the normalized tire force can be seen on the front left tire beginning shortly after four seconds. A time shift in the applied torques can be seen corresponding to the shift in driver steer input due to the variation between the driver's internal and the driver interpreter models. This indicates that even small differences between the driver intent and those determined by the internal interpreter model can alter the response and augmenting capabilities of the control system as changes in the tire usage are created.

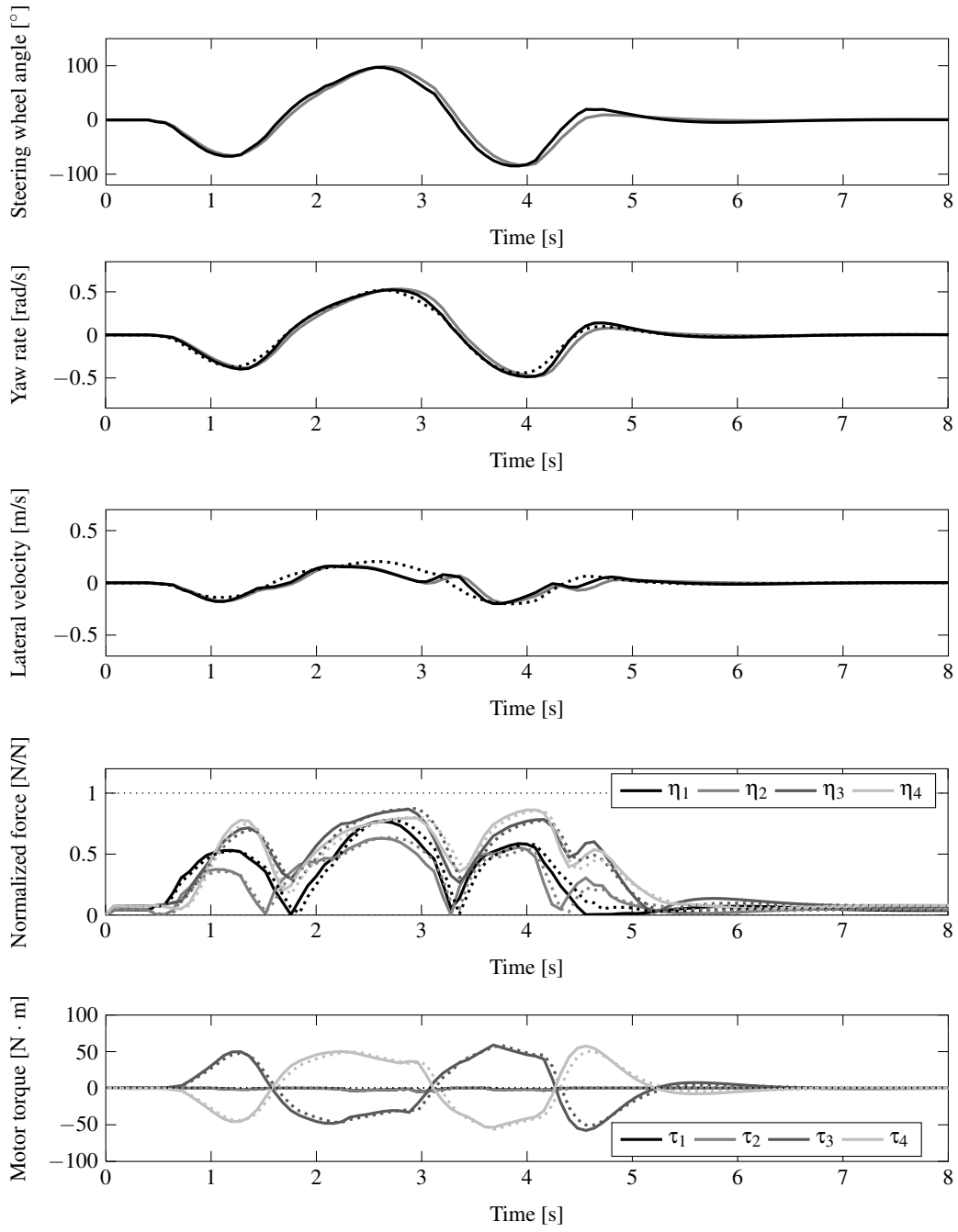

Figure 7.18: *Case 7: closed-loop emergency double lane change response*. The effect of the internal predictive driver model can be seen in the comparison between two controlled vehicles. The controlled response with a driver expecting neutral steer behaviour is given in gray and dotted lines, with the response of the vehicle with a driver expecting understeering behaviour is given in black and solid lines.

7.2.6 Case 8: Effect of Search Constraints and Objectives

The developed control allocation algorithm allows for easy alteration of the constraints to evaluate the effect of vehicle layout or additional constraints. To illustrate the importance of the imposed dynamic square force distribution objective in minimizing the control effort, a simulation with the objective removed was conducted. Removing the dynamic square objective leaves the least-squares minimization algorithm to converge on a rather unfavourable solution, exhibiting significant increases in the control torques applied to the front and rear motors, as shown in Figure 7.19. It can be seen that the steer input of the driver remains lower than that of the uncontrolled case. An increase in the yaw rate tracking is also present. It can be seen that large drive torques are applied to the rear axle and large braking torques are applied to the front axle to maintain the demanded zero longitudinal acceleration. These torques reach the limit of the motors in both the driving and braking conditions. It can also be seen that the normalized tire force is kept below the saturation of the tires, but is greatly increased over the case with the dynamic square objective. From this result it can be seen that the dynamic square objective can be used to control the amount of energy or control effort used by a given allocation. This objective can also greatly reduce tire wear, as the large torques applied in this case require a corresponding increase in longitudinal slip.

7.2.7 Case 9: Effect of Vehicle Configuration

A simulation was conducted using the previously detailed high lateral acceleration double lane change. Figure 7.20 and 7.21 present the vehicle response with four wheel independent torque distribution. This condition can be evaluated by simply removing the enforced condition requiring the motor torque on the front drive axles to be equal. Similar to the rear wheel distribution case, increased yaw rate tracking can be seen throughout the manoeuvre, with a corresponding reduction in lateral slip velocity. The tire force usage on the rear axle is markedly reduced when compared to the previous case at around four seconds. While the current test reaches a lateral acceleration of 0.7 g, this reduction may lead the four wheel implementation to perform better even closer to the handling limit of the vehicle. The required motor torques are also reduced, with higher torque requests being allocated to the rear axle as enforced by the dynamic square objective.

7.2.8 Closed-loop Summary

The closed-loop driver input trials indicate an improvement in vehicle response and a reduction in driver steer input is possible with the application of the developed control methods. As expected the applied control forces have been shown to increase the tire usage but remain below the saturation limit of the tires. The applied motor torques have also been shown to be well below the rated

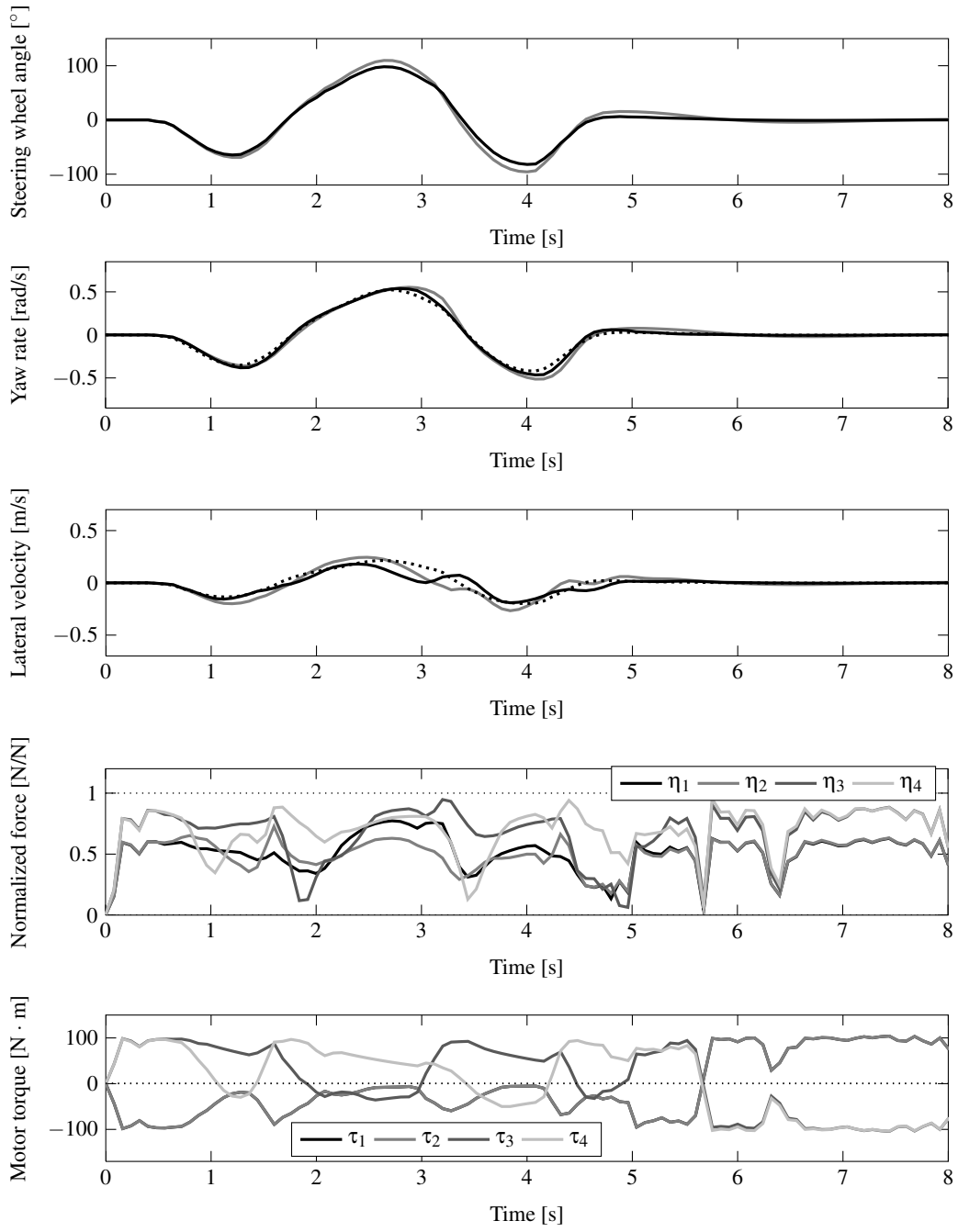

Figure 7.19: *Case 8: closed-loop emergency double lane change, dynamic square objective removed.* This figure illustrates the effect of removing the dynamic square objective from the least-squares minimization allocation. In this case, applied motor torques reach saturation, leading to large amounts of tire usage when attempting to track the reference states (dotted).

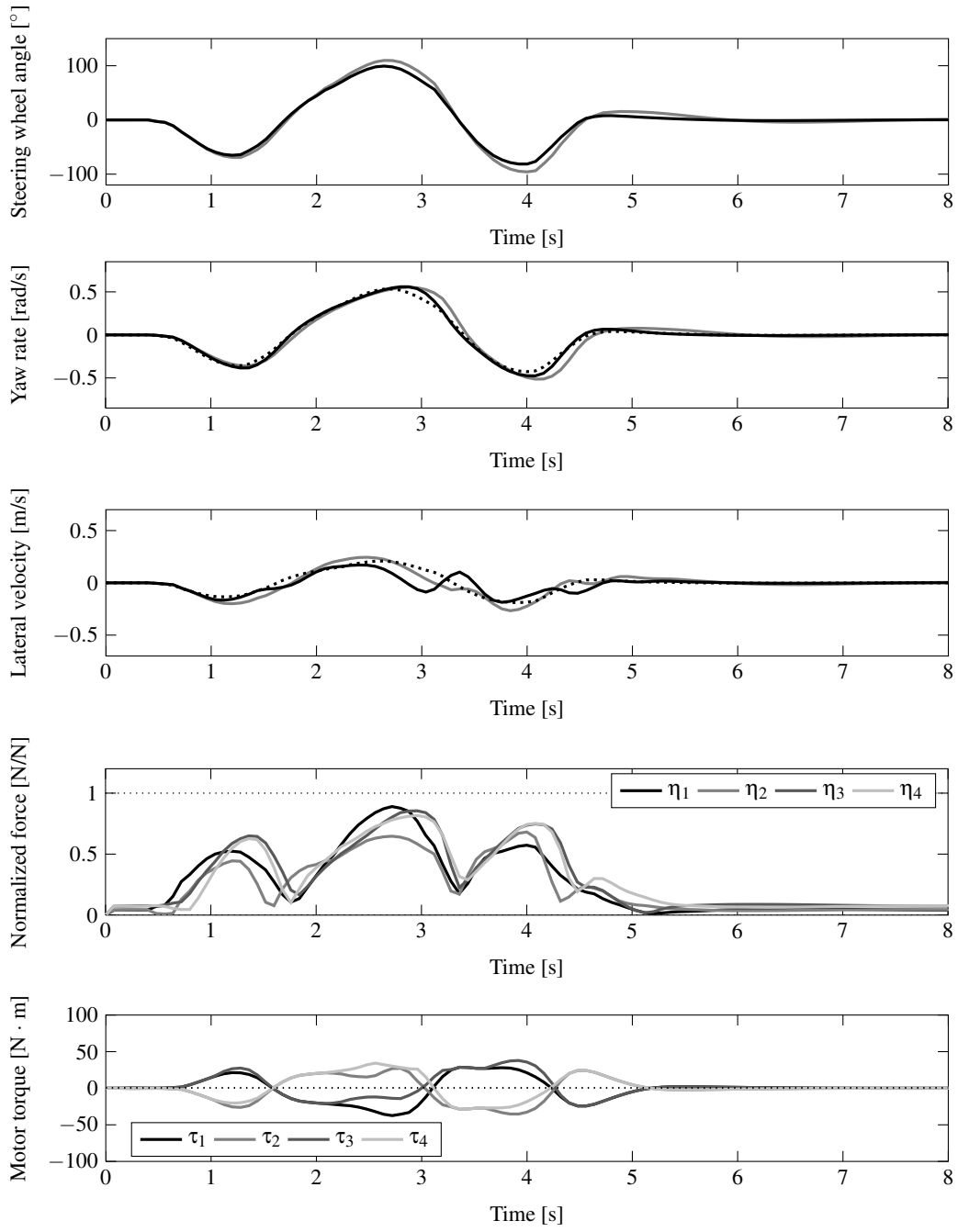

Figure 7.20: *Case 9: closed-loop emergency double lane change response with independent wheel drive*. This figure illustrates the response of a vehicle with four wheel independent torque distribution. It can be seen that the reference yaw rate (dotted) can be tracked with reduced motor torques when compared to the previous controlled and uncontrolled cases.

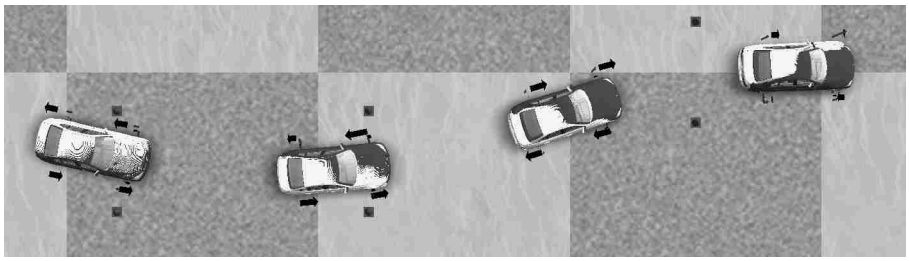

Figure 7.21: *Case 9: emergency double lane change, independent wheel drive, visualization.*

maximum of the drive motors in cases with the dynamic square objective activated. Changing the penalty weightings associated with LQR gains was shown to alter the response of the controlled system, and indicates that further tuning could contribute to increased vehicle performance. The use of linear observers was shown to produce reliable estimates in cases with low lateral acceleration; however, the accuracy of these estimates was shown to be insufficient in cases where high lateral accelerations were present.

7.3 Summary of Results

The control methods and implementations detailed in the preceding chapters were evaluated using simulated results from a variety of test conditions. These tests included cases with and without an active driver present to illustrate the effects of direct yaw moment control on vehicle system behaviour.

First, a set of tests with open-loop driver input were presented, showing the ability of the developed control systems to improve vehicle handling without additional driver input. The controlled systems were shown to provide greater handling response in steady-state and transient manoeuvres, including cases with significant longitudinal accelerations.

Next, a set of closed-loop tests with an active driver model were presented and the efficacy of the developed control and allocation algorithms in modulating vehicle handling response were shown. The implemented systems were shown to improve yaw rate and side slip tracking to the reference vehicle, while reducing driver steer inputs. The effects of LQR controller penalty weightings on tracking were shown. The limitations of the linear observer in the presented cases were discussed, and the potential use of nonlinear observers was proposed. The vehicle architecture presented in Chapter 4 was shown to provide adequate yaw moment control, while an alternative four wheel independent configuration was shown to reduce tire usage and required motor torques. This

could increase the implementation cost, but reduce packaging and weight considerations as smaller electric motors could be used.

In both cases, the developed co-simulation model was proven to be reliable and flexible in simulating multiple cases with minimal user effort.

Chapter 8

Conclusions and Recommendations

The steady progression of vehicle technology from wooden carts to modern road vehicles has been marked with the adoption of numerous technological advances. The integration of advanced technologies is expected to continue, as advances in computing, vehicle components and integration improve upon, and provide for greater amounts of control. These augmented control systems will require methods capable of harnessing the integrated vehicle technologies to improve vehicle safety, efficiency and performance.

This research was intended to develop and apply model-based simulation and control techniques to determine the effects of active dynamics control systems on human operated road vehicles. More specifically, the work detailed focused on demonstrating the viability of variable torque distribution direct yaw moment controls for hybrid electric vehicles. In this chapter, a summary of achievements and implications of the research within this scope are presented, as are areas of potential future work.

8.1 Dissertation Summary

First, the modelling of road vehicle systems was presented. Linearized vehicle models of a BMW 330i were created using a novel method for the automatic generation of the equations of motion. A set of two DOF yaw-plane models was generated and the effect of forward speed on vehicle stability was analyzed using the eigenvalues of the system. Next, a full multibody model was generated and the eigenvalues of the system were determined. From these results, it was inferred that the vehicle remains stable in the modelled configurations. A virtual prototype vehicle model was developed in CarSim® and has been shown to correlate well with experimental data. The model was shown to provide results that correlate well with those of published data. It was also shown that the time domain response of the linear models correlated well with those of the fully nonlinear model.

A hybrid driver model was developed to address the guidance and stabilization tasks of a human

driver, utilizing model predictive control and finite state modelling techniques. A novel method for path determination using genetic algorithms and mapped road elements was developed and evaluated. The developed method utilizes a coupled road and path definition that is capable of replicating complex geometries with a small number of parameters. This definition has been shown to be beneficial for optimal racing lap search problems. The driver models developed have been shown to accurately predict driver inputs, while being reliable and robust in closed-loop vehicle dynamics simulations. These models show great promise in providing robust and realistic closed-loop control of road vehicles for the evaluation of vehicle design and control systems.

The driver models developed have been applied to a novel project for the teaching of vehicle dynamics to undergraduate students. To facilitate this project, a suite of software tools and vehicle models were developed and generated. These methods have been shown to provide students with vehicle design experience, providing quantitative feedback on the effect of design parameters on the response of vehicle systems, within the scope of a single course, and at minimal cost.

A set of linear and nonlinear yaw moment control strategies were developed and evaluated. The results show that a hierarchical control comprised of driver interpretation, control determination and control allocation components was capable of controlling the handling dynamics of a hybrid electric vehicle configuration. A methodology for defining and generating active control systems using a novel method for generating the equations of motion has been developed and implemented in software. The methods and routines have been proven effective in generating active linear controls and state observers, using optimal and search based methods. The methods show great promise in automatically generating controls and reference models for vehicle dynamics control systems. With these methods, more complex vehicle models involving increased degrees of freedom could be readily incorporated into control strategies, providing for increased levels of control. Automatically generated full-state linear observers were shown to be capable of estimating lateral slip velocity; however, the fidelity of the estimates may be unsatisfactory in the presence of high lateral accelerations. While this was proven to be unsatisfactory in the case of lateral slip velocity tracking, it may serve to reduce lateral slip velocity in yaw rate tracking cases. In such cases, accurate estimates in the low lateral acceleration regime would allow for lateral slip velocity tracking, transitioning to lateral slip velocity reduction at high levels of lateral acceleration as shown by the results of the current research.

The use of nonlinear control techniques capable of rejecting modelling uncertainty were evaluated and were capable of maintaining vehicle control in emergency situations, without increased driver steer input. However, the direct allocation of control forces using fixed algorithms proved unsatisfactory. Limitations in the direct allocation method were addressed in the development of a force based indirect allocation algorithm. This method considers vehicle configuration, tire force

and actuator limitations to eliminate manifold solutions in over-actuated vehicle dynamics control systems. An additional allocation objective integrating the dynamic square method was proven to be effective in limiting control effort. The indirect allocation method was shown to be capable of distributing control requests to the various vehicle actuators under allocation constraints and objectives. However, as the number of actuators and constraints increases, search based allocation algorithms could require significant computing power to operate in real-time within vehicle systems. Regardless, the results indicated the promising potential of the developed control allocation method to solve the over-actuated control problem.

Finally, the effect of yaw moment control on the human controlled vehicle system was evaluated. A comprehensive closed-loop simulation model was developed, and used to evaluate the effect of several system parameters. The results show that direct yaw moment control can increase the handling response of road vehicles, while reducing driver effort. The results indicated that the drive torques and longitudinal tire forces required to correct the vehicle response could be obtained, and were below saturation limits in a majority of cases. While it was possible to generate the required yaw moments by varying drive torque across a single axle within the proposed hybrid architecture, further potential was shown for a four wheel independent control case. Additional improvements in vehicle performance and driver comfort may be possible with additional control objectives that attempt to maintain roll and pitch orientations. The methods outlined for the automatic generation of controls, state observers and reference models could be used to design and evaluate the effect of such objectives on the response of the vehicle. The methods developed within this research provide a flexible set of tools capable of reducing the effort required for the design and evaluation of vehicle and control systems.

8.2 Recommendations

Despite promising results, further research is required into the interactions between the human operator and the chassis control systems developed, to ensure the effectiveness of such a system.

8.2.1 Driver Model

The driver model presented made use of proven techniques and was shown to replicate driver response; however, further validation to experimental test data should be conducted. This could be achieved through in-vehicle testing or simulated driver in-the-loop simulations. This testing could be used to further refine the driver models ensuring accurate driver input predictions in all possible test scenarios.

8.2.2 Vehicle Dynamics Controls

The use of the two degree of freedom vehicle models linearized about a straight ahead equilibrium condition developed with the EoM software was proven useful in the determination of driver intentions and control gains. The use of models with higher degrees of freedom could provide further information to the vehicle dynamics controls allowing for roll and pitch angle control. The use of models linearized about non-zero operational points would also be of interest, potentially allowing for greater fidelity in predicting nonlinear vehicle response.

The controls within the simulations performed were assumed to have access to road friction information, and was provided by the CarSim® model. In reality, this information is not directly measurable and road friction estimations must be made. A road friction observer could be integrated into the control methodology, to evaluate the effect of nonuniform road friction on the determination and allocation of the control forces. This would allow for the analysis of the driver-vehicle interactions in an increased number of scenarios, where loss of control could be excited.

8.2.3 Other Considerations

The model developed focused on the yaw plane response of the vehicle, making use of simplistic dynamical hybrid vehicle powertrain component models. The fidelity of the simulations could be increased with the development and integration of more detailed hybrid component models, including motors and energy storage systems. With these models, a more detailed analysis of the interactions within the hybrid system could be evaluated. The proposed allocation method could also be extended to incorporate motor and battery efficiencies in the allocation of control forces. The developed modular co-simulation model could be extended with detailed sub-models, allowing for research into the effects of other subsystems within the integrated scheme, including mechanical brakes and rear wheel steering. Finally, while a validated vehicle model was used, a comprehensive study of the proposed systems should be conducted on a physical prototype using actual hardware.

8.3 Closing Remarks

The simulated results of the variable torque distribution yaw moment control within the hypothetical BMW 330i hybrid vehicle are promising. The proposed system has been shown capable of augmenting the driver inputs, creating a more responsive vehicle. It is expected that implementation of the developed chassis control system would increase safety of the vehicle. The simulation techniques presented are also promising in providing high-fidelity predictions of vehicle response at minimal capital investment. Further investigation into the development and implementation of these systems would be a worthwhile endeavour.

References

[1] Vehicle inertia measurement facility, suspension kinematics and compliance, shock absorber, suspension component geometric and inertia, and tire test measurement results 2006 bmw 330i. Tech. rep., SEA Inc., 7349 Worthington-Galena Rd., Columbus, Ohio 43085, 2006.

[2] Federal motor vehicle safety standards; electronic stability control systems; controls and displays. Tech. Rep. Docket No. NHTSA-2007-27662, U.S. Department of Transportation, 2007.

[3] Vehiclesim math models solver program reference manual. Tech. rep., Mechanical Simulation Corporation, 2007.

[4] Ipgdriver. World Wide Web electronic publication, accessed April 7th,2010.

[5] AGA, M., AND OKADA, A. Analysis of vehicle stability control (vsc)'s effectiveness from accident data. Tech. rep., 2003.

[6] ANDREASSON, J., AND BUNTE, T. Global chassis control based on inverse vehicle dynamics models. *Vehicle System Dynamics 44:1* (2006), 321–328.

[7] BECK, R. *Application of Control Allocation Methods to Linear systems with Four or More Objectives*. PhD thesis, Virginia Polytechnic Institute, 2002.

[8] BENGTSSON, J., JOHANSSON, R., AND SJOGREN, A. *Nonlinear and Hybrid Systems in Automotive Control*. SAE International, Warrendale, 2003.

[9] BHATTI, M. *Funadmental Finite Element Analysis and Applications*. John Wiley and Sons, Inc., 2005.

[10] BOMBARDIER, W. Symbolic modelling and simulation of wheeled vehicle systems on three-dimensional roads. Master's thesis, University of Waterloo, 2009.

[11] BRAYSHAW, D., AND HARRISON, M. A quasi-steady state approach to race car lap simulation in order to understand the effects of racing line and center of gravity location. *Journal Automobile Engineering 219d* (2005).

[12] BUCKHOLTZ, K. Use of fuzzy logic in wheel slip assignment - part 1: Yaw rate control. *SAE Technical Paper 2002-01-1221* (2002).

[13] CAI, G., AND LIM, C. Continuous suboptimal control with partial state feedback. *Journal of Vibration and Control 11* (2005), 561–578.

[14] CASANOVA, D. *On Minimum Time Vehicle Manoevering: The Theoretical Optimal Lap*. PhD thesis, Cranfield University, 2000.

[15] CIKANEK, S., AND BAILEY, K. Regenerative braking system for a hybrid electric vehicle. In *Proceedings of the American Control Conference* (Anchorage, AK, 2002), pp. 3129–3134.

[16] CIPELLI, M., SCHIEHLEN, W., AND CHELI, F. Driver-in-the-loop simulations with parametric car models. *Vehicle System Dynamics 46:1* (2008), 33–48.

[17] COULOM, R. *Reinforcement Learning Using Neural Networks, with Applications to Motor Control*. PhD thesis, Institut National Polytechnique de Grenoble, 2002.

[18] CRITTENDEN, J. Team mojavaton technical paper. Tech. rep., DARPA 2007 Urban Challenge, 2007.

[19] CSME FORUM. *Variable Torque Distribution For Advanced Hybrid Electric Powertrains* (Calgary, 2006).

[20] DAILY, R., AND BEVLY, D. The use of gps for vehicle stability control systems. *IEEE Transactions on Industrial Electronics 51:2*, 270–277.

[21] DANESIN, D. Driveline layout influence on four wheel drive dynamics. *SAE Technical Paper*, 2004-01-0860 (2004).

[22] DEMERS, S. M. Brake booster attenuation to increase efficiency in regenerative braking. Master's thesis, University of Waterloo, 2008.

[23] DENNY, M. The dynamics of antilock brake systems. *European Journal of Physics 26* (2005), 1007–1016.

[24] DRAČA, S. Finite element model of a double stage helical gear reduction. Master's thesis, University of Windsor, 2006.

[25] EHSANI, M., GAO, Y., AND EMADI, A. *Modern Electric, Hybrid Electric, and Fuel Cell Vehicles*. CRC Press, Boca Raton, 2010.

[26] ELLIS, J. *Vehcile Dynamics*. London Business Books, London, 1969.

[27] ENDO, H., ITO, M., AND OZEKI, T. Development of toyota's transaxle for mini-van hybrid vehicles. *JSAE Review 23* (2003), 109–116.

[28] GENTA, G. *Motor Vehicle Dynamics Modeling and Simulation*. World Scientific, Hackensack, 2006.

[29] GIESEN, N. Current analysis of the accident statstics: Mercedes passenger cars get into fewer accidents. Tech. rep., Mercedes-Benz, 2002.

[30] GILL, P., MURRAY, W., AND WRIGHT, M. *Practical Optimization*. Academic Press, London,UK, 1981.

[31] HANCOCK, M., AND WILLIAMS, R. A comparison of braking and differential control of road vehicle yaw-sideslip dynamics. In *Proceedings IMechE.* (2005), vol. 219.

[32] HE, J., AND CROLLA, D. Integrated active steering and variable torque distribution control for improving vehicle handling and stability. *SAE Technical Paper*, 2004-01-1071 (2004).

[33] HEYDINGER, G., SCHWARZ, C., SALAANI, M., AND GRYGIER, P. Model validation of the 2006 bmw 330i for the national advanced driving simulator. *SAE Technical Papers*, 2007-01-0817 (2007).

[34] ISHIO, J., ICHIKAWA, H., KANO, Y., AND ABE, M. Vehicle-handling quality evaluation through model-based driver steering behaviour. *Vehicle System Dynamics 46:1* (2008), 549–560.

[35] JALALI, K., UCHIDA, T., MCPHEE, J., AND LAMBERT, S. Integrated stability contro system for electric vehicles with in-wheel motors using soft computing techniques. *SAE Technical Paper*, 2009-01-0435 (2009).

[36] JAZAR, R. N. *Vehicle Dynamics Theory and Application*. Springer, New York, 2008.

[37] JOHANSSON, R., AND RANTZER, A. *Nonlinear and hybrid systems in automotive control*. Springer-Verlag, London, 2003.

[38] JONASSON, M., AND ANDREASSON, J. Exploiting autonomous corner modules to resolve force contraints in the tyre contact patch. *Vehicle System Dynamics 46:7*, 553–573.

[39] KARNOPP, D. *Vehicle Stability*. Marcel Dekker, New York, 2004.

[40] KATO, M., ISODA, K., AND YUASA, H. Study on vehicle dynamics in marginal condition using dynamic square method. *SAE Technical Paper*, 958503 (1995).

[41] KHALIL, H. K. *Nonlinear Systems, Third Edition*. Prentice-Hall Inc., New Jersey, 2000.

[42] KIENCKE, U., AND NIELSEN, L. *Automotive Control Systems, For Engine,Driveline, and Vehicle*. Springer-Verlag, New York, 2000.

[43] KIERS, M. Automotive regenerative braking utilizing electrochemical capacitor energy storage. Master's thesis, University of Waterloo, 2004.

[44] KIMURA, A., ABE, T., AND SASAKI, S. Drive force control of a parallel-series hybrid system. *JSAE Review 20* (1999), 337–341.

[45] KLOMP, M. Passenger car all-wheel drive systems analysis. Master's thesis, Department of Technology, mathematics and computer science, University of Trollhattan/Uddevalla, 2005.

[46] KOIBUCHI, K., YAMAMOTO, M., FUKADA, Y., AND INAGAKI, S. Vehicle stability control in limit cornering by active brake. *SAE Technical, 960487* (1996).

[47] KORTÜM, W., AND SHARP, R. Multibody computer codes in vehicle system dynamics. *Supp. to Vehicle System Dynamics* (1993).

[48] KURIYAGAWA, Y., IM, H., KAGEYAMA, I., AND ONISHI, S. A research on analytical method of driver-vehicle-environment system for construction of intelligent driver support system. *Vehicle System Dynamics 37:5* (2002), 339–358.

[49] KWAKERNAAK, H., AND SIVAN, R. *Linear Optimal Control Systems*. Wiley-Interscience, Toronto, 1972.

[50] LEE, S., AND ATKINSON, N. Understanding the interaction between passive four wheel drive and stability control systems. *SAE Technical Paper 2002-01-1047* (2002).

[51] LIN, Y., TANG, P., ZHANG, W., AND Q.YU. Artificial neural network modelling of driver handling behaviour in a driver-vehicle-environment system. *Int. J. Vehicle Design 37:1* (2005), 24–45.

[52] LU, J., AND YANG, D. Path planning based on double-layer genetic algorithm.

[53] LUENBERGER, D. Observing the state of a linear system. *IEEE Transactions on Military Electronics 8* (1964), 74–80.

[54] MACADAM, C. Understanding and modeling the human driver. *Vehicle System Dynamics 40:1* (2003), 101–134.

[55] MILLIKEN, W., AND MILLIKEN, G. *Race Car Vehicle Dynamics*. Society of Automotive Engineers International, Warrendale,PA, 1995.

[56] MINAKER, B., AND FRISE, P. Linearizing the equations of motion for multibody systems using an orthogonal complement method. *Journal of Vibration and Control 11:1* (2005).

[57] MINAKER, B., AND RIEVELEY, R. Automatic generation of the non-holonomic equations of motion for vehicle stability analysis. *Vehicle System Dynamics* (2010).

[58] MOKHIAMAR, O., AND ABE, M. Simultaneous optimal distribution of lateral and longitudinal tire forces for the model following control. *Journal of Dynamic Systems, Measurement, and Control 126* (2004), 753–763.

[59] MORENCY, K. Automatic generation of real-time simulation code for vehicle dynamics using linear graph theory and symbolic computing. Master's thesis, University of Waterloo, 2007.

[60] NAGAI, M. The perspectives of research for enhancing active safety based on advanced control technology. *Vehicle System Dynamics 45:5* (2007), 413–431.

[61] NAGAI, M., SHINO, M., AND GAO, F. Study on integrated control of active front steer angle and direct yaw moment. *JSAE Review 23* (2002), 309–315.

[62] NANTAIS, N. Active brake proportioning and its effects on safety and performance. Master's thesis, University of Windsor, 2006.

[63] OH, E. W. K. Vehicle dynamics controller for a hybrid electric vehicle. Master's thesis, University of Windsor, 2006.

[64] ONO, E., HATTORI, Y., MURAGISHI, Y., AND KOIBUCHI, K. Vehicle dynamics integrated control for four-wheel-distributed steering and four-wheel-distributed traction/braking systems. *Vehicle System Dynamics 44:2* (2006), 139–151.

[65] ONO, E., HOSOE, S., TUAN, H., AND DOI, S. Robust stablilization of vehicle dynamics by active front wheel steering control. In *Proc. Conference on Decision and Control* (Kobe, JP, 1996), pp. 1777–1782.

[66] OSBORN, R. P., AND SHIM, T. Independent control of all-wheel-drive torque distribution. *Vehicle System Dynamics 44:7* (2006), 529–546.

[67] PACEJKA, H. *Tire and Vehicle Dynamics*. SAE International, Warrendale,PA, 2005.

[68] PAPELIS, Y. Study of esc assisted driver performance using a driving simulator. Tech. Rep. ID: N04-003-PR, University of Iowa, 2003.

[69] PLOCHL, M., AND EDELMANN, J. Driver models in automobile dynamics application. *Vehicle System Dynamics 45:7* (2007), 24–45.

[70] PLUMBLEE, J., AND BEVLY, D. Control of a ground vehicle using quadratic programming based control allocation techniques. In *Proceedings 2004 American Control Conference* (Boston, 2004), pp. 4704–4709.

[71] RIEVELEY, R., AND MINAKER, B. Variable torque distribution yaw moment control for hybrid powertrains. *SAE Technical Paper*, 2007-01-0278 (2007).

[72] RIEVELEY, R., AND MINAKER, B. Virtual motorsports as a vehicle dynamics teaching tool. *SAE Int. J. Passenger Cars - Mech. Syst. 1:1* (2008), 1325–1333.

[73] RIEVELEY, R., AND MINAKER, B. Virtual motorsports in project-based engineering education. In *Proceedings 22nd. Canadian Congress of Applied Mechanics* (Halifax, N.S., 2009), pp. 104–105.

[74] RIEVELEY, R., MINAKER, B., MAURINI, M., SHALLVARI, I., AND LAPORT, J. Development of an advanced driver model and simulation environment for automotive racing. *SAE Int. J. Passenger Cars - Mech. Syst. 2:1* (2009), 636–644.

[75] SAKAI, S., SADO, H., AND HORI, Y. Dynamic driving/braking force distribution in electric vehicles with independently driven four wheels. *Electrical Engineering in Japan 138:1* (2002).

[76] SALAANI, M. Analytical tire forces and moments model with validated data. *SAE Technical Paper*, 2007-01-0816 (2006).

[77] SALAANI, M., SCHWARZ, C., HEYDINGER, G., AND GRYGIER, P. Parameter determination and vehicle dynamics modeling for the national advanced driving simulator of the 2006 bmw 330i. *SAE Technical Paper*, 2007-01-0818 (2007).

[78] SAMBORSKY, S. Design and simulation of an ultracapacitor-based hybrid electric vehicle. Master's thesis, University of Waterloo, 2006.

[79] SAWASE, K., AND SANO, Y. Application of active yaw control to vehicle dynamics by utilizing driving/breaking force. *JSAE Review 20* (1999), 289–295.

[80] SAYERS, M., AND HAN, D. A generic multibody vehicle model for simulating handling and braking. *Vehicle System Dynamics 25:Supplement* (1996), 599–613.

[81] SHINO, M., AND NAGAI, M. Independent wheel torque control of small-scale electric vehicle for handling and stability improvement. *JSAE Review 24* (2003), 449–456.

[82] SLOTINE, J., AND LI, W. *Applied Non-linear Control*. Prentice Hall, New York, 1991.

[83] TSENG, H., ASHRAFI, B., MADAU, D., BROWN, T., AND RECKER, D. The development of vehicle stability control at ford. *IEEE/ASME Trans. on Mechatronics 4:3* (1999), 223–233.

[84] UNGOREN, A., AND PENG, H. An adaptive lateral preview driver model. *Vehicle System Dynamics 43:4* (2005), 245–259.

[85] WANG, H., AHAO, J., BIAN, X., AND SHI, X. An improved path planner based on adaptive genetic algorithm for autonomous underwater vehicle.

[86] WARD, D., BERTRAM, T., AND HILLER, M. Vehicle dynamics simulation for the development of an extended adaptive cruse control. In *Proc. IEEE/ASME Int. Conf. on Advanced Intelligent Mechatronics* (Atlanta,GA, 1999), pp. 730–735.

[87] YANG, K., AND ORSI, R. Static output feedback pole placement via a trust region approach. *IEEE Transactions on Automatic Control 52:11* (2007), 2146–2150.

[88] YANG, X., WANG, Z., AND PENG, W. Coordinated control of afs and dyc for vehicle handling and stability based on optimal guaranteed cost theory. *Vehicle System Dynamics 47:1*, 57–79.

[89] ZANTEN, A. V., ERHARDT, LUTZ, A., NEUWALD, W., AND BARTELS, H. Simulation for the development of the bosch-vdc. *SAE Technical Paper 960486* (1999).

Appendix A

Appendix A: Vehicle Model Data

This appendix presents the vehicle parameters and suspension locations for a 2006 BMW 330i courtesy of Dr. Gary Heydinger, documented in [1]. The 2006 BMW 330i, is a 4-door passenger car with a 3.0L inline 6 cylinder engine, automatic transmission, rear wheel drive, and Bridgestone Potenza RE050A P225/40R18 88W, P255/35R18 90W tires in the front and rear respectively. Running tire pressures of 32 psi and 36 psi int the front and rear respectively. The Gross Vehicle Weight Rating (GVWR) is 2049 kg, with a front axle weight rating of 970 kg and a rea of 1120 kg. The steering system the average steering ratio (wheel-road wheel) of 15.65. The inertial properties of the vehicle were measured by SEA, and includes weight distribution, vehicle centre of gravity longitudinal, lateral and height position and vehicle moments and products of inertia. The report also detailed suspension and steering kinematics and compliance by means of nine separate tests, and damper testing. The suspension tests included;

The front and rear suspension configurations are as shown in Figure A.1 and A.2, and given in TablesA.3-A.6. As presented in [1], all measurements with respect to an origin located at ground level at the intersection of lines projected laterally through the front axle and longitudinally through the vehicle centreline. The X-direction is positive forward, Y-direction positive toward the passenger's (right) side of the vehicle, and Z-direction is positive down. The rear suspension measurements origin is 108.55 inches directly behind the front.

Table A.1: *Chassis mass parameters*. The table gives the experimentally measured mass properties for a 2006 BMW 330i as presented in [1].

	Mass [kg]	CG Height [mm]	Front Axle-CG [mm]	CG off centre
Curb Weight	1587.3	510.2	1370	10
With Driver	1718.5	509.0	1371	1

Table A.2: *Chassis inertial parameters*. The table gives the experimentally measured inertial parameters for a 2006 BMW 330i as presented by [1].

Loading Condition	I_{xx} $[kg-m^2]$	I_{yy} $[kg-m^2]$	I_{zz} $[kg-m^2]$	I_{xz} $[kg-m^2]$
Curb Weight	546	2470	2743	29
With Driver	572	2487	2768	42

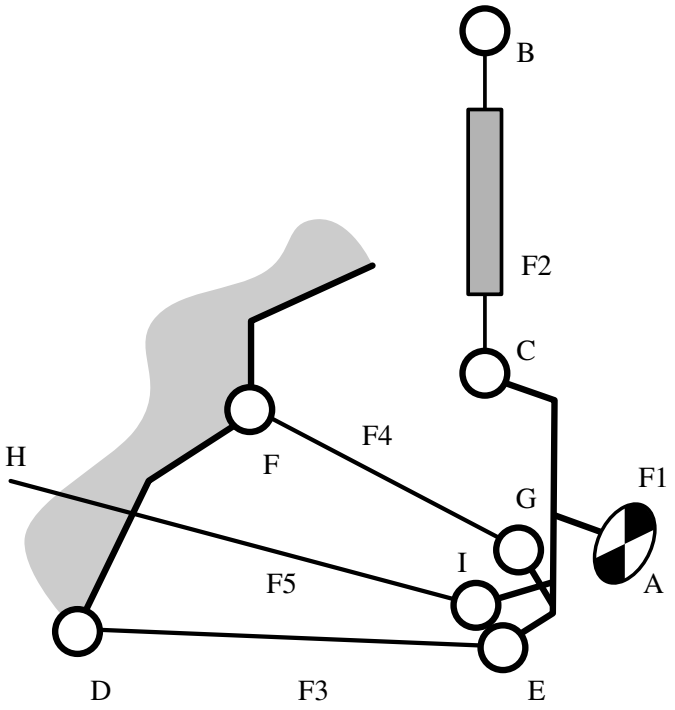

Figure A.1: *2006 BMW 330i front Macpherson strut suspension*. Suspension point and body data given in Tables A.3 and A.4.

Table A.3: *2006 BMW 330i front Macpherson strut suspension body locations*. The table presents front suspension points, as shown in Figure A.1, adapted from [1]. Dimensions given in imperial units.

	Point Name	X [in]	Y [in]	Z [in]
A	Centre of wheel	0	-29.53	-11.92
B	Top of strut	-3.30	-21.30	-30.37
C	Bottom of strut tube	-0.20	-24.40	-11.87
D	Front LCA Inner	10.65	-13.60	-9.57
E	Front LCA Outer	1.60	-26.20	-8.87
F	Rear LCA Inner	-1.70	-14.70	-6.97
G	Rear LCA Outer	0.60	-26.00	-6.77
H	Tie-rod, Inner	2.20	-13.50	-8.37
I	Tie-rod, Outer	5.40	-26.80	-8.07
	Front spindle Height	-	-	11.92

Table A.4: *2006 BMW 330i front Macpherson strut suspension body properties*. The table presents front suspension bodies, as shown in Figure A.1, adapted from [1]. Dimensions given in imperial units.

	Part	Weight [lb]/side	X [in]	Y [in]	Z[in]
F1	Tire/Wheel/Rotor/Hub	84.2	0.00	-30.17	-11.92
F2	Strut(spindle,shock,spring,cal)	29.8	-1.20	-26.20	-18.57
F3	Front lower control arm	3.9	6.34	-19.60	-9.24
F4	Rear lower control arm	2.1	-0.62	-19.99	-6.88
F5	Steering tie rod	2.5	3.82	-20.24	-8.22

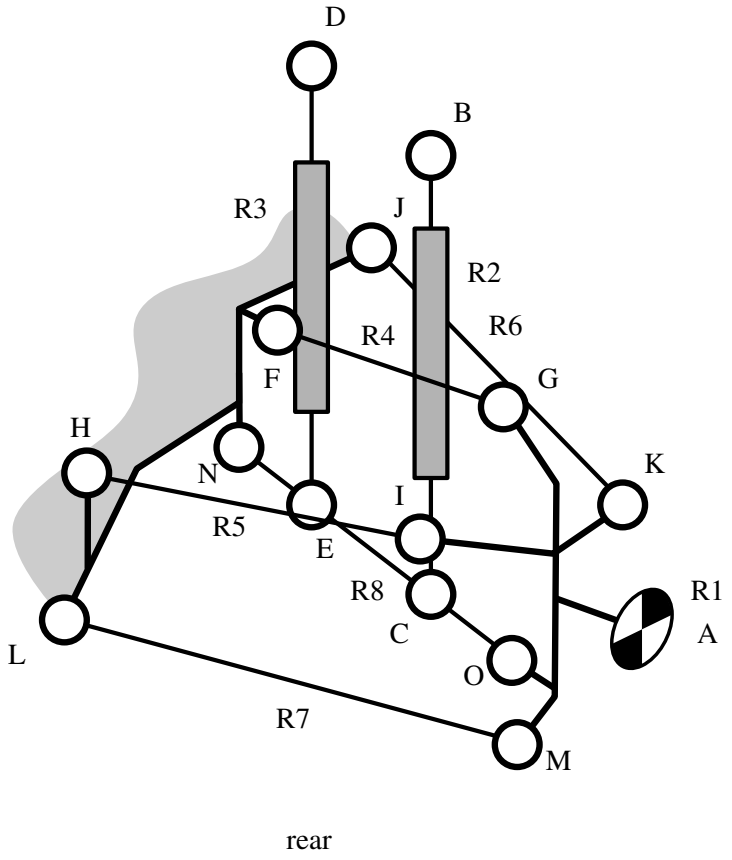

Figure A.2: *2006 BMW 330i rear 5-link suspension*. Suspension point and body data given in Tables A.5 and A.6.

Table A.5: *2006 BMW 330i rear 5-link suspension body positions*. The table presents rear suspension points, as shown in Figure A.2, adapted from [1]. Dimensions given in imperial units.

		X [in]	Y [in]	Z [in]
A	Centre of wheel	0.00	29.53	-12.10
B	Top of spring	-4.90	-17.60	-16.00
C	Bottom of spring	-4.40	-18.40	-5.20
D	Top of shock	-3.90	-20.00	-26.50
E	Bottom of shock	-3.30	-22.20	-7.10
F	Wishbone, Inner	-2.00	-15.80	-16.70
G	Wishbone, Outer	-0.40	-25.60	-16.30
H	Guide link, Inner	5.90	-18.00	-14.60
I	Guide link, Outer	1.50	-25.60	-14.70
J	Track strut, Inner	-8.80	-10.15	-10.50
K	Track strut, Outer	-6.00	-25.90	-10.30
L	Trailing arm, Inner	8.80	-16.20	-9.00
M	Trailing arm, Outer	1.20	-25.80	-6.50
N	Roll-over strut,Inner	-7.00	-10.20	-7.20
O	Roll-over strut,Outer	-2.60	-24.90	-7.70
P	Prop. shaft, Inner	0.00	-8.00	-12.10
Q	Prop. shaft, Outer	0.00	-22.90	-12.10
R	Rear Spindle Height			12.10

Table A.6: *2006 BMW 330i rear 5-link suspension body parameters*. The table presents rear suspension bodies, as shown in Figure A.2, adapted from [1]. Dimensions given in imperial units.

	Part	Weight [lb]/side	X [in]	Y [in]	Z [in]
R1	Tire/Wheel/Rotor/Hub	83.5	0.00	-30.00	-12.10
R2	Spring	5.8	-4.65	-18.00	-10.60
R3	Shock	3.9	-3.60	-21.10	-16.80
R4	Wishbone	2.4	-1.19	-20.73	-16.50
R5	Guiding Susp. Link	2.1	3.60	-21.98	-14.65
R6	Track strut	2.1	-7.38	-18.12	-10.40
R7	Trailing arm	4.88	4.88	-21.15	-7.71
R8	Roll-over strut	-4.51	-4.51	-18.53	-7.48
R9	Carrier Spindle w/calliper	2.35	2.35	-27.10	-10.85
R10	Prop shaft	11.1	0.00	-17.00	-12.10

Table A.7: *Front spring force vs. displacement*. The table gives the experimentally measured spring force vs. displacement for the front suspsension of a 2006 BMW 330i as presented by [1].

Displacement [m]	Force [N]
0.4136584	-8219.7036
0.4186088	-6645.3354
0.4263174	-5632.624
0.4363794	-4950.6481
0.4486969	-4330.368
0.4589484	-3942.1889
0.4698282	-3555.4198
0.4811452	-3247.8894
0.4920972	-2990.6016
0.5027467	-2567.2404
0.5133825	-2122.1296
0.5233704	-1709.0544
0.532894	-1287.2101
0.5423704	-852.82512
0.5523801	-379.52043
0.5579759	735.77209

Tables A.7 and A.8 present the front and rear spring stiffnesses. The approximate linear front and rear spring stiffnesses are 29.77 N/mm and 37.13 N/mm respectively. The vehicle roll stiffness is presented in Table A.9. Table A.10 and A.11 present the front and rear damper force. The steering compliance is given in Table A.12.

Table A.8: *Front spring force vs. displacement*. The table gives the experimentally measured spring force vs. displacement for the rear suspension of a 2006 BMW 330i as presented by [1].

Displacement [m]	Force [N]
0.2307344	-11878.329
0.2369588	-9899.4973
0.2437338	-8726.2148
0.2503615	-7842.1863
0.2562213	-7125.7697
0.2627535	-6252.4277
0.2696338	-5524.5484
0.2757667	-4885.6311
0.2822974	-4366.7106
0.2878971	-3791.6151
0.2944111	-3155.1184
0.3008688	-2482.5753
0.3063984	-1852.3442
0.3119779	-1346.2881
0.3179153	-720.78834
0.325841	371.08624

Table A.9: *Chassis roll stiffness*. The table gives the chassis roll stiffness for a 2006 BMW 330i determined from experimental test data, as presented by [1].

Roll-Stiffness	Front	Rear
Overall stiffness [N·m/deg]	1322	776.3
Auxiliary stiffness [N·m/deg]	1339	602.1

Table A.10: *Front damper force vs. speed*. The table gives the experimentally measured damper force vs. speed data for the front suspension of a 2006 BMW 330i as presented by [1].

Speed [m/s]	Force [N]
-0.2869654662	-121.8384003
-0.2671550191	-119.3371578
-0.247344572	-114.3346898
-0.2275341249	-116.8359323
-0.2077236778	-119.3371578
-0.1879132307	-119.3371578
-0.1681027836	-119.3371578
-0.1482923365	-116.8359323
-0.1284818894	-114.3346898
-0.1086714423	-109.3322217
-0.08886099523	-104.3297367
-0.06905054814	-96.82602617
-0.04924010104	-84.31984758
-0.02942965394	-56.80623091
-0.009619206848	-24.29012923
0.01019124025	25.73461061
0.03000168734	95.76926505
0.0498121344	173.3076322
0.06962258154	258.3497056
0.08943302863	378.4091168
0.1092434757	523.4808938
0.1290539228	668.5526877
0.1488643699	813.6244476
0.168674817	938.6861014
0.1884852641	1043.738283
0.2082957112	1113.772938
0.2281061583	1156.293992
0.2479166054	1188.810077
0.2677270525	1218.824919
0.2875374996	1251.341004

Table A.11: *Rear damper force vs. speed*. The table gives the experimentally measured damper force vs. speed data for the rear suspension of a 2006 BMW 330i as presented by [1].

Speed [m/s]	Force [N]
-0.2866069198	-443.945128
-0.2668014423	-436.5358478
-0.2469959649	-425.4219785
-0.2271904874	-4180126983
-0.20738501	-410.603452
-0.1875795325	-395.7848917
-0.1677740551	-388.3756454
-0.1479685776	-377.2617421
-0.1281631002	-351.3293124
-0.1083576227	-321.6922596
-0.08855214525	-277.2366803
-0.06874666779	-225.3718548
-0.04894119034	-173.5069954
-0.02913571288	-117.9375298
-0.009330235428	-40.14025756
0.01047524203	45.06627043
0.03028071948	178.4330157
0.05008619694	334.0275431
0.06989167439	560.0100795
0.08969715185	789.6972221
0.1095026293	1034.202959
0.1293081068	1249.071575
0.1491135842	1375.029101
0.1689190617	1460.235602
0.1887245391	1504.691215
0.2085300166	1538.032925
0.228335494	1571.374499
0.2481409715	1601.01162
0.2679464489	1630.648605
0.2877519264	1656.581137

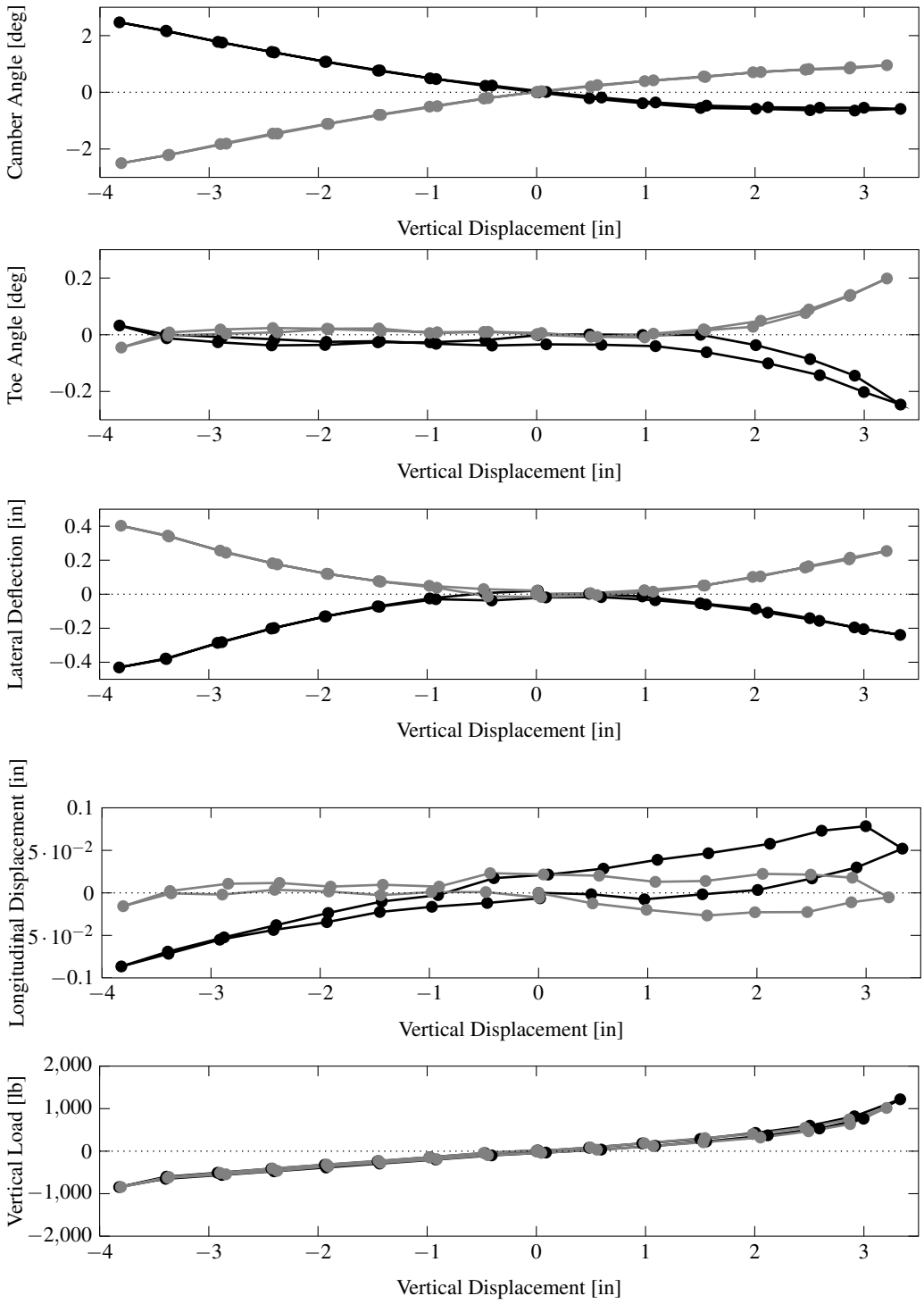

Figure A.3: *Front suspension kinematics and compliance*. Figure illustrates the front suspension kinematic and compliance data for the left (gray) and right (black) wheels.

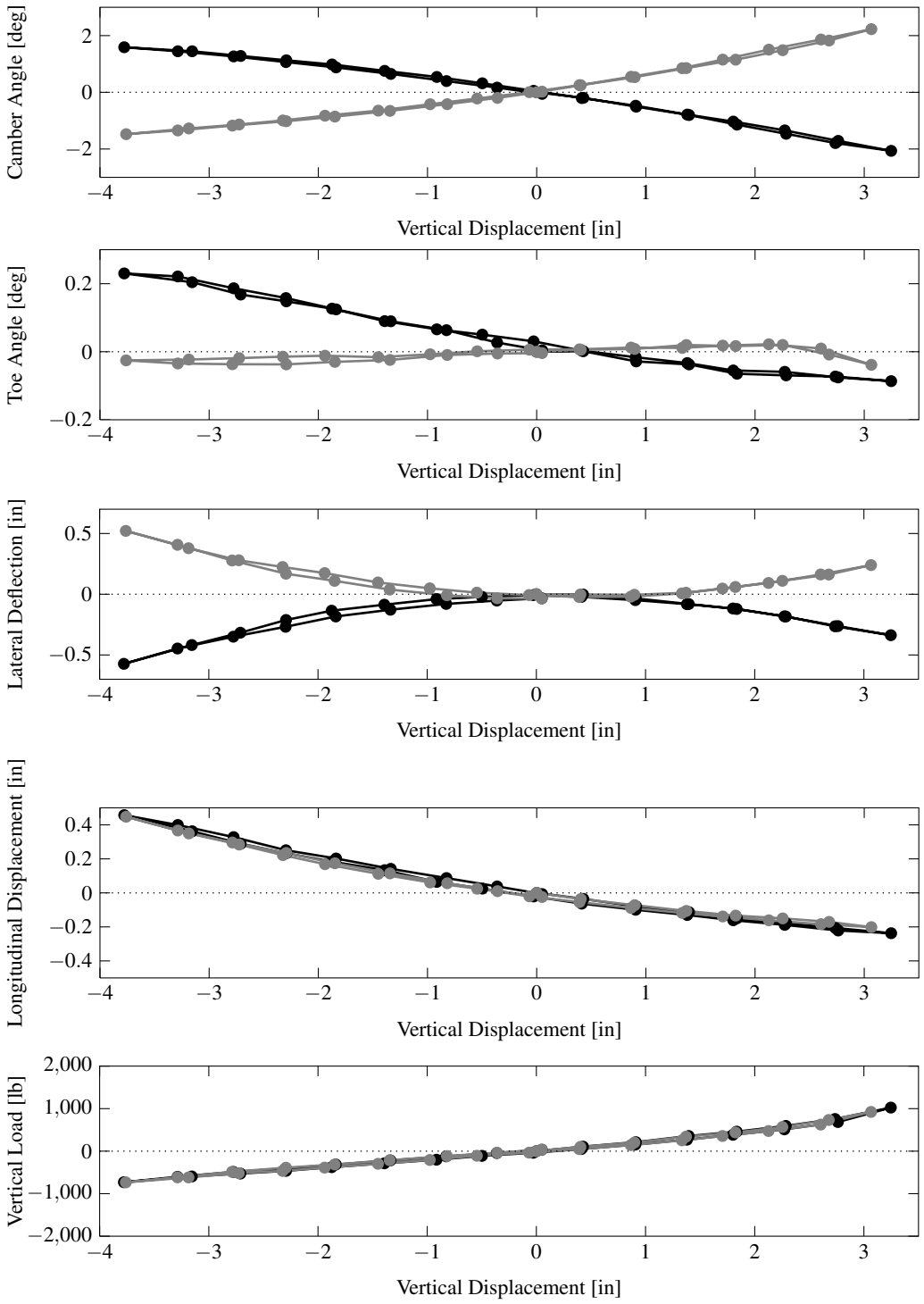

Figure A.4: *Rear suspension kinematics and compliance*. Figure illustrates the front suspension kinematic and compliance data for the left (gray) and right (black) wheels.

Table A.12: *Suspension compliance*. The table gives the experimentally measured suspension compliance for a 2006 BMW 330i as presented by [1].

Compliance	Front	Rear
Lateral Force Steer [deg/N]	-0.00146	-0.0000243
Lateral Force Camber [deg/N]	-0.000218	-0.000158
Aligning Moment [deg/N·m]	0.00155	0.00125

Yaw-plane EoM Model

The linear time invariant system matrices for the nominal yaw-plane vehicle model determined using the EoM implementation are

$$\mathcal{A} = \begin{bmatrix} -0.00000 & -0.00000 & -1.00000 & -0.00000 & -0.00000 & -0.00000 \\ -0.00000 & -0.00000 & -0.00000 & -1.00000 & 25.00000 & -0.00000 \\ 0.00000 & 0.00000 & 0.00000 & 0.00000 & 0.00000 & 0.00000 \\ 0.00000 & 0.00000 & 0.00000 & -7.16741 & 0.00000 & 24.88599 \\ -0.00000 & -0.00000 & -0.00000 & -0.00000 & -0.00000 & 1.00000 \\ -0.00000 & -0.00000 & -0.00000 & -0.08067 & -0.00000 & -9.64015 \end{bmatrix}$$

$$\mathcal{B} = \begin{bmatrix} 0.000000 & 0.000000 \\ 0.000000 & 0.000000 \\ -0.000000 & -0.000000 \\ 0.099386 & -0.000000 \\ 0.000000 & 0.000000 \\ -0.096349 & -0.000365 \end{bmatrix}$$

$$\mathcal{C} = \begin{bmatrix} 0.00000 & 0.00000 & 0.00000 & 0.00000 & 0.00000 & -1.00000 \\ 0.00000 & 0.00000 & 0.00000 & 1.00000 & 0.00000 & 0.00000 \end{bmatrix}$$

$$\mathcal{D} = \begin{bmatrix} 0 & 0 \\ 0 & 0 \end{bmatrix}$$

given the system

```
%%/////////////////////////////////////////////////////////////////////////////
%% bmw330i_yawplane.m
%% Copyright (C) 2010 Rob Rieveley, adapted from work of B. Minaker
%% Licence: GPL
%% ---------------------------------------------------------------------------
%% This file defines a yaw-plane model of a 2006 BMW 330i for use with EOM
%% development version 20091128 (November 2009).
%%/////////////////////////////////////////////////////////////////////////////

global timer; %% Use global timer to loop from 0 to 40 m/s
global vmax; % maximum velocity
global q; % sensor penalty values
global r; % actuator penaly values
global n; % configuration number

if(~isscalar(timer)) % if not batch run
        timer=0.5;vmax = 40;
        n = 2;
end
```

```
u= timer*vmax; % forward speed

CF.length = 1; % length unit conversion (eg. inches to meters)
CF.mass = 1; % mass unit conversion (eg. pounds to kilograms)

cg = [1100 1370 1600]; % vehicle configurations: cog location
Ca = [97350 86488 76150;75331 87410 99171]; % vehicle configurations: ...
% front and rear cornering stiffness

Caf = Ca(1,n); % set front cornering stiffness
Car = Ca(2,n); % set rear cornering stiffness
a = cg(n)/1000; % set the centre of gravity to front axle length
wb = 2.7572; % wheelbase length

cog = [0;0;0]; % centre of gravity location
wheelbase_offset = [wb;0;0]; % set wheelbase offset

%% Add one rigid body, along the x-axis
body.mass=1718+106+117;
body.momentsofinertia=[546;2470;2743];
body.productsofinertia=[0;0;0];
body.location=[0;0;0.0254*20];
body.name='cabin';
body.type='body';
body.vel=[u;0;0];
the_system.item{end+1}=body;

point.type='rigid_point';
point.name='road';
point.body1='cabin';
point.body2='ground';
point.location=cog;
point.forces=1;
point.moments=2;
point.axis=[0;0;1];
the_system.item{end+1}=point;
point ={};

%% Add a damping, to connect our body to ground, aligned with y-axis (front tire)
spring.name='front tire';
spring.type='flex_point';
spring.body1='cabin';
spring.body2='ground';
spring.location=[a;0;0];
spring.forces=1;
spring.moments=0;
spring.axis=[0;1;0];
spring.damping=[2*Caf/u;0];
the_system.item{end+1}=spring;

%% Rear tire
spring.name='rear tire';
spring.location=[-(wb-a);0;0];
spring.damping=[2*Car/u;0];
the_system.item{end+1}=spring;

%% Constrain to planar motion
point.type='rigid_point';
point.name='road';
point.body1='cabin';
```

```
point.body2='ground';
point.location=[0;0;0];
point.forces=1;
point.moments=2;
point.axis=[0;0;1];
the_system.item{end+1}=point;

% Sensors ---------------------------------------------------
item.type='sensor';
item.name='cabin yaw rate';
item.body1='cabin';
item.body2='ground';
item.location1=CF.length.*cog;
item.location2=CF.length.*cog+[0;0;-1];
item.active= 1;
item.measured = 1;
item.feedback =0;
item.twist=1; % rotation
item.order = 2; % rate
item.frame = 0; % local
item.gain= 1;
item.penalty = q(1);
item.pltgain = 180/pi();
item.pltylabel = '[rad/s]';
the_system.item{end+1}=item;
item={};

item.type='sensor';
item.name='cabin lateral slip velocity';
item.body1='cabin';
item.body2='ground';
item.location1=CF.length.*cog;
item.location2=CF.length.*cog+[0;-1;0];
item.active =1;
item.measured = 0;
item.feedback = 0;
item.twist=0; % linear
item.order = 2; % velocity
item.frame = 0; % local
item.gain= 1;
item.penalty = q(2);
item.pltgain = 1;%/u*180/pi();
item.pltylabel = '[m/s]';
the_system.item{end+1}=item;
item={};

% Actuators -------------------------------------------------
act.name='$\\delta_f$';
act.type='actuator';
act.body1='cabin';
act.body2='ground';
act.location1=[a+CF.length*cog(1);0;0];
act.location2=[a+CF.length*cog(1);-1;0];
act.twist=0;
act.penalty = r(1);
act.gain= 2*Caf*pi()/(180*15.65);
the_system.item{end+1}=act;

act.name='$M_z$';
act.type='actuator';
act.body1='cabin';
```

```
act.body2='ground';
act.location1=CF.length*cog;
act.location2=[CF.length*cog(1);0;-1];
act.twist=1;
act.penalty = r(2);
act.gain=1;
the_system.item{end+1}=act;
```

Appendix B

Appendix B: Vehicle Validation Tests

This appendix presents the vehicle validation tests evaluating the CarSim model used within this study. The steady-state and transient responses of the nominal vehicle model have been shown to correlate well with those presented by Heydinger[33]. These tests presented include:

- Slowly increasing steer test @ 80 km/h
- Steady-state steer test @ 40 km/h
- Double lane change test @ 50 km/h
- Pulse steer test @ 40 km/h

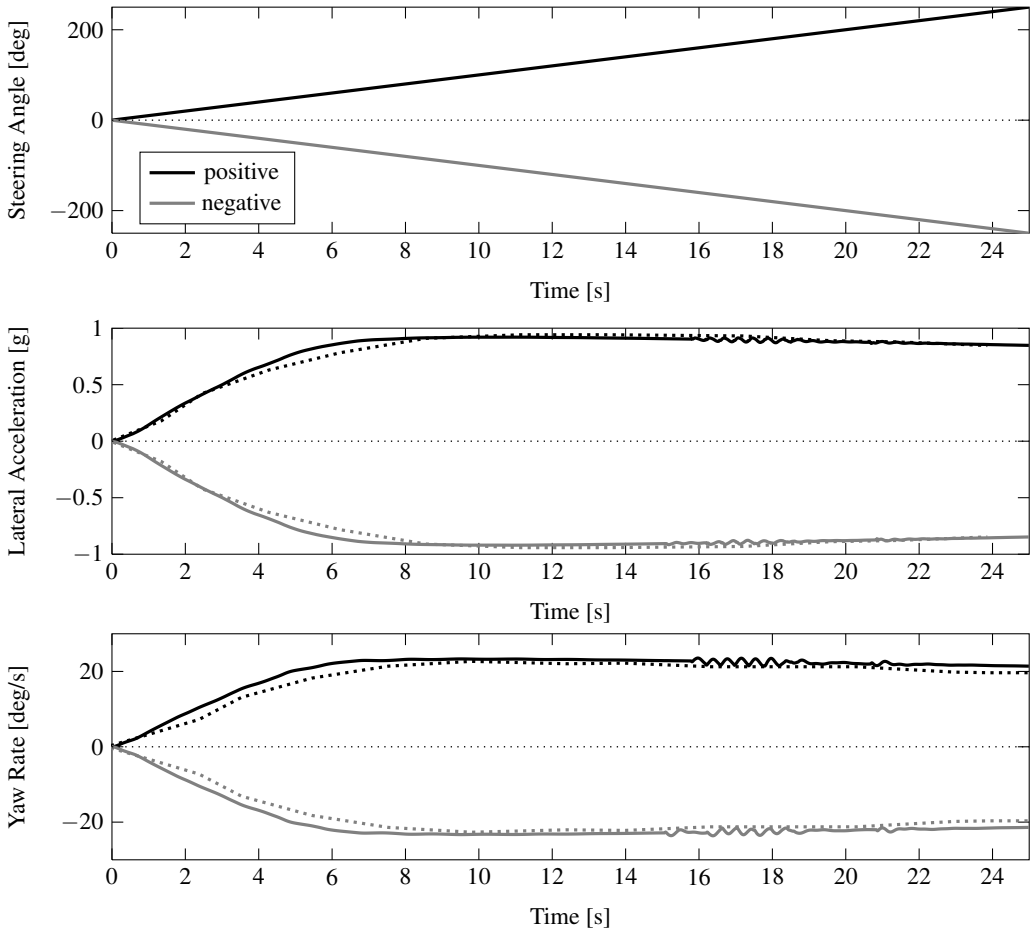

Figure B.1: *Model verification: ramp steer input*. Steadily increasing steer input response for 2006 BMW 330i with forward speed of 80 km/h. Tire saturation initializes at approximately fifteen seconds corresponding to a steering wheel input of 120 degrees. The simulated result (solid) correlates well with those found in literature (dotted).

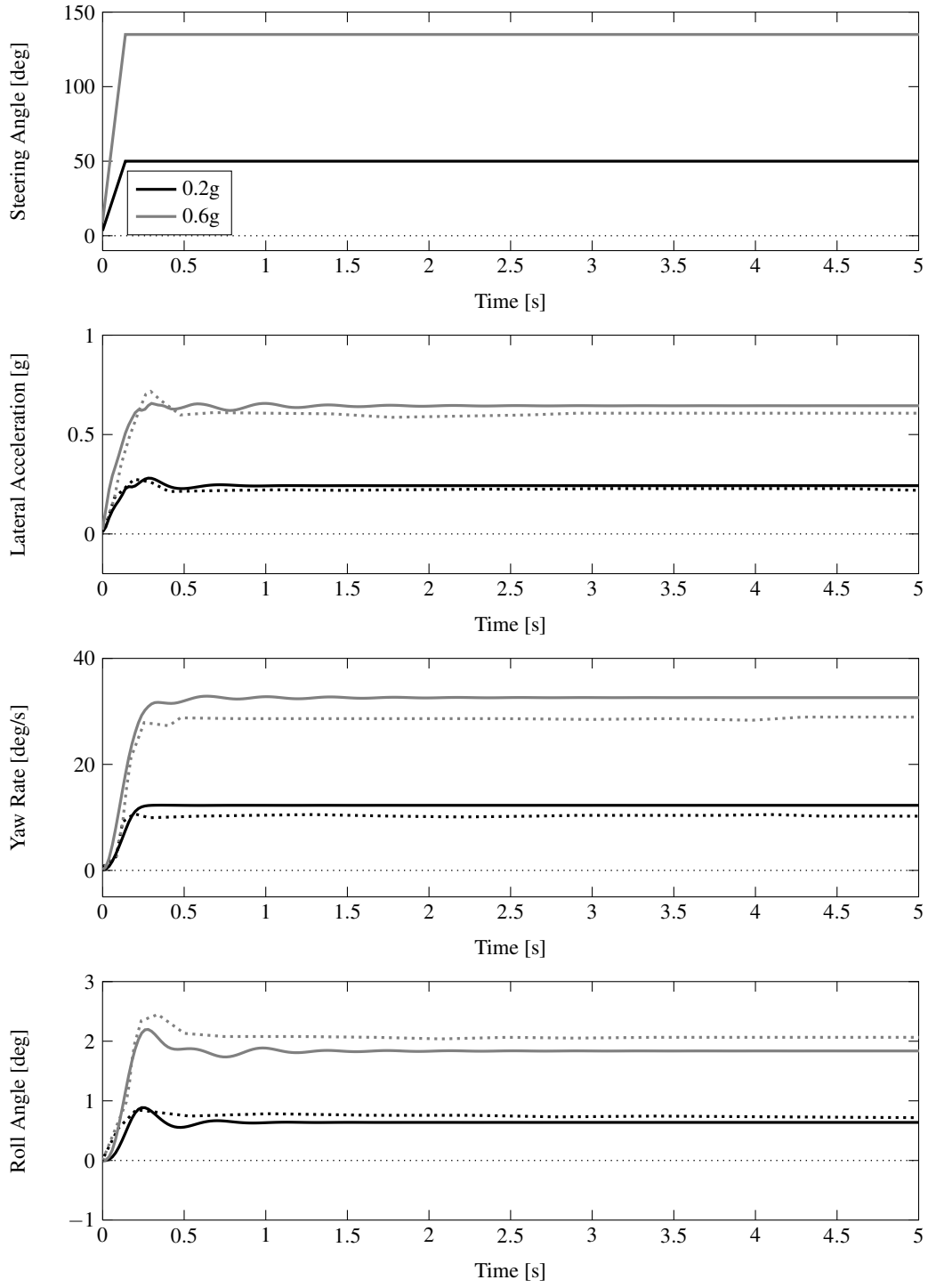

Figure B.2: *Model verification: steady-state steer input* Steady-state steer input response for 2006 BMW 330i with a forward speed of 40 km/h. The black and grey lines represent 0.2 and 0.6 g lateral cornering conditions. The simulated result (solid) correlates well with those found in literature (dotted).

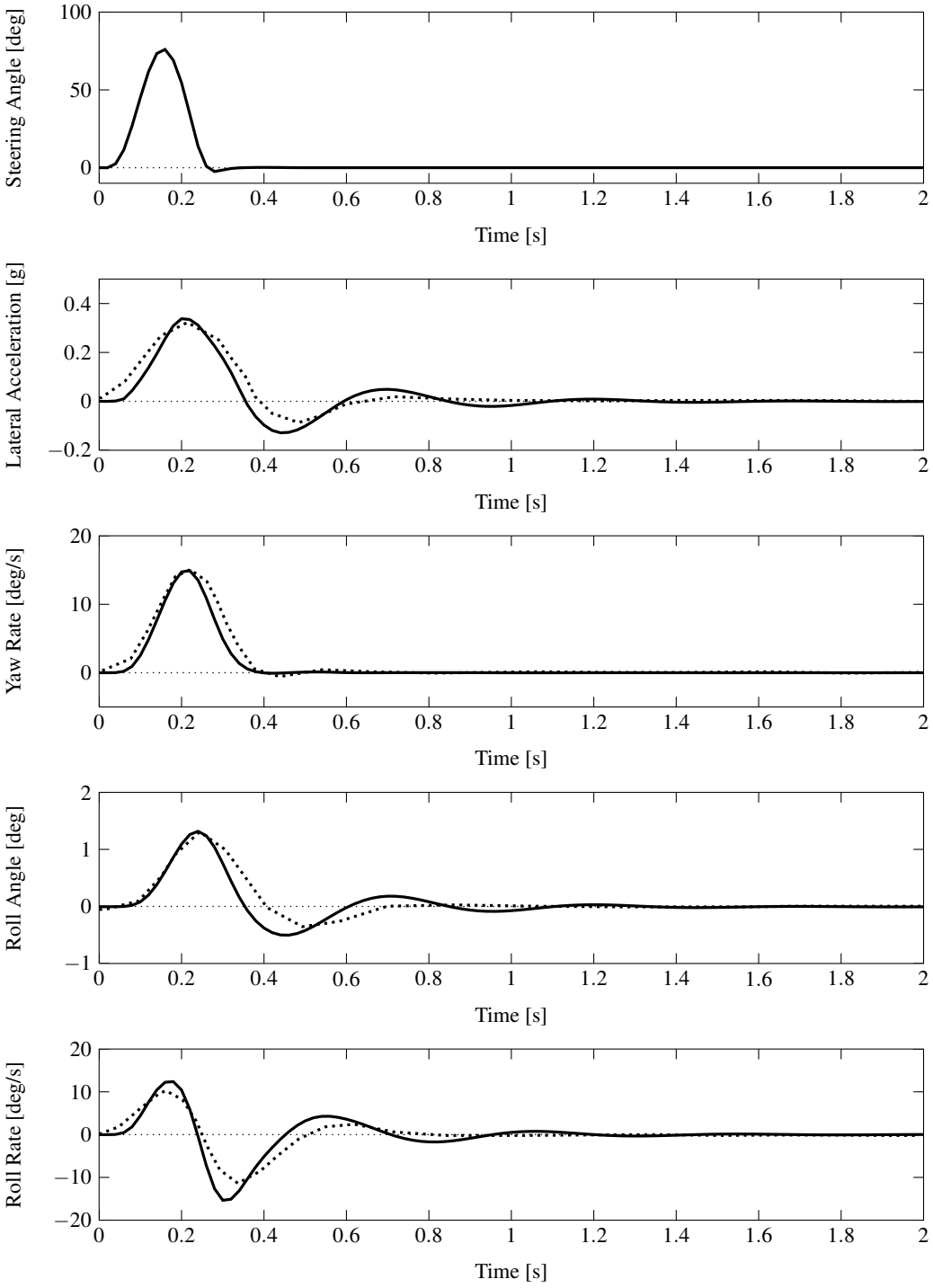

Figure B.3: *Model verification: pulse steer input* Pulse steer input response for 2006 BMW 330i with a forward speed of 40 km/h. The simulated result (solid) correlates well with those found in literature (dotted).

Appendix C

Appendix C: Algorithms

This appendix presents algorithms developed within the documented study.

Longitudinal Driver State Operations

The finite state machine driver routines for the longitudinal driver model presented in chapter three are outlined in this section. The tunable driver model is comprised of an initialization state and five operational states. Within each state the reference velocity and acceleration are determined given a set of driver parameters. The driver is described using coefficients expressing the straight line speed k_{u} and $u_{\max}$, the longitudinal acceleration k_{a}, as well as the cornering radius ρ_{limit} and speed k_{c} limits of the driver for a given test condition.

State 0: Initialization

On entry:
state $= 0$
$\rho(t+t_{\mathrm{f}}) = \rho_{\mathrm{limit}}$
Exit condition:
1. if $(\rho(t+t_{\mathrm{f}}) > \rho_{\mathrm{limit}})$ set $s_{\mathrm{o}} = s(t+t_{\mathrm{f}}) \Rightarrow$ state 1
2. if $(\rho(t+t_{\mathrm{f}}) \leq \rho_{\mathrm{limit}})$ set $s_{\mathrm{o}} = s(t+t_{\mathrm{f}}) \Rightarrow$ state 5

State 1: Straight Line

On entry:

state $= 1$

$u_{\text{ref}} = k_{\text{u}} u_{\max}$

$\Delta u = u_{\text{ref}} - u(t)$

$t_a = \min\left(\frac{\Delta u}{9.81 k_{\text{a}}}, t_{\min}\right)$

$a_{\text{ref}} = \min\left(\frac{\Delta u}{9.81 t_a}, a_{max}\right)$

Exit condition:

1. if $(\rho(t+t_{\text{f}}) \geq \rho_{\text{limit}}) \Rightarrow$ state 1
2. if $(\rho(t+t_{\text{f}}) < \rho_{\text{limit}})$ set $s_{\text{o}} = s(t+t_{\text{f}}) \Rightarrow$ state 2

State 2: Approaching Change

On entry:

state $= 2$

$u_{\text{ref}} = \sqrt{9.81 k_{\text{c}} \rho(t+t_{\text{f}})}$

$\Delta s = s_{\text{o}} - s(t)$

$\Delta u = u_{\text{ref}} - u(t)$

$t_{\text{a}} = \frac{\Delta s}{u(t)}$

$a_{\text{ref}} = \frac{\Delta u}{9.81 t_{\text{a}}}$

$t_{\text{p}} = \frac{\Delta s}{u(t)} - \frac{\Delta u}{9.81 k_{\text{u}}} - \frac{1}{2}\frac{\Delta u^2}{9.81 k_{\text{a}} u(t)}$

$t_{\text{m}} = \frac{\Delta s}{u(t)} - \frac{\Delta u}{9.81 k_{\text{a}}} - \frac{1}{2}\frac{\Delta u(t)^2}{9.81 u(t)}$

$t_{\text{p}} = \min\left(t_{\text{p}}, t_{\text{m}}\right)$

Exit condition:

1. if $\left(t_{\text{p}} > 0 \text{ and } \rho(t) \geq \rho_{\text{limit}} \text{ and } |\Delta u| > \varepsilon u_{\text{ref}}\right) \Rightarrow$ state 2
2. if $\left(t_{\text{p}} \leq 0 \text{ and } \rho(t) \geq \rho_{\text{limit}} \text{ and } |\Delta u| > \varepsilon u_{\text{ref}}\right) \Rightarrow$ state 3
3. if $(\rho(t) < \rho_{\text{limit}})$ set $s_{\text{o}} = s(t+t_{\text{f}}) \Rightarrow$ state 5
4. if $(|\Delta u| \geq \varepsilon u_{\text{ref}} \text{ and } \rho(t) \geq \rho_{\text{limit}}) \Rightarrow$ state 4

State 3: Braking

On entry:

$state = 3$

$\Delta s = s_{\mathrm{o}} - s(t)$

$\Delta u = u_{\mathrm{ref}} - u(t)$

$a_{\mathrm{ref}} = \frac{-u\Delta u - \frac{1}{2}\Delta u^2}{9.81\Delta s}$

$u_{\mathrm{ref}} = \sqrt{|9.81 k_{\mathrm{c}} \rho(t + t_{\mathrm{f}})|}$

Exit condition:

1. if $(\Delta u > \varepsilon u_{\mathrm{ref}}$ and $\rho(t) \geq \rho_{\mathrm{limit}}) \Rightarrow$ state 3
2. if $(\Delta u \leq \varepsilon u_{\mathrm{ref}}$ and $\rho(t) \geq \rho_{\mathrm{limit}}) \Rightarrow$ state 4
3. if $(\rho < \rho_{\mathrm{limit}})$ set $s_{\mathrm{o}} = s(t + t_{\mathrm{f}}) \Rightarrow$ state 5

State 4: Wait

On entry:

$state = 4$

$u_{\mathrm{ref}} = \sqrt{|9.81 k_{\mathrm{c}} \rho(t + t_{\mathrm{f}})|}$

$a_{\mathrm{ref}} = 0$

Exit condition:

1. if $(\rho(t) \geq \rho_{\mathrm{limit}}) \Rightarrow$ state 4
2. if $(\rho(t) < \rho_{\mathrm{limit}}) \Rightarrow$ state 5

State 5: Curve Region

On entry:

$state = 5$

$u_{\mathrm{ref}} = \sqrt{|9.81 k_{\mathrm{c}} \rho(t + t_{\mathrm{f}})|}$

$a_{\mathrm{ref}} = 0$

Exit condition:

1. if $(\rho(t) < \rho_{\mathrm{limit}}) \Rightarrow$ state 5
2. if $(\rho(t) \geq \rho_{\mathrm{limit}}) \Rightarrow$ state 1

Vita Auctoris

Name: Robert J. Rieveley
Born: Windsor, Ontario, Canada, 1981
Education: 1995-2000 Saint Joseph's Highschool, Windsor, Ontario, Canada
2000-2004 Honours Bachelor of Applied Science with Automotive Option, Mechanical Engineering, University of Windsor, Windsor, Ontario, Canada